Controls of fault zone structure on synthetic seismic images of the Maghlaq Fault, Malta

Mari Prestegård

Master Thesis in Basin and Reservoir Geoscience

Department of Earth Science

University of Bergen

June 2020

Abstract

Application of seismic reflection data and 2D seismic modelling studies based on field analogues, contribute to closing the scale gap between field observations and interpretation of seismic data. This has improved the understanding of structurally complex reservoirs, with special focus on the impact faults and fractures have on e.g., hydrocarbons, water and CO_2-storage in the subsurface. Seismic imaging of fault zones is inherently challenging because they are narrow zones of heterogeneously deformed rocks at the limit of seismic resolution. Modelling faults, which exert strong control on fluid flow, allow us to investigate their seismic signatures to further help seismic interpreters in the characterization of such structures in seismic data. In this thesis, realistic geological models were generated based on virtual outcrop models from exposed sections of the Maghlaq Fault situated in the Miocene-Oligocene carbonate succession in Malta. Through an efficient 2D seismic modelling approach, the fault zone architecture has been modelled with variation in fault elements, size, elastic properties, and fault geometry. In addition, modelling at different dominant frequencies show great variability in resolution and detail-level within the resulting synthetic seismic images. The Maghlaq Fault is characterized by the termination of footwall reflections and fault-related deformation. The obtained results of the imaged fault zone show a change in fault discontinuity associated with fault zone elements and geometries, as well as variation in amplitude and interference pattern owing to changes in elastic properties and the presence of sub seismic structures. Vertical and horizontal resolution in the seismic images is strongly controlled by the illumination and dominant frequency, and that the apparent dip of the fault is significantly lower in low-frequency (20 Hz) seismic images than the true dip. Furthermore, elastic properties impact the reflection characterization and delineation of structural geometries with intersecting acoustic impedance boundaries due to interference within the fault zone. Analysis of the synthetic seismic in this thesis may improve the understanding of the seismic signatures of fault zones.

Acknowledgements

This thesis is part of my MSc degree in Basin and Reservoir Geoscience at the Department of Earth Science, University of Bergen. In association with this project, there are several people I would like to show my greatest gratitude. First and foremost, I would like to thank my main supervisor Prof. Atle Rotevatn for all the guidance, feedback, and motivation these past two years. Thanks to my co-supervisor Isabelle Lecomte for feedback, guidance, and discussions. I would like to express that I am extremely thankful for how they managed to always be available and provided the best guidance and support possible during the Covid-19 situation that affected the final stages of my MSc degree. A special thanks to co-supervisor Vilde Dimmen for guidance and feedback, especially during my fieldwork in Malta. In addition to Vilde, I would like to thank Isabel Edmundson, Prof. David Sanderson, and Maria Erichsen Ordemann for their contributions during our fieldwork.

UiB are acknowledged for funding the fieldwork for this study. Thanks to NORCE for the academic license to the software LIME. A special thanks to NORSAR for the use of academic license to NORSAR Software Suite and SeisRoX. MathWorks is thanked for the academic license to Matlab.

I would like to thank my fellow students at the University of Bergen for making these five years memorable through coffee breaks and great field trips. A special thanks to my floorball team for keeping me active and focused on something else than geology. Thanks to Kari Gulbrandsen, Kristine Andres, and Harry Scott for proof-reading and feedbacks.

Thanks to Anna and Charles at Maple Farm B&B for their great hospitality, kindness, and tuna sandwiches during our fieldwork. A special thanks to my friend and field partner, Ingvild Andersen Gabrielsen, for excellent company, discussions, support, and for putting up with me. The last two years would not have been the same without you. Finally, I would like to thank my family and Maria for their endless support, encouragement, and for always being there for me.

Mari Prestegård

Bergen, June 2020

CONTENTS

1. INTRODUCTION

1.1 Project framework

This study is one of two interrelated MSc projects investigating the seismic response of the carbonate-hosted Maghlaq Fault in Malta. Together, the two projects aim to improve the understanding of the seismic imaging of fault zones in carbonate rocks. This thesis investigates and identifies the seismic signatures by varying fault geometries and structural features within the Maghlaq Fault zone. The related sister MSc project (by Ingvild Gabrielsen Andersen) focuses on investigating the seismic expression of the Maghlaq Fault zone through the effect of various geophysical survey parameters on the seismic.

1.2 Motivation

Geological structures, such as faults and fractures, play a major role in the control of fluid flow in the subsurface. The understanding of such structures has implications in the simulation of e.g., hydrocarbons and groundwater, as flow in a brittle fault zones has proven to be dependent on the fault zone architecture and their properties (Caine et al., 1996). Fault detection in the subsurface are generally done with seismic reflection data. The structural elements occurring in a fault zone may, however, be hard to detect in seismic sections due to limited seismic resolution. This makes it difficult to reveal small-scale features and detect zones of higher structural complexity, which excert strong control on fluid transport in a subsurface reservoir (Jolley et al., 2007; Fossen and Rotevatn, 2016). To apply 2D seismic modelling on outcrop analogues, with structures on a range of scales, is one way to improve the understanding of such subsurface reservoirs (e.g., Eide et al., 2018; Rabbel et al., 2018; Lubrano-Lavadera et al., 2019). This way synthetic seismic modelling is trying to close the scale gap between outcrop analogues and seismic data of subsurface reservoirs, and this thesis is a contribution to that effort. The thesis comprises a study of an outcrop analogue from the Maghlaq Fault in Malta, used for seismic modelling of a Miocene-Oligocene carbonate-hosted fault in order to investigate seismic signatures of fault zone structures and geometries. Imaging of carbonate rocks are challenging due to high seismic velocities inherent in carbonates minerals which contribute to poor contrast in acoustic impedance and low resolution. As the fault zone structures are known and elastic properties can be controlled during modelling, we can get a better understanding of the resulting seismic images. Using this field-based method, seismic modelling can help seismic interpreters to recognize and characterize fault zones in structurally complex reservoirs.

1.3 Aims and objectives

The aim of this study is to improve the understanding of seismic imaging of faults in carbonate rocks, focusing on varieties in fault geometries. This thesis investigates and identifies seismic signatures of structural features in and around a carbonate-hosted fault through 2D seismic modelling. The synthetic seismic is based on detailed outcrop investigation of the Maghlaq Fault. The aim is achieved through the following objectives:

- Document and describe stratigraphic and fault zone architecture through fieldwork to create realistic 2D geological models.
- Use petrophysical /geophysical data from the literature and simple empirical relations to populate the 2D geological models with elastic properties.
- Use the 2D (3D) convolution method between a PSDM filter and reflectivity models to generate synthetic seismic images.
- Perform sensitivity testing by varying dominant frequency, geological geometries and input of typical fault zone elements, as well as varying seismic velocities.

1.4 Study area

The Republic of Malta is an archipelago situated in the Central Mediterranean Sea (Fig. 1). The Pelagian Platform in Malta is one of few places where a larger part of the Oligocene-Miocene succession appears above sea level (Reuther and Eisbacher, 1985; Micallef et al., 2013). The archipelago is located on the northern flank of the WNW-ESE trending Pantelleria Rift system, but is dominated by normal faulting that formed a series of ENE-WSW trending horst and graben structures (Dart et al., 1993). The studied Maghlaq Fault is the only onshore major fault with similar trend as the offshore Pantelleria Rift. The Maghlaq Fault is exposed on the southwestern coast of Malta and offsets the Oligocene-Miocene pre-to syn-rift succession by a displacement up to 210 m (Bonson et al., 2007). The footwall is exposed 4 km, whereas the hangingwall is preserved 2.5 km (Dart et al., 1993). Furthermore, the Maghlaq Fault has sections with well exposed sediments across the fault which make it excellent to study.

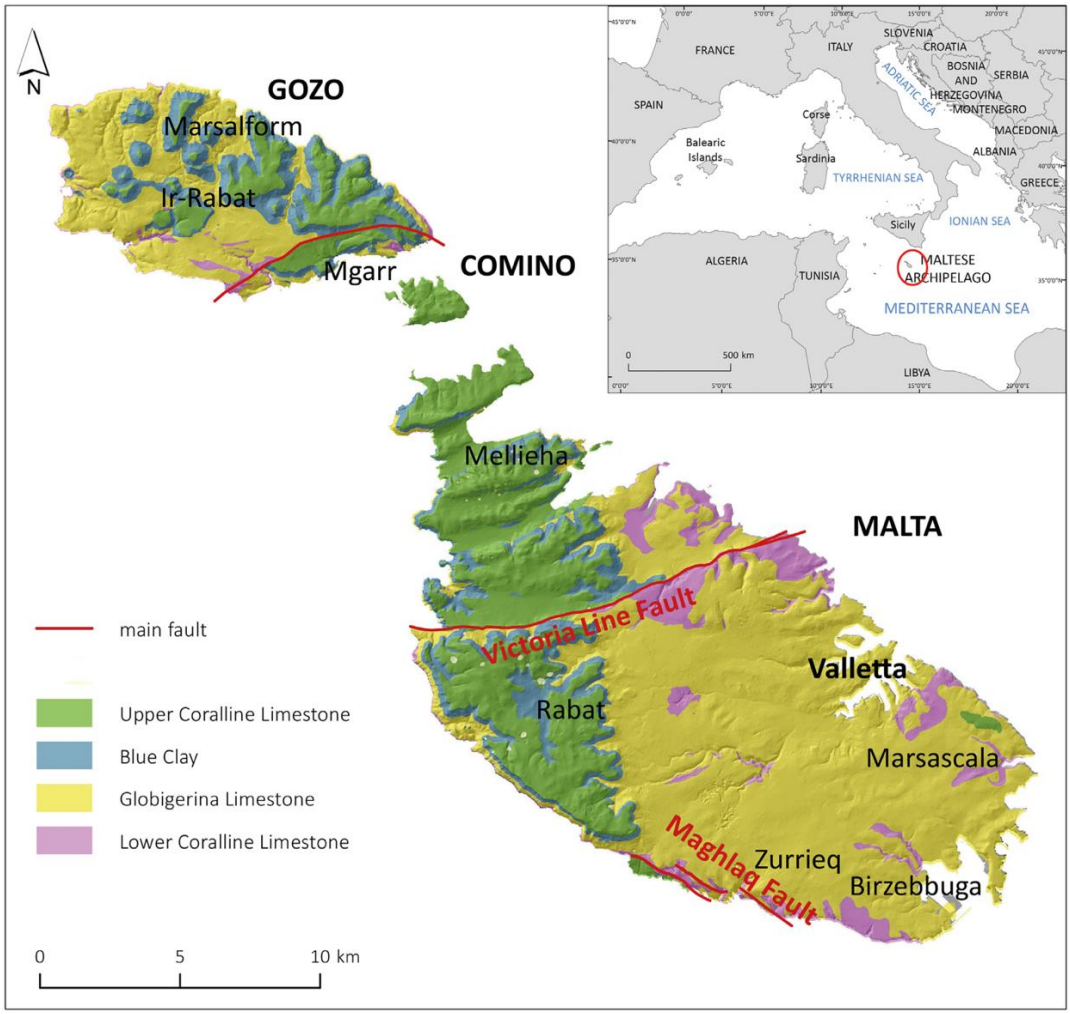

Fig 1: The overview map shows the Mediterranean with the Maltese Archipelago pointed out (red circle). The zoomed map of the Maltese Islands shows the outcropping geological formations along with the Victoria Line Fault and the studied Maghlaq Fault. From Furlani et al. (2017).

2. GEOLOGICAL FRAMEWORK

2.1 Regional tectonic framework

2.1.1 Tectonic Evolution of the Mediterranean Region

The tectonic evolution of the Mediterranean is a result of the creation and consumption of the Paleotethys and Neotethys oceanic basins in Paleozoic to Mesozoic times, and the complex interactions between orogenic processes and extensional tectonics from the African-Eurasia convergence since late Cretaceous (Dewey et al., 1989; Rosenbaum et al., 2002). The region is dominated by a system of fold-and-thrust belts with associated foreland and back-arc basins. The fold-and-thrust belts did not originate as a single "alpine" orogenic cycle, but are different in terms of timing, tectonic setting and internal architecture (Cavazza and Wezel, 2003).

The Western Mediterranean Sea is composed of numerous small basins that developed from Oligocene times until the present from the convergence between Africa and Europe (Dewey et al., 1989; Rosenbaum et al., 2002). Major extensional tectonics developed due to the slab roll back of the subducting Adriatic plate (African promontory), leading to the creation of several back-arc basins, such as the Tyrrhenian Sea, the Aboran Sea, the Ligurian Sea, the Algerian-Provençal Basin, and the Valencia Trough, (Malinverno and Ryan, 1986; Gueguen et al., 1998; Rosenbaum et al., 2002). The age of the basins are greatest to the north and west, and decreases towards the south and east (Dewey et al., 1989; Rosenbaum et al., 2002). The eastern part of the Mediterranean is recognized as an older and more stable area than the western part, and it is likely to consist of remnants of a Mesozoic passive margin and oceanic crust (Neotethys) (de Voogd et al., 1992 from Biju-Duval and Dercourt, 1980; Reuther and Einsbacher, 1985).

2.1.2 The Pelagian Platform

The Pelagian Platform constitute the northern part of the African continental plate and consist of Mesozoic-Cenozoic carbonate rocks which are underlain by continental basement of unknown age (Reuther and Eisbacher, 1985; Civile et al., 2010). Four structural domains can be recognized on the platform: 1) The Malta Escarpment, 2) the Apennine-Maghrebian fold-and-thrust belt, 3) the shallow shelfs (e.g., Hyblean-Malta Plateau), 4) and The Pantelleria Rift system (Fig. 2). To the east, the platform margin is marked by the NNW-SSE trending Malta Escarpment, which descend to depths more than 3000 meters before entering the Ionian Basin. It is likely that the escarpment follows an older crustal fracture zone (Reuther and Eisbacher,

1985). Along the northern and western margin of the Pelagian Platform lies the Apennine-Maghrebian fold-and-thrust belt which developed during the collision between the African and the European plates from late Cretaceous to Early Pleistocene (Elter et al., 2003). The African plate was only partially subducted under the European plate, due to the thicker and more buoyant crust of the Hyblean-Malta Plateau (Gardiner et al., 1995). This resulted in the formation of the shallow shelfs that constitute the Pelagian platform, and the separation of the Ionian Basin from the Western Mediterranean. The Malta Plateau lies on the northeastern shoulder of the Pantelleria Rift System.

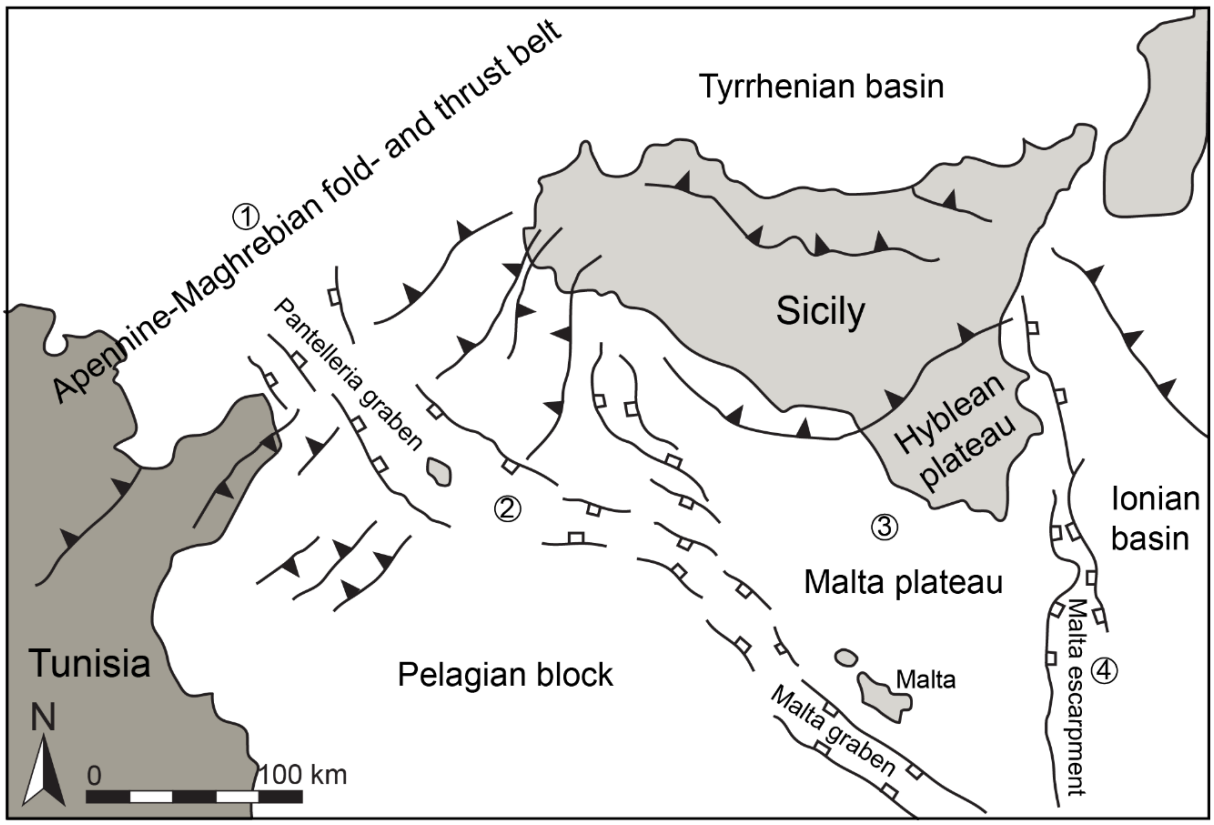

Fig 2: Overview of the Middle Mediterranean with (1) the Apennine-Maghrebian fold-and-thrust-belt; (2) the WNW-ESE oriented Pantelleria Rift System; (3) the Malta Plateau with the Maltese Islands; (4) The Malta escarpment. From Granath and Casero (2004).

In the Central Mediterranean Sea, between Sicily and Tunisia, lies the NW trending Pantelleria Rifts System. This is also known as the Sicily Channel Rift Zone, developed in the foreland associated with the Apennine-Maghrebian fold-and-thrust-belt. This 100 km wide and 600 km long rift system is composed of the three Miocene-Pliocene grabens known as the Pantelleria, Linosa and Malta Troughs (Reuther and Eisbacher, 1985; Dart et al., 1993). The troughs were created during N-S-directed continental rifting in Neogene-Quaternary times and was later filled with Plio-Quaternary deposits (Gardiner et al., 1995; Civile et al., 2010). Maximum water depth in the troughs ranges between 1300 m to 1700 m (Morelli et al., 1975), and the crustal

thinning has been up to 17 km (Civile et al., 2008). Other geological features produced from the continental rifting are the two volcanic islands called Pantelleria and Linosa, and several submarine volcanic edifices with ages 10 Ma to present (Bosman et al., 2008). The origin of the Pantelleria Rift System is not fully understood, and there are different interpretations about what governed the creation of the rift. Argnani (1990; 2009) proposes the rifting to be controlled by slap-pull forces related to the opening of the Tyrrhenian Sea, while others (Jongsma et al., 1985; Reuther and Eisbacher, 1985; Cello, 1987) suggest the driving force to be a major dextral shear zone in front of the African-European collisional belt, where the troughs are interpreted as pull-apart basins. An interpretation by Illies (1981) considers the Pantelleria Rift System to be a product of intraplate rifting and rotation of the regional stress conditions.

2.1.3 The Maltese Islands

The Maltese Islands are located on the Malta Plateau, about 200 km south of the convergent margin of Europe and Africa, and consist of the three islands Malta, Gozo, and Comino (Fig. 3). The archipelago is dominated by normal faulting that formed a series of ENE-WSW trending horst and graben structures (Dart et al., 1993). There are two distinct tectonic features visible on the Malta Island itself; (1) the Victoria Lines Fault, which marks the southernmost extent of the horst and graben structures, which has a maximum displacement of 90 m and strikes ENE-WSW; (2) the Maglaqh Fault on the southwestern coast, which is the only large, onshore fault with the same trend as the Pantelleria Rift system. As fieldwork for this project were conducted along the Maglaqh fault, it is further described in the following section.

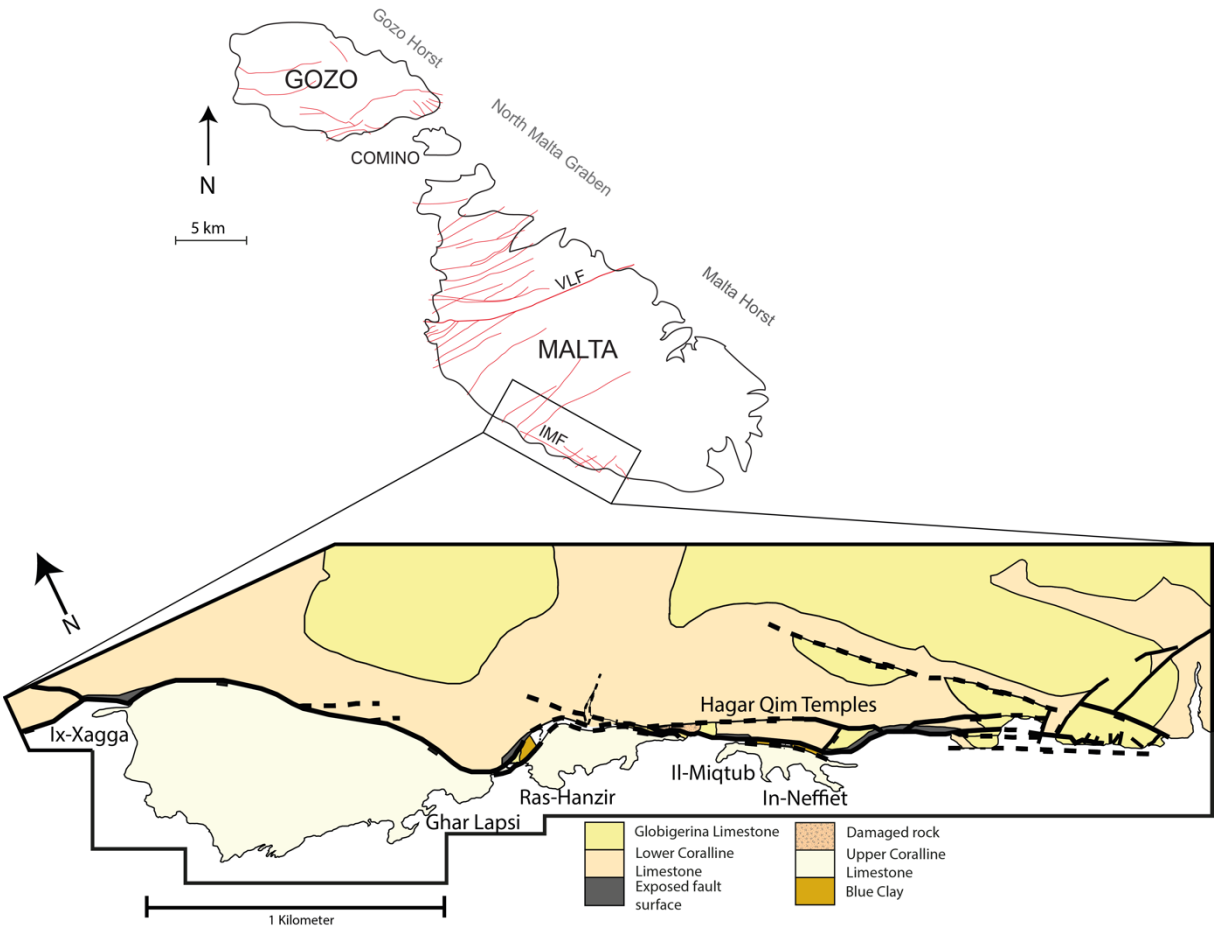

Fig 3: Map of the Maltese archipelago illustrates the largest faults in red. Modified from Pedley et al. (1976); Michie et al. (2014); Dimmen et al. (2017). Geological map of the study area along the Maghlaq Fault on the southwestern coast of Malta. Modified from Bonson et al. (2007).

2.1.4 The Maglaqh Fault

The Maglaqh Fault is a normal fault with a displacement up to 210 m and extension up to 500 m wide, and cuts the Oligocene-Miocene pre-to syn-rift carbonates (Reuther and Eisbacher, 1985; Bonson et al., 2007). The fault zone is ESE-WNW oriented and runs parallel to the southwest coast of Malta, and is hence interpreted to be the outermost master fault of the Pantelleria Rift System (Illies, 1969) (Fig. 3). The geometry of the fault is left-stepping with fault bends interpreted to be points of segment-linkage that is dipping 60-75º towards the SSW. Footwall slip surfaces consists of polished Lower Coralline Limestone and cataclasites with movement striations and lenses of derived footwall material (Bonson et al., 2007). Normal drag along the fault has caused the hangingwall beds to fold and some places overturn. Deformation in the hangingwall is also characterized by synclines and anticlines caused by minor contractional faults and extensional faults, respectively (Reuther and Eisbacher, 1985; Dart et al., 1993). These structures are exposed onshore but are below seismic resolution.

2.2 Stratigraphic Framework

The Maltese Islands consist of a shallow water, Oligocene-Miocene pre- to syn-rift sedimentary succession (Pedley et al., 1976). This subdivision is established with respect to the Pantelleria rifting event (Fig. 4). The succession is of almost only pure marine carbonates, further recognized as Lower Coralline Limestone, Globigerina Limestone Formation, Blue Clay Formation, Greensand Formation, and Upper Coralline Limestone, described in more detail in the following subchapters.

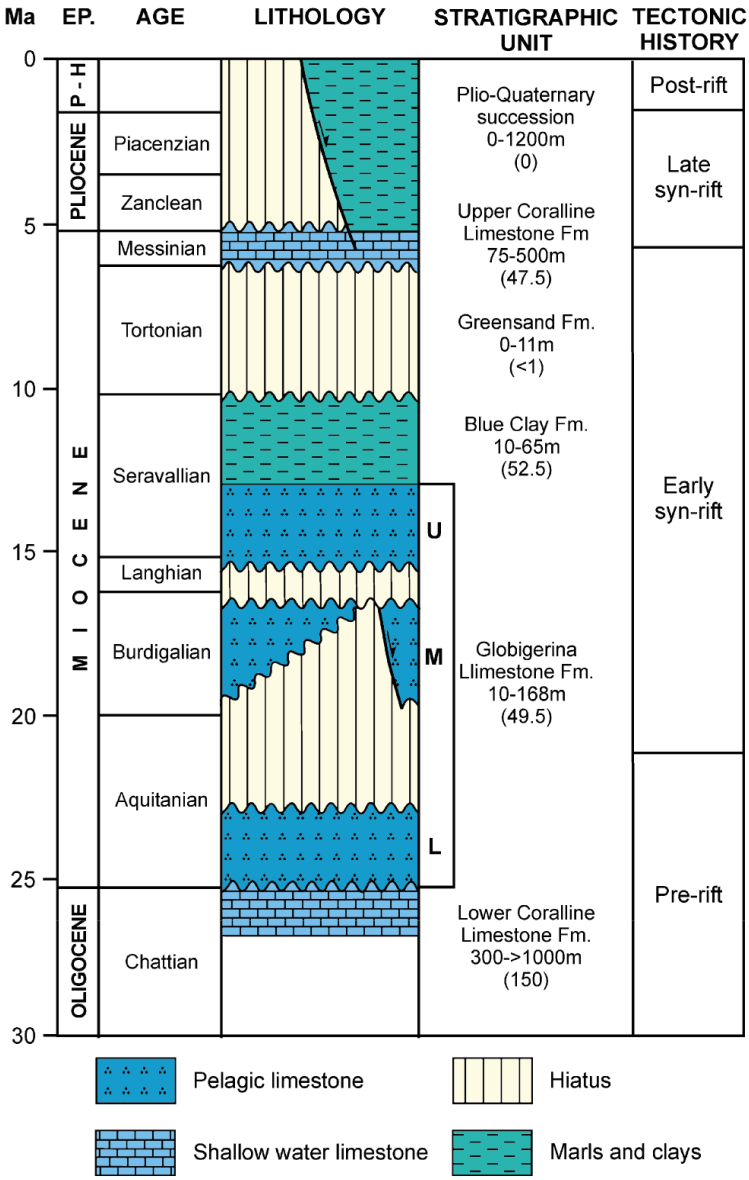

Fig 4: Stratigraphic log of the Oligocene-Quaternary sediments of the Maltese Islands. The carbonate succession can be subdivided into pre-, syn- and post-rift deposits with respect to the Pantelleria rift event. After Bonson et al. (2007) modified from Dart et al. (1993).

2.2.1 Pre-rift succession

The Lower Coralline Limestone (LCL) and the Lower Globigerina Limestone (LGL) compose the pre-rift deposits found on the Maltese Islands. At the base of the succession the Oligocene LCL has been observed to be up to 140 m thick, although the total thickness of the formation have been found to be up to 1000 m (Pedley et al., 1976). The LCL crops out along the western coast of Gozo and Malta where it forms steep cliffs. The formation is mainly made up of massive beds of yellow biomicrites, which are rich in benthonic foraminifera, overlain by pale-grey bedded coralline algal limestones. The upper 10 m of the LCL consist of cross-bedded, coarse, bioclastic limestone with echinoids, marking the top of the formation (Pedley et al., 1976). Deposition of the LCL formation took place in a shallow marine gulf, which later developed into open marine conditions (Felix, 1973). The overlaying Globigerina Limestone Formation (GL) has its name from the high content of planktonic foraminifera, and has a thickness variation from about 23 m to about 207 m across the islands. Only the Lower Globigerina Limestone Member (LGLM) is considered to be deposited before the rifting event, and hence part of the pre-rift succession. The LGLM consist of massive bedded, globigerinid biomicrites, and is recognized by its yellow color and the characteristic honeycomb weathering pattern (Pedley et al., 1976). An eroded bed of phosphorite conglomerate, which holds fossils of molluscs, coral cast and teeth of sharks, marks the top of the LGLM.

2.2.2 Syn-rift succession

The syn-rift succession is subdivided into an early syn-rift phase and a late syn-rift phase. The early syn-rift succession comprises the Middle (MGLM) and Upper Globigerina Limestone Member (UGLM), Blue Clay Formation (BC), Greensand Formation (GF), and the lower sequences of the Upper Coralline Limestone Formation (UCL).

Early syn-rift phase

This early stage is characterized by neptunian dikes, minor fault related thickness variations, and minimal fault related bathymetric relief. Facies distribution is significantly controlled by faults and growth faults; for instance, in the Pantelleria Rift stratigraphic wedges has formed on the hanging-wall dip-slopes due to rotational growth faulting (Dart et al., 1993). The maximum thickness of the MGLM and UGLM are 100 m and 14-18 m, respectively. These shallow-water, globigerinide biomicrites are pale-grey and pale yellow and are separated by another bed of phosphorite conglomerate (about 0.5 m thick) with similar characteristics to the bed separating LGLM and MGLM (Pedley et al., 1976). Above the UGLM follows the BC,

which has a maximum thickness of 75 m and consist of slightly consolidated hemipelagic clays and marls composed of kaolinite, glauconite and not more than 30% of carbonate material (Pedley et al., 1976; Micallef et al., 2013). The depositional environment to the BC is likely to be an open marine setting with water depth up to 150 m. The GF overlaying the BC is rarely thicker than 1 m and is composed of poorly consolidated glauconitic limestone (Dart et al., 1993). In fresh sections, the formation is recognized by a greyish color due to the high content of black or dark green glauconite grains. When weathered, breakdown of the iron oxides gives the rock an orange-brown color. The intense bioturbation found in the GF indicates shallow marine conditions as the main depositional environment (Pedley et al., 1976). The overlaying UCL is a shallow water reef complex and holds many similarities to the LCL in regard to color and algal content. It is subdivided into three sequences, where the two lower subdivisions of the formation are part of the early syn-rift succession. For the first sequence, the facies consist of yellow, fine grained biomicrites, brown micrites which turns into coarser grained lithoclast of biosparite. Furthermore, the facies are rich in diverse fauna and flora, such as coralline algal, bivalves, echinoids, brachiopods, and colonies of bryozoans (Pedley et al., 1976). The second sequence in the UCL contains oolitic limestones and coarser grained bioclastics. Coralline algae and patch reefs with fauna of different bivalves, gastropods and corals indicates water depths of less than 10 m in a shallow platform environment (Bosence and Pedley, 1982). Throughout the Maltese Islands, the UCL is highly exposed to erosion, and as a result, the thickness of the formation varies from 1m to 162 m (Felix, 1973; Pedley et al., 1976).

Late syn-rift phase

The late syn-rift phase consists of the third and uppermost division in the UCL, overlain by Plio-Quaternary carbonate mudstones. Most of the deposits in this division of the UCL are cross-bedded, oolitic, pelletoidal and bioclastic limestones, which indicate a shallow subtidal environment. Reduction and absence of micro-and macrofauna and the presence of at least one stromatolite horizon also suggests intertidal and supratidal beds (Pedley et al., 1976). When the central Mediterranean was reflooded, Pliocene-strata composed of marls and carbonate muds were deposited onto the UCL. However, these sediments are absent onshore, while the Quaternary deposits are patchy and restricted to some areas on Malta (Dart et al., 1993).

2.2.3 Post-rift succession

Today the sea bed offshore Malta shows a smoothed relief relative to the underlying structure, and the historical seismicity support the interpretation of late Quaternary biogenic, hemi-

pelagic, and tubiditic muds to be post-rift deposits (Jongsma et al., 1985; Dart et al., 1993). Whereas the sediments onshore consist of caliche soil profiles, alluvial fan deposits and calcrete breccias as a result of degradation of fault scarps (Pedley et al., 1976).

3 THEORETICAL BACKGROUND

This chapter presents the theoretical background for the thesis. Some fundamental theory behind faults and fault zone architecture will be presented first, before a brief presentation of the theory behind seismic expression.

3.1 Fault zone architecture

Brittle fault zones are lithologically heterogeneous and represent anisotropic discontinuities in the upper crust (Caine et al., 1996; Faulkner et al., 2010). In three dimensions, faults are known to have a complex geometry and high variability in internal properties (Childs et al., 1997; Manzocchi et al., 2010). A fully developed fault zone contains a fault core and a damage zone, which further inherent different structural fabrics and deformation mechanism that result in different permeability properties (Chester et al., 1993; Caine et al., 1996). A fault core is where most of the displacement is accommodated, and can be composed of one or more slip surfaces, fault rocks (breccia, gouge, and cataclasite) and lenses (Sibson, 1977; Chester and Logan, 1986; Braathen et al., 2009). The fault core normally becomes thicker and more continuous as the fault zone matures (Micarelli et al., 2006). Permeability normally decreases in the fault core as the rock fabric changes from fracture dominated to high strain products, such as cataclasites, and may act as barriers or baffles. The damage zone is a fault-related fractured rock volume that bounds the fault core (Faulkner et al., 2011). The highest permeability in a fault zone is typically found in the damage zone due to high fracture density, and hence, this zone can serve as a conduit for fluids (Billi et al., 2003; Micarelli et al., 2006; Agosta et al., 2007).

Limestones and dolomites are considered to be relatively competent strata in terms of mechanical behavior, compared to shale and evaporites. This make them susceptible to brittle failure and fault nucleation (Billi et al., 2003; Ferrill and Morris, 2003). Additionally, carbonate sediments and rocks are prone to diagenetic alteration, particularly cementation, dissolution and pressure solution (Peacock et al., 1998; Eberli et al., 2003). Hence, they commonly stand out as heterogenous rocks, and high heterogeneity are retained in carbonate-hosted fault zones (Fig. 5).

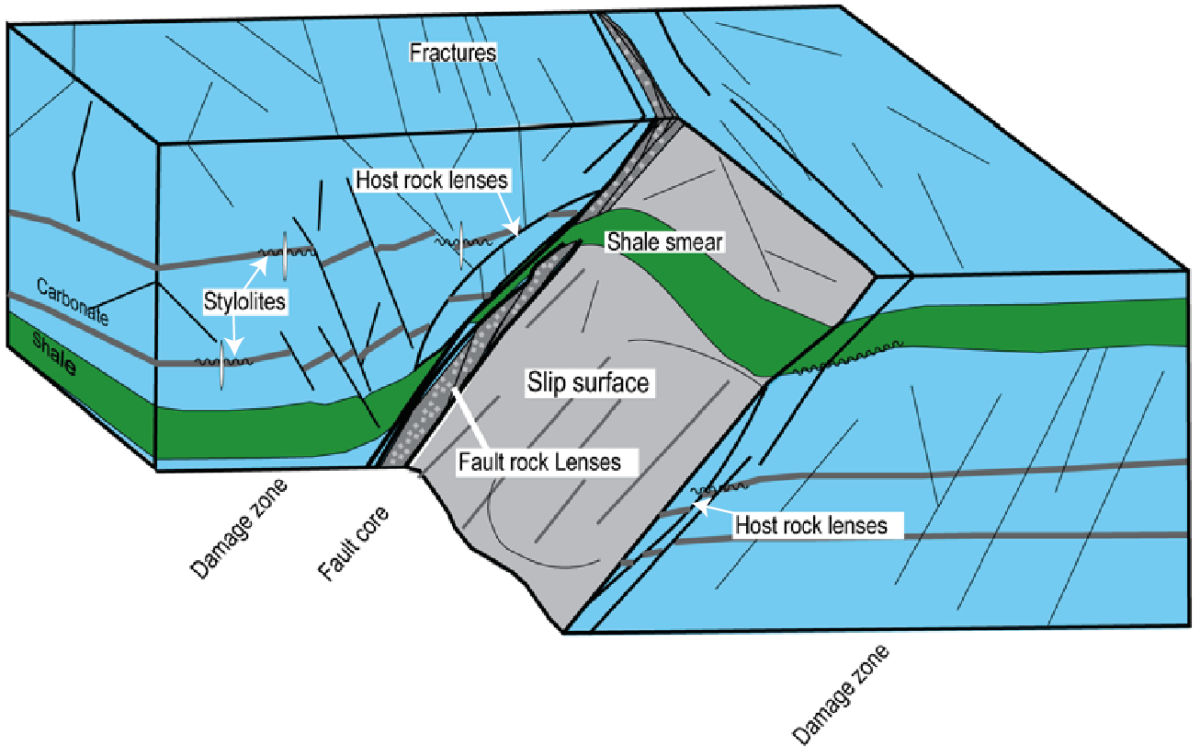

Fig 5: Fault model showing common structures encountered in a carbonate and shale fault zone. After Bastesen (2010) modified from Braathen et al. (2009).

Different deformation mechanism in lithofacies occur due to textural differences. For instance, high porosity grain-dominated carbonates tend to deform on the grain-scale, which often lead to the formation of cataclasites. Whereas deformation in low porosity grain-dominated carbonates and high porosity micrite-dominated carbonates tend to fracture and become brecciated (Billi et al., 2003; Michie et al., 2014; Cooke et al., 2018). Due to the different fabric in fault rocks, fault rock thickness and continuity should be taken into account as it is a key factor in determining their impacts they have on fluid flow (Micarelli et al., 2006; Agosta et al., 2007; Cooke et al., 2018). The heterogeneity of the fault core may become higher with greater displacement and variety of lithofacies juxtaposed. In addition, heterogeneity of fault rocks are higher in structural complex zones, such as breach relay zones, and areas of linkage and overlapping of fault segments (Childs et al., 1997; Bonson et al., 2007). Zones like that, are largely controlled by mechanical stratigraphy in carbonate sequences.

3.2 Seismic response

Seismic data can be gathered on land or at sea and are acquired with acoustic sources and receivers (Fig. 6). Waves of sound energy are shot from the gun into the subsurface where it is

reflected due to contrasts in acoustic impedances from geological interfaces. The reflected energy is then recorded by each receiver on the cable.

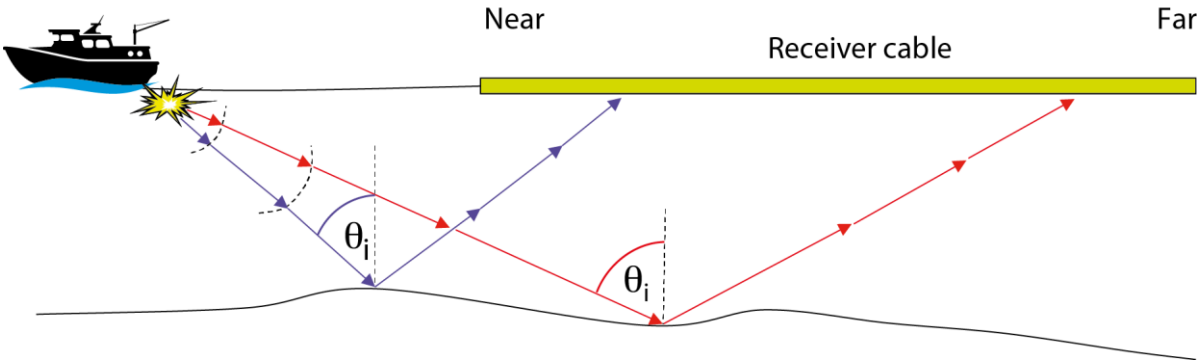

Fig 6: Acquiring seismic data at sea is typically done with a towed gun and a receiver cable. Rays are perpendicular to wavefronts and angle of incidence increases with offset. After Simm et al. (2014).

Two types of seismic body waves are recognized: compressional waves (P-waves) and shear waves (S-waves). P-waves propagate by compressional and dilational strain in the wave travel direction. Whereas, the S-waves propagate by a pure shear strain perpendicular to the wave travel direction. The progradation velocity of seismic waves through a material, are determined by the density and elastic moduli (Kearey et al., 2002). The seismic response of propagating seismic wavelets through layers originate from acoustic impedance (AI) boundaries. This is measured by the reflection coefficient as a function of AI, which is given by the P-wave velocity (V) and bulk density (r) of a rock (Sheriff, 2002; Herron, 2011).

Identification of reflections from an acoustic impedance boundary, also called a horizon, depends upon the seismic data quality, impedance relationship and available well data (Herron, 2011). In cases with many close spaced impedance boundaries the reflection seismic data represent a composite response (Kearey et al., 2002). Such composite response arises from the interference between different seismic characters (amplitude and phase of waveform) of individual impedance boundaries. The individual response of each reflection coefficient to the input wavelet generate destructive and constructive interferences when convolved to a composite response (Fig. 7). Furthermore, the composite response is highly dependent upon the width of the seismic pulse (length of the wavelet) and the interval between impedance contrast (Herron, 2011; Simm et al., 2014).

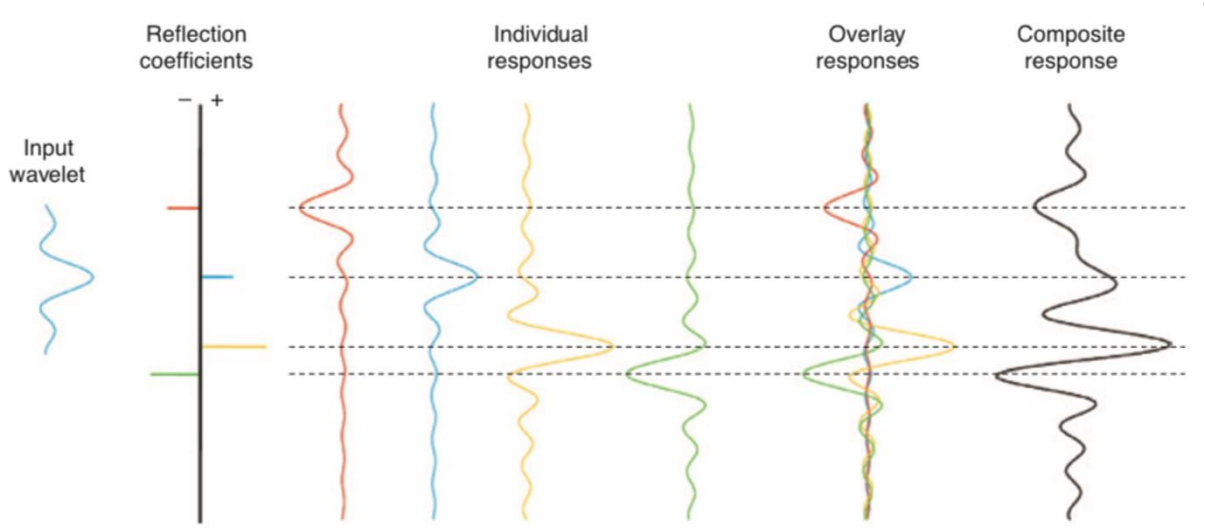

Fig 7: The convolution model with the individual responses of each reflection coefficient to the input wavelet. The sum of these responses generates the composite response formed by constructive and destructive interference. After Herron (2011).

3.3 Seismic resolution

Seismic resolution is defined as the ability to separated and detect features (i.e., top and base of a rock layer) in the subsurface, and is mainly controlled by wavelet properties, such as frequency band and wavelet shape (Sheriff, 2002; Simm et al., 2014). Therefore, there is a lower limit to the bed thickness and geological lineaments that can be resolved before becoming a composite reflection. As a general rule of thumb the vertical resolution is a quarter of a wavelength (λ/4) (Widess, 1973). Lateral resolution is defined by the Fresnel zone (λ/2) (Sheriff, 1977) and is the part of an interface from which seismic signals are reflected. Migration of this zone lead to better lateral resolution. The seismic resolution is determined by the dominant wavelength (λ) of the signal, given by the compressional velocity (Vp) and the dominant frequency (Fd):

$$\lambda = Vp/Fd \qquad (1)$$

Resolution decreases with depth due to absorption of high frequencies and downward increasing seismic velocity. Seismic imaging issues are especially associated with high velocity carbonate reservoirs.

Geological elements, such as normal faults, appear on different scales and the detectability in seismic depends upon the resolution. Fault zones are normally interpreted as 2D surfaces but are in reality 3D narrow zones of heterogenous rocks (Faulkner et al., 2010). Major faults are considered to have high fault scarps and a large downthrow, producing accommodation for

sediments to be deposited, which can be resolved in seismic sections. The fault internal structures, on the other hand, vary in scale and can be on the limit to seismic resolution. Horizontal resolution is lower than the vertical resolution and presents a problem in interpreting faults (Gauthier and Lake, 1993; Long and Imber, 2011). Although, the level of details are limited, damage zones with associated brittle and ductile deformation, can be large enough to be visualized (Townsend et al., 1998; Dutzer et al., 2010). Detection of fault scarp depends upon the steepness of the fault surface in order for it to be illuminated. The seismic signature of faults is strenuous to generalize due to the high variability of heterogenous combinations in terms of lithology, deformation, and fault displacement (Faulkner et al., 2010; Botter et al., 2016).

3.4 Seismic interpretation

Interpretation of seismic images are done by characterizing the reflections and their relations in terms of continuity, character, and reflector spacing. The continuity of a reflection describes the lateral consistency of the horizon. Detection of faults in seismic is done by characterizing the reflection continuity and termination (Lines and Newrick, 2004). Reflector spacing describes the distance between two reflectors and can further give an evaluation of bedding thickness. High-amplitude seismic reflections can function as stratigraphic markers which makes it possible to identify faults and calculate throws of faults.

3.5 Carbonates and faults expressed in seismic

Two important factors for recognizing geological features on a seismic image are the acoustic impedance contrasts and the dimensions of the geologic object (Eberli et al., 2004). Carbonate rocks are susceptible to rapid diagenetic alteration and dissolution which can destroy and create porosity and hence change the pore type and permeability. This results in a large variation of elastic properties and a wide range of sonic velocities in pure carbonates, with Vp from 1700 m/s to 6500 m/s, and Vs from 800 m/s to 3400 m/s. Shallow platform carbonates often have higher velocities than carbonates deposited on deeper water, due to a higher diagenetic potential, and is characterized by a high-amplitude reflection (Anselmetti and Eberli, 1993). On the other side, carbonate reservoirs very often inherent a limited mineralogy composition with a small contrast in velocity. In addition to the resolution issues associated with the increase of seismic velocity with depth, compressional wave attenuation is shown to be greater in carbonates compared to clastics (Adam et al., 2009). Therefore, high velocities and frequency attenuation contribute to poor contrast in acoustic impedance and low resolution, which again

makes it challenging to image carbonates in seismic and to delineate carbonate reservoirs, e.g., Alberta Basin (Wagner, 1997; Skirius et al., 1999). In order to improve seismic interpretations and to better produce constrained reservoir models for carbonates, integrated seismic and petrological data must be used in the seismic inversion (Bosch et al., 2010; Sams et al., 2017).

4 METHODS

This chapter gives an overview of the methods used during the fieldwork in Malta and throughout the generation of the 2D geological models and seismic images from the obtained data. An overview of the workflow used in this thesis is presented in Fig. 8. The following subchapters explain the steps in detail.

Outcrop analogues have been used for decades to provide qualitative and quantitative data that may help better understand and characterize subsurface geology (e.g., Weber, 1987; Dreyer et al., 1992; Brandsæter et al., 2005; Enge and Howell, 2010; Rabbel et al., 2018). Seismic modelling of outcrops brings this one step further, emulating the seismic response of a given geological outcrop model. This provides a better understanding of the seismic imaging of different geological features, which in turn may improve the interpretation of real seismic data from the subsurface. Furthermore, seismic modelling can distinguish between seismic artefacts and real geological structures, thereby narrowing the scale gap between outcrop analogues and seismic data from a subsurface system.

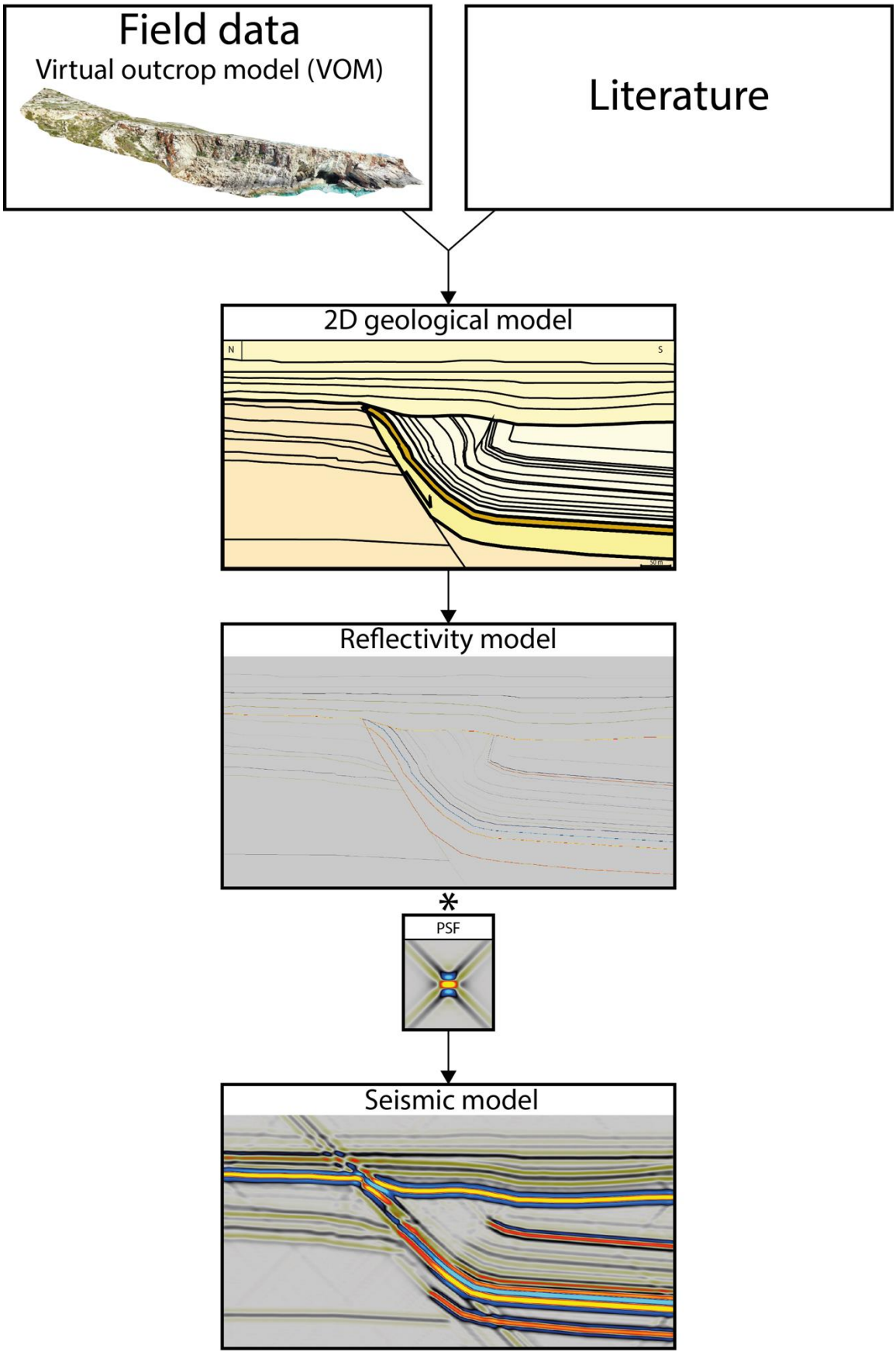

Fig 8: Detailed structural input gathered from the field and well-constrained elastic properties derived from literature are used to create a geological model. The elastic properties are further lead to a reflectivity model. Convolution between the reflectivity model and a Point-Spread Function (PSF) results in a synthetic seismic model.

4.1 Field work and geological modelling

Data was gathered during a two weeks field period in Malta, March 2019, and served as the main fundament for the geological models. Several virtual outcrop data from hangingwall sections of the Maghlaq Fault along the southwestern coast of Malta have been studied. Geological models were made based on interpretation of the virtual outcrop models. Literature was used to supplement where necessary data are missing or inadequate.

4.1.1 Logged section

A sedimentary log of the hanging wall section was conducted at Locality 3 to supplement the lithological characteristics, mainly grain size and fossil content, which cannot be observed in the virtual outcrop models. A thorough study of the lithology on site is needed in order to get a realistic case when assigning elastic properties from the literature to the different units in the geological model. The Dunham classification system for carbonate rocks was used in the lithological description of each lithofacies. One log is considered representative for all the studied localities since they are situated within the same stratigraphic level. No fresh and easily accessible footwall sequence was found, so data of the footwall strata were acquired with drone-images from an open quarry.

4.1.2 From outcrop to geological model

The main data herein is built on photogrammetry. It is used to make high-resolution virtual outcrop models which create a base for geological models and input to 2D seismic modelling. The data were gathered on the southwest coast of Malta using a drone (DJI Mavic Pro). All the images were captured at 20-30 m distance perpendicular to the outcrops, which are mainly hangingwall cliff sections. Images were captured with at least 60% overlap to ensure adequate coverage. AgiSoft PhotoScan, version 1.3.4., was then used to generate optimized 3D photogrammetric models of the outcrops. The geological interpretations of the outcrop models were carried out in the 3D interpretation software, Lime (Buckley et al., 2019), with focus on mapping the geometries in the hangingwall sections. The interpreted models were then exported as 2D-panels, oriented perpendicular to the Maghlaq fault surface, for further editing in Adobe Illustrator. Adobe Illustrator was used to extrapolate lines and boundaries where outcrop data was inadequate and to assign different colors to individual units. The model was converted to grey scale in order to simplify color codes and to make each unit identifiable in the programming software, Matlab. Through their unique color code, each unit was assigned a

block number and the elastic properties P-wave velocity (Vp), S-wave velocity (Vs), and density. Simultaneously, Matlab was used to read the PNG file of the geological 2D models to get a grid with the grey code. These numerical grids were populated with the assigned block number, Vp, Vs, and density, and stored as four SEG-Y files. SEG-Y files are necessary for doing seismic modelling in the NORSAR software, SeisRoX (Fig. 9).

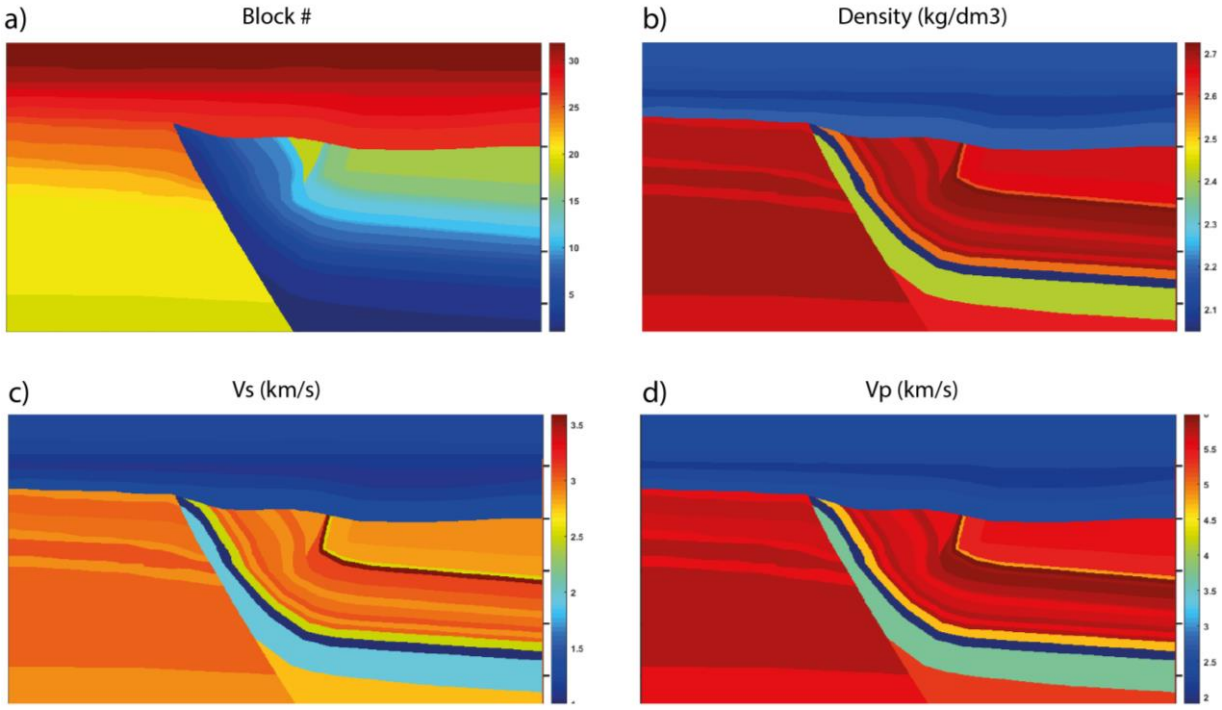

Fig 9: The figure shows an example of the four property grids generated by the Matlab script before exporting them to SEG-Y files: a) block, b) density, c) Vs, and d) Vp. The SEG-Y files display how the elastic properties and block numbers are assigned and distributed in the geological model of Locality 3.

4.2 Seismic modelling: the 2D (3D) convolution method

At this point, 2D geological models with assigned elastic properties have been created and further exported to SEG-Y files. The SEG-Y files are then imported to the SeisRoX software as input cubes, where they are displayed and ready to be employed in 2D. SeisRoX rapidly simulates 2D PSDM seismic images by applying a 2D (3D) PSF-based convolution method. The software allows us to observe the seismic characterization at different scales while varying input parameters such as geological and elastic properties.

In the following, the 2D (3D) PSF-based convolution method used for seismic modelling in this thesis is briefly described. Ray-based modelling of 2D (3D) prestack depth migration (PSDM) point-scatterer (diffraction) responses, also called Point-Spread Functions (PSF), allows for faster and more flexible applications of the 2D (3D) spatial prestack convolution approach

(Lecomte, 2008; Lecomte et al., 2015). Ideally, the PSF is based on parameters such as survey geometry, background velocity model, and wavelet. However, in this thesis the ray-based PSFs used in the 2D (3D) convolution with the reflectivity model are generated from an average velocity, a selected incident angle, the degree of illumination in geological dips, and a wavelet. This is justified by not having a specific data set to compare with, hence no existing or specifically designed survey geometry and velocity model. It also allows a focus on the geological aspects of the seismic imaging as originally targeted for the present work. A standard of 45º maximum reflector-dip illumination (steeper dips will not be imaged) and an incident angle of 0º were further applied during the present modelling as good standard values and for the sake of simplicity. For more information and illustration on the impact of varying these parameters, see Andersen (2020). Zero-phase Ricker wavelets of 20, 40, and 60 Hz as dominant (peak) frequencies were selected. These peak frequencies are characteristic of seismic data for subsurface targets on the Norwegian continental shelf (e.g., Eide et al., 2018). The Ricker wavelet (Ricker, 1940) is defined by a single central frequency and has only two side lobes (Simm et al., 2014). It is a standard wavelet for synthetic seismic modelling due to its simplicity, but other wavelets are studied in Andersen (2020).

In practice, a Fast Fourier Transform (FFT) is applied to a so-called PSDM filter generated in the wavenumber domain (i.e., the Fourier domain related to the spatial one) from the selected parameters. This application produces a ray-based PSFs in the spatial domain, which is an estimation of the point-scatterer (diffraction) PSDM response for the chosen imaging zone. For simplification, a single PSF will be applied per image in the 2D (3D) spatial convolution with the reflectivity model. After FFT is applied to the reflectivity model, the convolution is most efficiently done in the wavenumber domain by multiplying the PSDM filter with the reflectivity model. The inverse FFT of that product leads to the desired (spatial) seismic image in depth. This method of modelling is highly efficient and low in computing cost (Fig. 10).

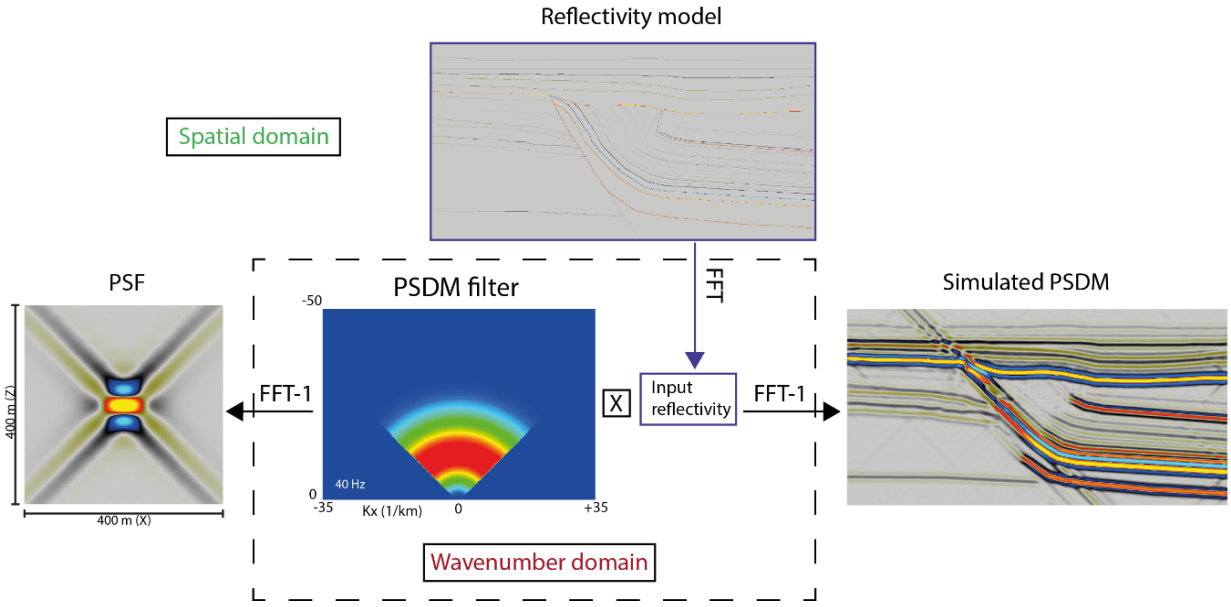

Fig 10: The FFT of the reflectivity model gives the input reflectivity in the wavenumber domain which allows multiplication with the PSDM filter. The simulated PSDM image display the resulting product in the spatial (depth) domain. The PSDM filter in the wavenumber domain corresponds to the PSF in the spatial domain. A figure of the input reflectivity in the wavenumber domain is not possible to retrieve from SeisRoX. See Lecomte (2008) Figure 14 and 15 for examples.

4.3 Database and experimental design

A total of three geological models were built to function as the most realistic base cases. Dimensions of the models have been enlarged to gain seismic scale by increasing the original pixel size from 0.2x0.2 m^2 to 1x1 m^2. Scaling can be done because faults and folds are fractals, called self-similar. Self-similar fractal properties, such as geometry, repeats at different scales (Fossen and Gabrielsen, 1996 and references therein). The quantitative data added from literature are qualified to be representative of the limestone sequence in Malta.

4.3.1 Model set-up

In addition to the base cases, models have been designed with variation in fault geometry, lens size, and properties. Then, the models are further compared in order to systematically identify seismic signatures at different dominant frequencies for each of the respective scenarios (Fig. 11). All the scenarios were modelled at each of the studied localities, which resulted in a total of 90 seismic models (Fig. 12).

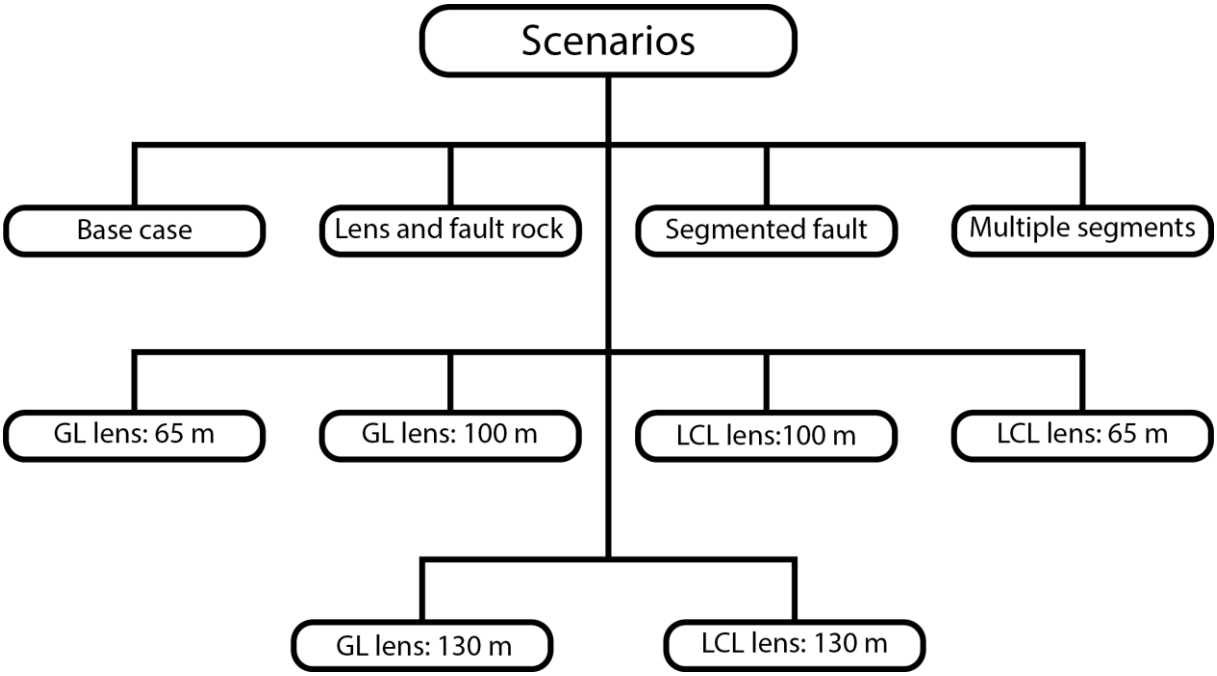

Fig 11: The chart flow contains all the different scenarios modelled in this thesis. The different scenarios are mainly variation in fault geometry, fault structure, lens size (65, 100, and 130 m thick), and properties.

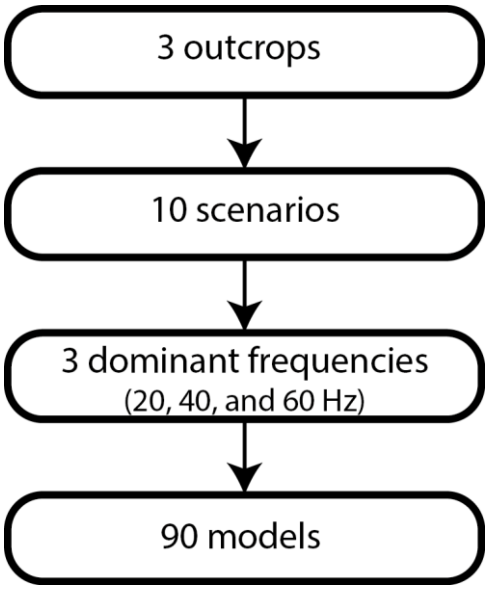

Fig 12: A total of 90 models were generated in this thesis. The models are based on three different outcrops along the Maghlaq Fault. Each of them was modelled with the different scenarios listed in Fig. 11. Every scenario was modelled at the three frequencies: 20, 40, and 60 Hz.

4.3.2 Elastic properties

Pickett (1963) introduced the relationship between Vp and Vs from well data as a lithology indicator. Through his laboratory research, he determined the Vp/Vs value to be 1.9 for clean limestones and 1.7 for calcareous sandstone. Later on, Anselmetti and Eberli (1993) found that the ratio normally falls between 1.8-2.0. for rocks with high Vp. Therefore, it is reasonable to

apply a Vp/Vs value of 1.9 for the relatively homogeneous limestone sequence in Malta, and a Vp/Vs value of 1.7 for Green Sand. Dvorkin et al. (2001) derived a Vp/Vs value of 1.91 for marls from petrophysical analysist of two well logs in the North Sea. This value are used in seismic modelling of the overburden post-rift sediments. A Vp/Vs value of 2.13 was chosen for the Blue Clay Formation (Tosaya and Nur, 1982; Castagna et al., 1993). In order to establish rock densities, the original Gardner relation was used (Gardner et al., 1974):

$$\rho = ((Vp\ x\ 1000)^{0.25})0.31 \qquad (2)$$

Derived from the Vp/Vs values and the Gardner equation 2 for densities, each block in the geological models have been assigned a constant value of density, Vp and Vs. The resulting elastic properties is listed in Table 1. Stratigraphic thicknesses derived from literature are used to constrain thicknesses of the geological formations (Pedley et al., 1976; Dart et al., 1993).

Table 1: The geological formations are given elastic properties based on simple empirical relations from the listed sources.

Formation	Vp (km/s)	Vs (km/s)	Density (g/cm^3)	Vp/Vs	Source
Lower coralline limestone	5,25-5,80	2,76-3,05	2,64-2,71	1,90	Pickett, 1963, Anselmetti and Eberli, 1993
Globigerina limestone	3,70-4,00	1,95-2,11	2,42-2,47	1,90	Pickett, 1963, Anselmetti and Eberli, 1993
Blue clay	1,90-2,50	0,89-1,17	2,05-2,19	2,13	Tosaya and Nur, 1982, Castagna et al., 1993
Green sand	3,00	1,76	2,29	1,70	Pickett, 1963, Castagna et al., 1993
Upper coralline limestone	4,70-5,90	2,47-3,11	2,57-2,72	1,90	Anselmetti and Eberli, 1993
Marls and clay	2,10-2,50	1,10-1,31	2,10-2,20	1,91	Dvorkin et al., 2001
Cemented LCL	6,47	3,41	2,78	1,90	Agosta et al., 2007, Matonti et al., 2012
Damaged host rock	4,4-4,8	2,32-2,53	2,52-2,58	1,90	Agosta et al., 2007, Matonti et al., 2012

5. RESULTS

In this chapter, the results from the seismic modelling of selected geological outcrop models are presented. First, the geological interpretations from virtual outcrop models are addressed, before presenting the seismic images of three base cases in subchapter 5.2.1. Finally, the seismic images of different conceptual geological structures and geometries are presented in subchapter 5.2.2. Geological models and seismic images that were generated for this project but not chosen for presentation herein can be found in the Appendix.

5.1 Geological interpretation from virtual outcrop models

Four outcrops were used to make geological models of the Maghlaq Fault Zone along the southwestern coast of Malta. From west to east, the studied outcrops are located close to Ix-Xagga, Ras-Hanzir, Il-Miqtub, and In-Neffiet (Fig. 13). The aim of the geological interpretation is to identify and document formation boundaries and lithology as well as fault and bed geometries. The virtual outcrop models and the log from Locality 3 were the main data used in the formation of the geological models. Geometries, such as bedding orientation and minor faults and fractures, were obtained from the virtual outcrop models, whereas the log documents the lithological differences.

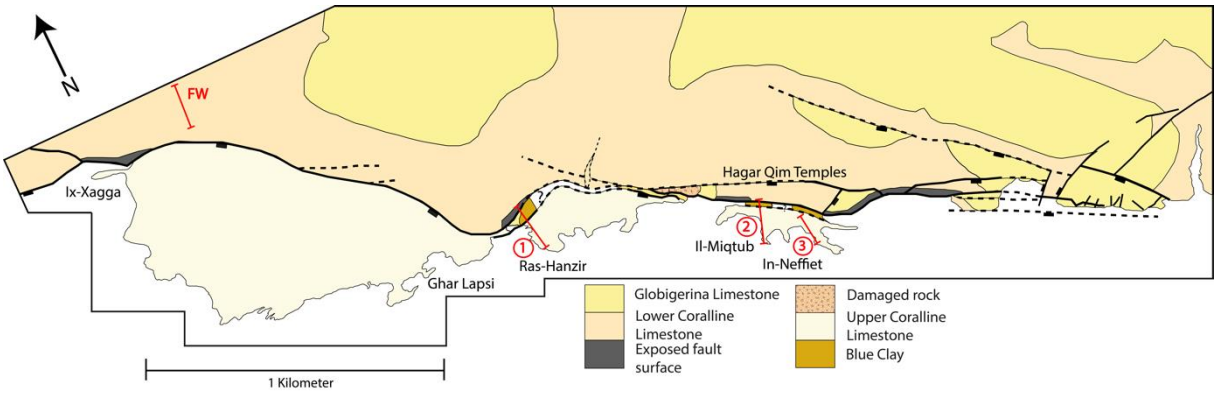

Fig 13: Geological map of the study area and the Maghlaq Fault, oriented WNW-ESE, runs parallel to the southwestern coast of Malta. Localities that were studied along the fault are marked in red. FW indicates the location of the footwall section, whereas the marked localities of 1, 2 and 3 are the hangingwall sections. Modified from Bonson et al. (2007).

Virtual outcrop models were made from a footwall section and the hangingwall sections at localities 1, 2, and 3. The localities lie along the Maghlaq Fault Zone, which is oriented WNW-ESE and runs parallel to the southwest coast of Malta (Fig. 13). Three 2D geological models were made from the interpretation of localities 1, 2, and 3. Based on the outcrop description, the lateral lithological variability is high, especially at localities 2 and 3, because of the layers

that is steeply dipping to the SW. However, the purpose of the 2D models was to give simplified illustrations of the fault zone architecture and the sedimentary succession. A footwall section was studied and implemented in all the geological models. Conceptual ideas were used to extrapolate sedimentological units, both vertically and laterally, in order to make a complete model suitable for seismic modelling. The exact same overburden geometry and lithological properties of marls and clays were provided for all the geological models. Minor lithological variations were added to the LCL and the UCL, which was supported by the stratigraphic log. The folded geometry in the hangingwall strata was based on the interpreted lines from the outcrop model.

5.1.1. Footwall stratigraphic framework

In order to establish the stratigraphic framework of the geological models, data of the footwall stratigraphy were retrieved from an active quarry northeast of Ix-Xagga (Fig. 13). The outcrop was studied to find a footwall section that is representative for the Maglaqh Fault Zone in the geological models. The locality comprises a 40 m high and 190 m wide fresh section in the footwall of the Maghlaq Fault, oriented N-S (Fig. 14). Here, a part of the massive LCL sequence crops out with a very gentle southward dip of 2º. Major fault-related deformation in the footwall strata was not observed in this section; exposure of the Maghlaq Fault was also not observed. However, the Maghlaq Fault forms a fault bend ca. 150 m south from the studied section and crops out at Ix-Xagga, where the fault surface can be studied. Based on the interpretation of Bonson et al. (2007), where deformation related to the Maghlaq Fault was found to be restricted to the hangingwall strata, the studied LCL section is qualified to be implemented in the geological models.

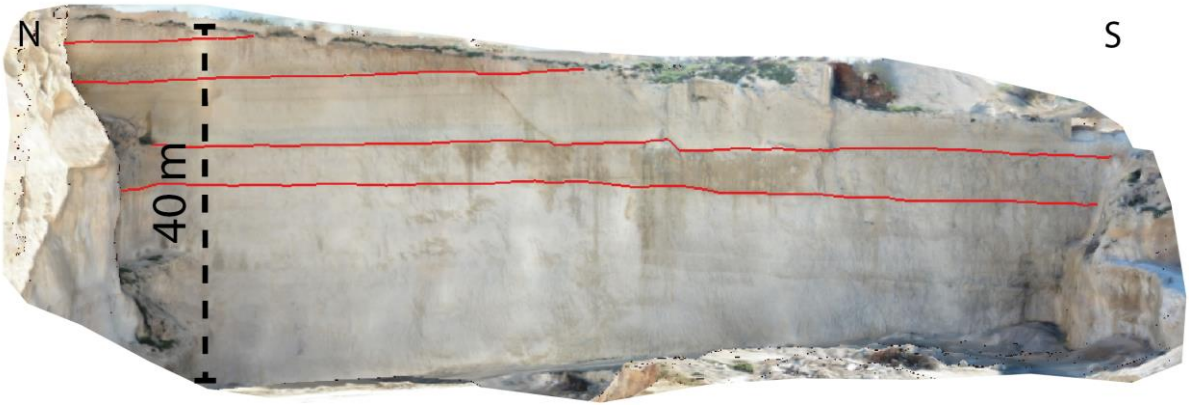

Fig 14: In an open quarry north of Ix-Xagga a 40 m high N-S section of the footwall stratigraphy can be studied from a distance. The interpreted lines (red lines) in the virtual outcrop model illustrates the horizontally oriented footwall strata.

5.1.2 Hangingwall stratigraphic framework

A detailed log was conducted at Locality 3 (Fig. 13) to supplement the virtual outcrop models. To the best of my knowledge, no other detailed logs have been conducted at these localities in recent years. However, in 1976, Pedley et al. reviewed the sequence and structure of the Oligocene-Miocene sediments of the Maltese Island.

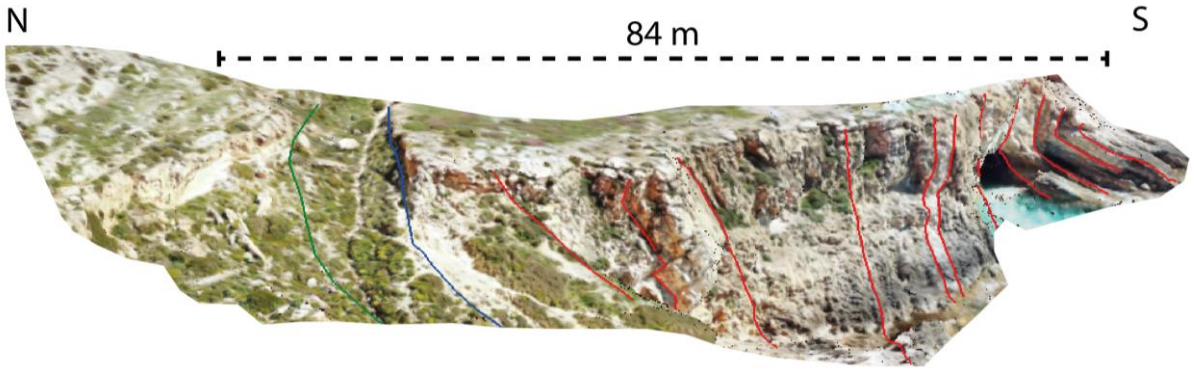

Fig 15: The stippled line indicates where the 84 m long section was logged at Locality 3. The interpreted lines illustrate hangingwall geometries and lithological interfaces (blue: GL-BC interface, green: BC-UCL interface, red: UCL bed geometries).

The acquired log has a total stratigraphic height of ca. 84 m and was recorded through a succession of sub-vertically to vertically-dipping beds (Fig. 15). The outcrop is easy to access and well exposed due to the near vertical geometry of the strata. Starting at the far north of the outcrop in Fig. 15, which corresponds to the bottom of the outcropping succession, a 2 m thick fractured surface of UGLM crops out and is recognized by its yellow color and fine grains (Fig. 16). A few echinoids and nodules were also found. The fractured UGLM is classified as a mudstone. For the next 10 m, a wide eroded area of BC forms a small gully. This area stands out in contrast to the rather resistant limestone succession forming hills and cliffs in Malta. The GS is not present in this section. South of the BC, the near vertical UCL is exposed for ca. 70 m. The first 10 m of the limestone beds consists of fractured and chaotic UCL with shell fragments (e.g., corals). Following this, the UCL turns into undamaged host rock that comprises the remaining 60 m of the log. As a whole, the UCL is dominated by wackestones and packstones, but the first 20 m of the undamaged UCL has lithofacies varying between wackestones, packstones, and mudstones. Except for the mudstones, the beds are rich in fossil, e.g., bryozoans, corals, brachiopods, shell fragments, and bioturbation. Only the latter was found in the mudstones. From 45-57 m, wackestones with bioturbation and shell fragments were logged; and packstones of the same fossil content, but with greater quantity, were logged from 57-65 m. Wackestones, (having a fossil content of gastropods, bryozoans, shell fragments,

burrows, and bioturbation) were present from 65-74 m, after which the logged section was interrupted by a cave with no rock exposure. South of the cave, < 1 m of the section remained, and the exposed rock is an oolitic limestone.

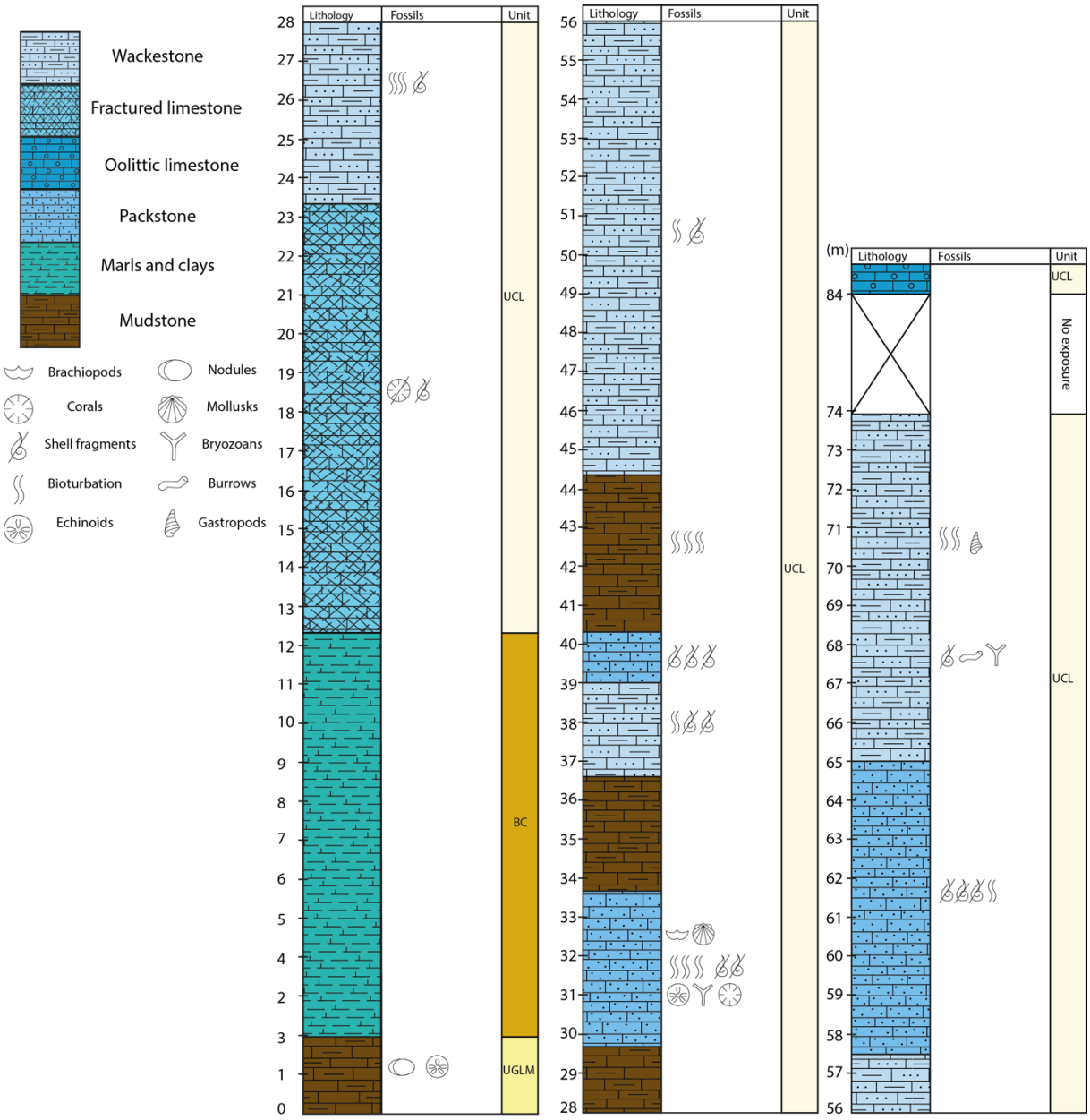

Fig 16: A detailed stratigraphic log of the hangingwall lithologies and fossil content at Locality 3. Logging was conducted on the cliff section indicated in Fig. 15.

5.1.3. Locality 1: Ras-Hanzir

Locality 1 at Ras-Hanzir is located ca. 300 m east of Ghar Lapsi (Fig. 13). This 138 m long outcrop is a N-S oriented cliff section of the fault and its hangingwall (Fig. 17 and 18). In the north part of the locality, a 20 m high exposure of the fault surface composed of polished LCL

cataclasite with lenses of intact LCL is present (Fig. 17c). A layer of brecciated GL (ca. 10 m thick) is found closest to the polished fault surface and was distinguished by its orange color, followed by a layer of weathered BC (ca. 14 m thick). The GS was not identified at this locality. The UCL is folded and exposed for ca. 116 m southward, with a maximum height of ca. 15 m. The first few meters of the folded UCL consists of extensively damaged host rock, followed by minor antithetic and synthetic faults and fractures (Fig. 17b). A 3D virtual outcrop model was made of Locality 1 which was used when interpreting lithology and structural geometries (Fig. 18).The structural setting at Ras-Hanzir is similar to what we found by the fault bend close to Ix-Xagga, but the presence of an additional fault segment makes it more complex at Locality 1.

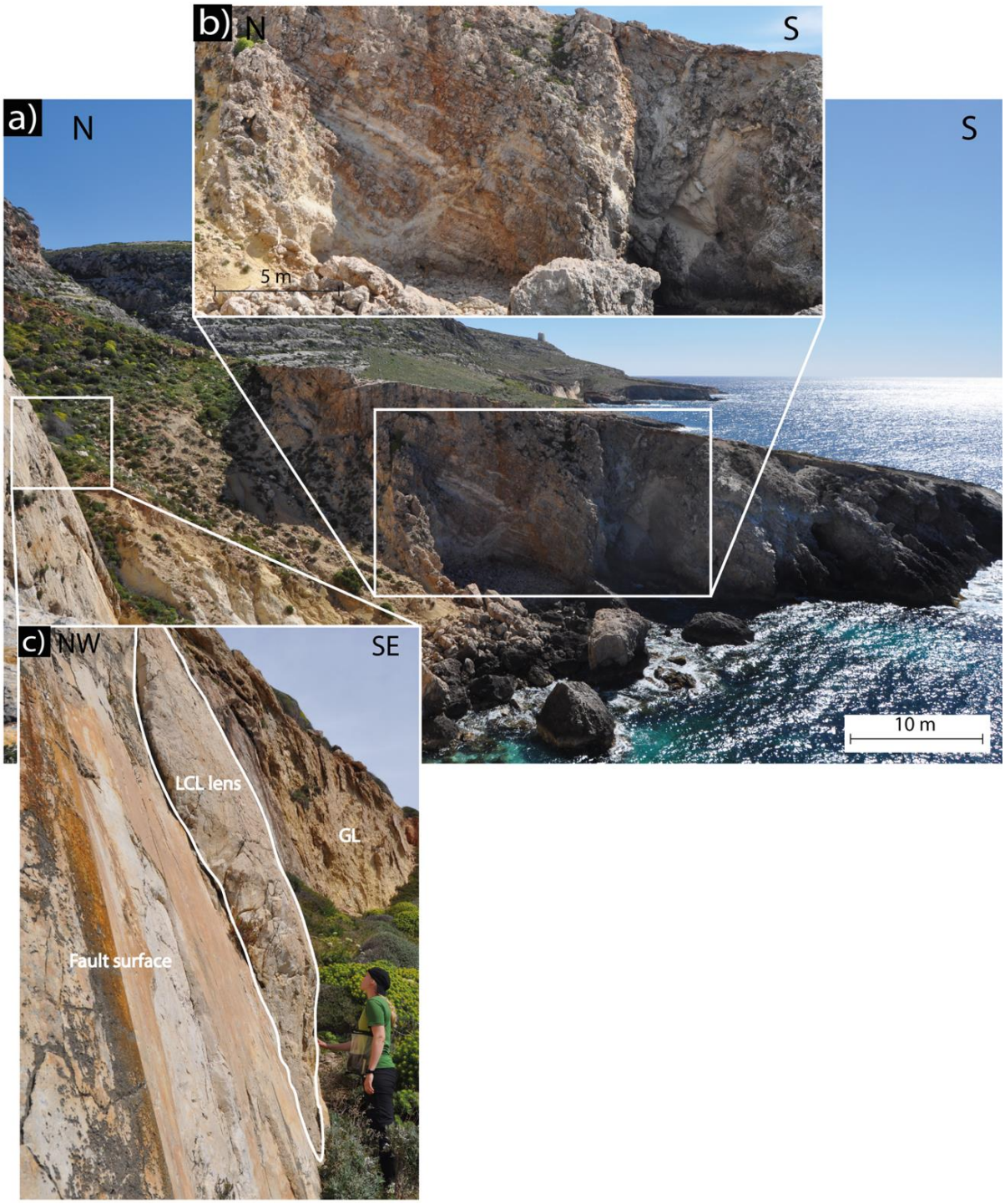

Fig 17: A photomontage of the lithologies and structures at Locality 1 (Ras-Hanzir). a) An overview photo of the hangingwall cliff section showing the polished Maghlaq Fault surface to the north, the steep cliffs of UCL to the south, and the GL and BL in the gully. b) Fault-related deformation, such as minor faults and fractures, are prevalent in the UCL. c) Brecciated GL was found closest to the Maghlaq Fault surface together with lenses of intact LCL.

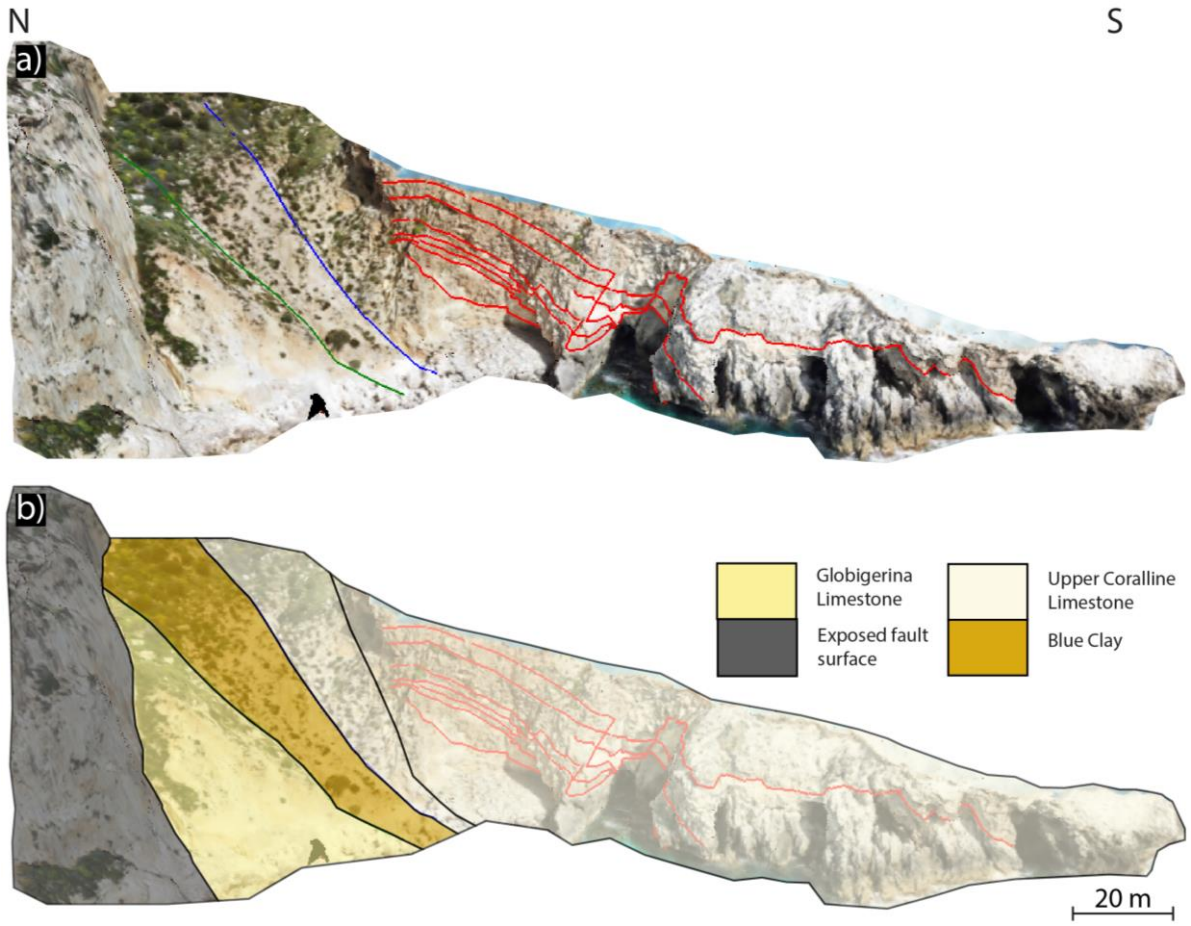

Fig 18: a) A 3D visual outcrop model was made from the hangingwall cliff section at Locality 1. The lines illustrate hangingwall geometries and lithological interfaces (blue: GL-BC interface, green: BC-UCL interface, red: UCL bed geometries). b) A simple illustration of the lithological distribution within the fault zone including the exposed fault surface.

The 2D geological model strikes NE-SW and is oriented perpendicular to the fault surface (Fig.19). The resulting 2D geological model from Locality 1 gives a simplified illustration of the geology in the section. Furthermore, the stratigraphic units have been divided according to the following formation and facies types, which are: LCL, GL, BC, damaged rock, UCL, and marls and clays (Fig. 19). The footwall consists of horizontal layering of the LCL, while the surfaces defining the strata interfaces in the hangingwall are folded to a syncline. In the geological model, the Maghlaq Fault is represented as the discontinuity that intersects the surfaces. This discontinuity results in the juxtaposition of LCL with the folded GL and BC dragged along the fault surface. The Maghlaq Fault is modelled with a mean dip of ca. 59º. Minor antithetic faults and fractures, which intersect the UCL close to where the drag pattern increases in dip, was included in the model. The folded layers of GL, BC, and damaged rock vary slightly in thickness along the fault, whereas an equal thickness was kept throughout the layers when extrapolated.

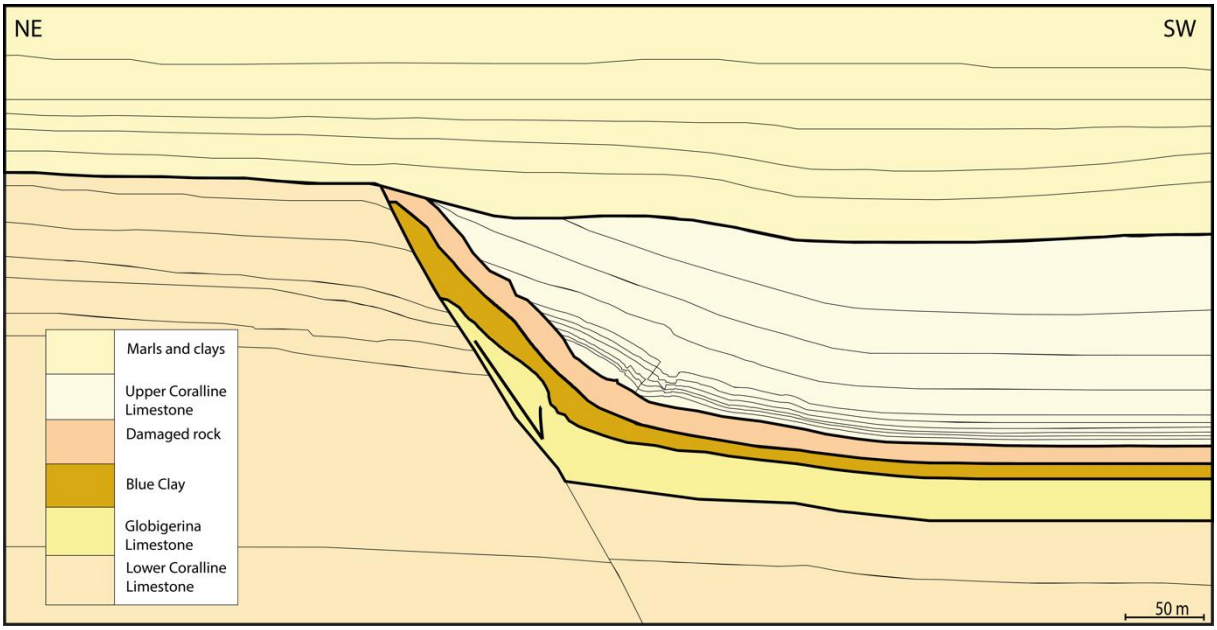

Fig 19: A 2D geological model of the stratigraphic and fault zone architecture at Locality 1.

5.1.4. Locality 2: Il-Miqtub

Locality 2 is an outcrop at Il-Miqtub, located about 750 m southeast of Ras-Hanzir and just south of the Hagar Qim Temples (Fig. 13). The site has an exposure of the Maghlaq Fault surface and a hangingwall cliff section, ca. 127 m long oriented NE-SW, comprising a succession of GL, BC, GS, and UCL rocks (Fig. 20). In contrast to the other localities, a layer of GS (ca. 80 cm thick) was recognized in the fault zone at Il-Miqtub (Fig. 20c). The 70 m long and 11 m high outcropping of UCL has a folded and southward dipping geometry (Fig. 21). The beds have a near vertical dip closer to the Maghlaq Fault, in the NE part of the outcrop, while a shallowing of the dip towards the SW makes the beds dipping more horizontally. It was not possible to access the cliff section of the UCL for measurements. At Il-Miqtub, the structural setting is a segmentation (ca. 15 m wide) with two principal segments of the Maglaqh Fault, where discontinuous GL lenses occur in the corrugations on the exposed slip surface (Bonson et al., 2007). Only one of the principal segments crops out as a polished surface in the LCL footwall (Fig. 20b).

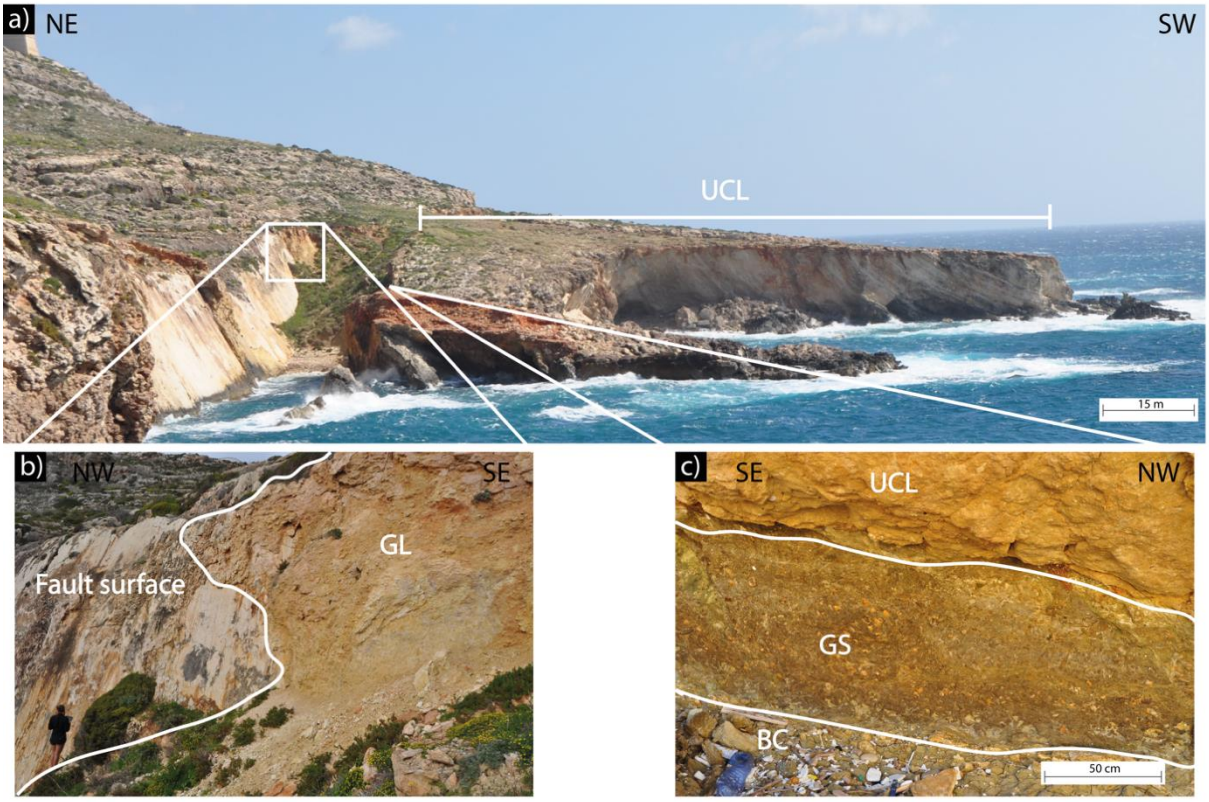

Fig 20: A photomontage of the lithologies at Locality 2 (Il-Miqtub). a) An overview photo of Locality 2. The hangingwall cliff section consists of the UCL, whereas the BC forms the gully close to the exposed Maghlaq Fault surface. b) GL lens on the fault surface (person for scale). c) An 80 cm thick GS layer was found with distinctive contacts to the BC and UCL.

Fig 21: The 3D virtual outcrop model of the hangingwall cliff section at Locality 2, which only contains UCL. The red lines show the folded geometry of the layered UCL.

Along with Locality 1, the creation of a 2D geological model provides a simplified representation of the studied outcrop at Locality 2. When oriented perpendicular to the fault surface, the section modelled strikes NE-SW. Based on the finding from the studied cliff section at Locality 2, the following stratigraphic units were implemented in the model are: LCL, GL, BC, GS, UCL, and marls and clays (Fig. 22). The presence of the thin GS layer at Locality 2 distinguishes this model from the other models. The intersection of the Maghlaq Fault is illustrated by a syncline drag pattern and thinning of GL and BC along the fault surface in the hangingwall. A flattening of the folded layers appears when moving SW from the Maghlaq

fault. Likewise, underneath the overburden strata a decrease in dip occurs to the layers close to the fault surface, (Fig. 22). The fault is modelled with a mean dip of ca. 55º, where the horizontal LCL footwall layers are juxtaposed with the dragged hangingwall layers of GL, BC, GS, and UCL.

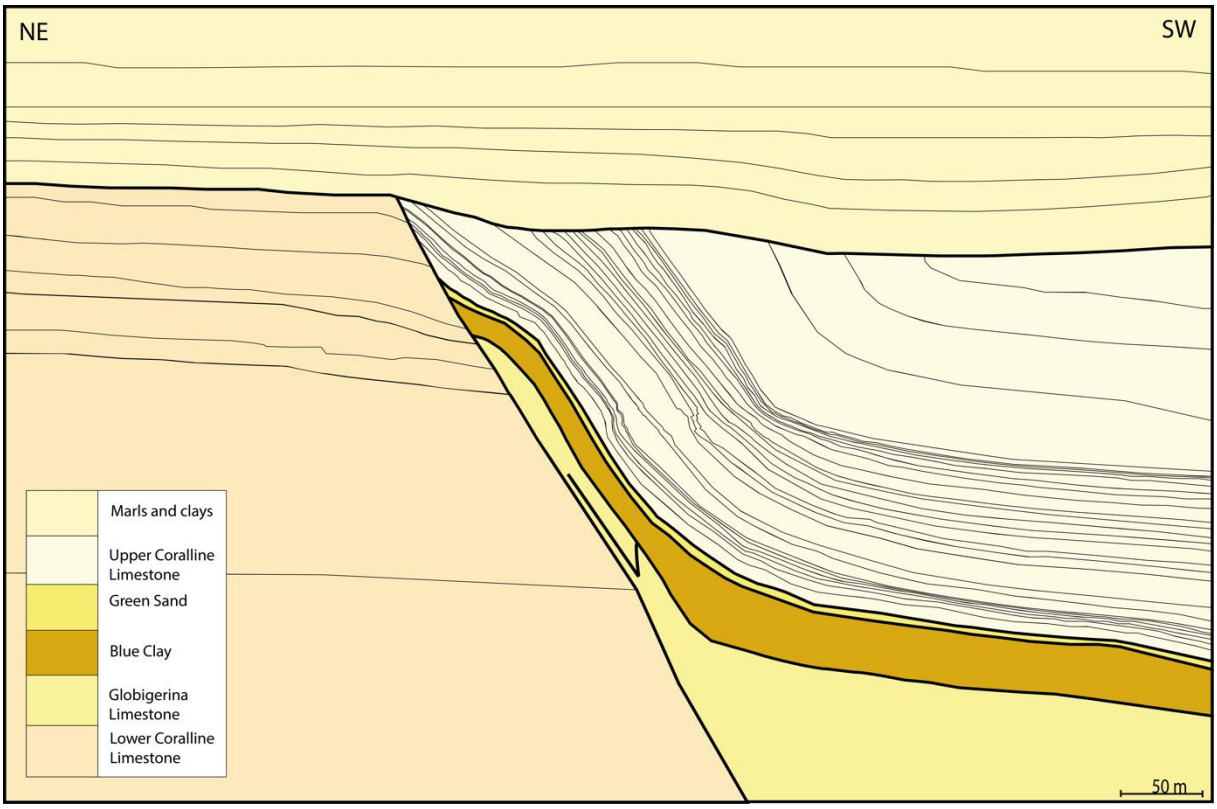

Fig 22: A 2D geological model representing the stratigraphic and fault zone architecture at Locality 2.

5.1.5. Locality 3: In-Neffiet

Locality 3 lies in a small sea inlet about 120 m east of Locality 2 and is the easternmost locality along the Maglaqh Fault studied in this thesis (Fig. 13). The hangingwall section studied is a ca. 140 m long cliff section and ca. 14 m at its highest point. This section is oriented N-S and has no exposure of the fault surface (Fig. 23a). The interpretation of the Maghlaq Fault was based on the lithological boundary between the LCL and GL. The location of the interpreted fault trace is indicated by the stippled line in Fig. 23. Supporting this interpretation, a fault surface with the same NW-SE orientation crops out 30 m to the SW from the fault trace at Locality 3 (Fig. 13). From north to south, there is a gradually increasing dip from ca. 60º to near vertical beds (Fig. 24). However, in relation to the main fault, an antithetic fault interrupts the gradually increasing dip, and the beds at the far south are deformed to an open, recumbent fold resulting in a southward dipping topography. A cave is situated underneath the antithetic fault, which implies that the area is less resistant to erosion. Locality 3 shares its structural

setting with Locality 2 (Fig. 13). Locality 3 was chosen as it was approachable for a more thorough study of the lithology. The log in subchapter 5.1.2 gives a description of the lithology on site (Fig. 16).

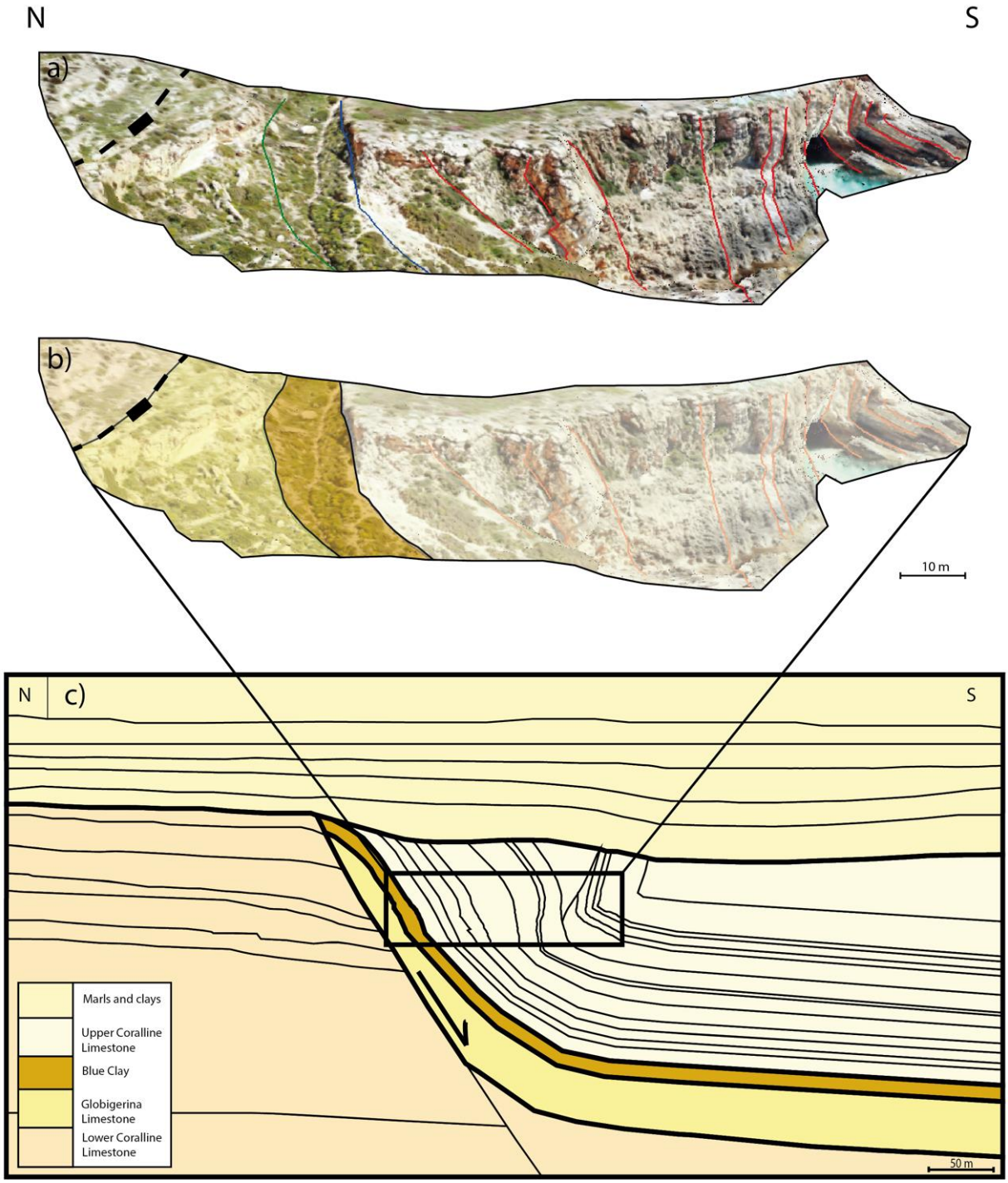

Fig 23: a) A 3D virtual outcrop model was made of the hangingwall cliff section at Locality 3. The interpreted lines illustrate hangingwall geometries and lithological interfaces (blue: GL-BC interface, green: BC-UCL interface, red: UCL bed geometries), whereas the stippled line marks the trace of the Maghlaq Fault. b) A simple illustration of the lithological distribution within the fault zone including the fault trace. c) A 2D geological model of the stratigraphic and fault zone architecture at Locality 3.

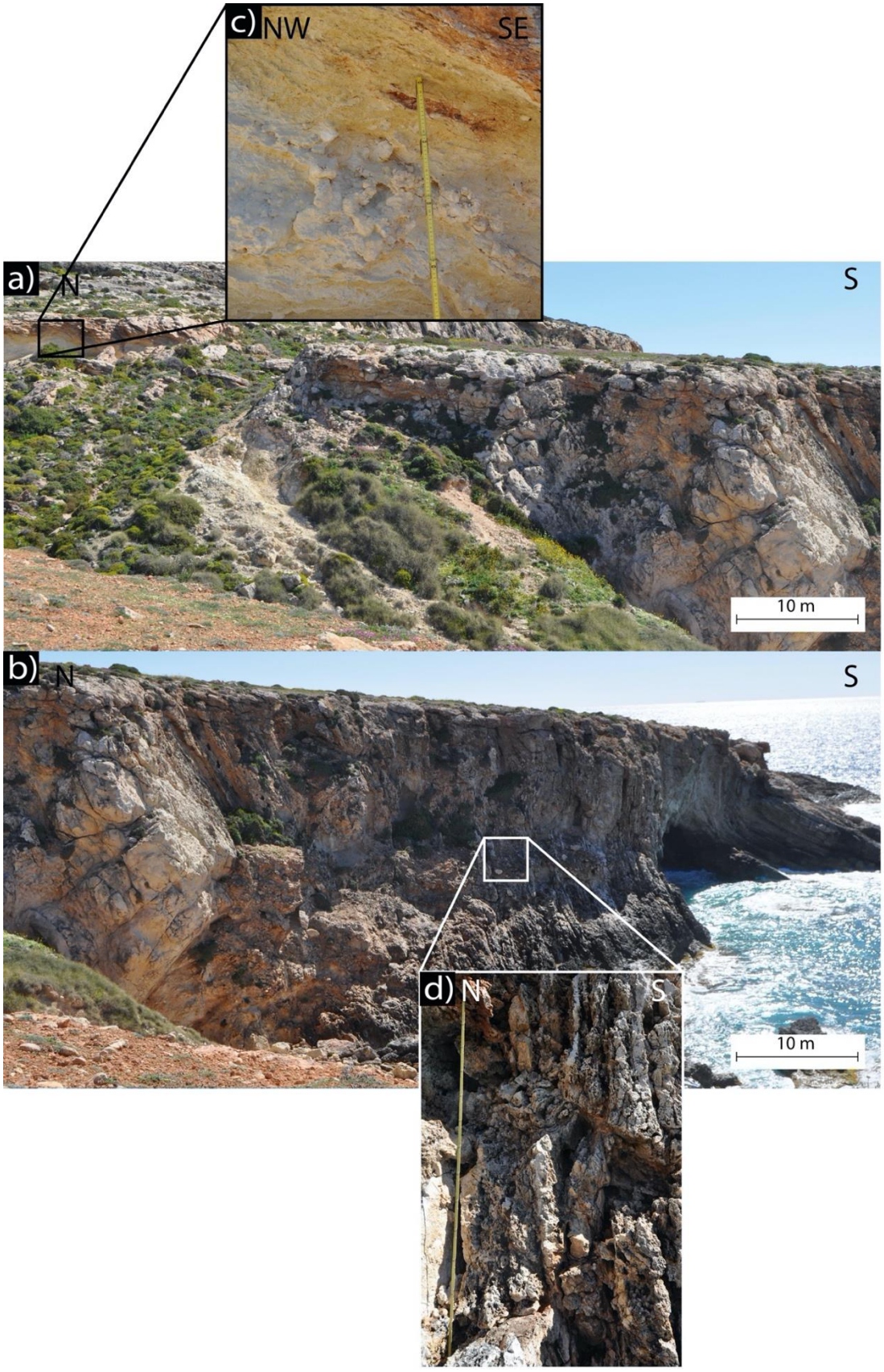

Fig 24: Photos of the hangingwall geometry and lithology at Locality 3 (In-Neffiet). a) A more detailed view of the north part of the section in Fig. 23a. b) A more detailed view of the south part of the section in Fig. 23a. c) GL was found close to the Maghlaq Fault (60 cm long ruler for scale). d) Vertical oriented and fractured UCL hangingwall layers (2 m long ruler for scale).

The generated 2D geological model from Locality 3 is oriented N-S (Fig. 23). It was modelled with a high degree of details, especially within UCL, because of the logged section at this locality. However, only five different stratigraphic units were used in the modelling, i.e., LCL, GL, BC, UCL, and marls and clays (Fig. 23). The dragged hangingwall strata is folded like a syncline with the dip increasing to near vertical towards the Maghlaq Fault, while a flattening of the layers occurs southward in the geological model. The Maghlaq Fault was modelled with a mean dip of ca. 59º. The fault juxtaposes the horizontal LCL footwall layers with the GL and BC, which is dragged along the fault surface, thus generating a discontinuity in the model. A change in orientation of the LCL layers occurs south of an antithetic fault intersecting the UCL in the hangingwall.

The designed 2D geological models contain different features and some variation in lithology and stratigraphic thicknesses. Locality 1 has a shallow dip of the hangingwall strata and includes minor antithetic faults (Fig. 19), whereas the base-case model from Locality 2 shows a steeply dipping and uninterrupted hangingwall strata (Fig. 22). The same steeply dipping hangingwall strata is interrupted at Locality 3 by an antithetic fault (Fig. 23). Modelling geological base cases from different localities, which contains different geological features, broadens the sensitivity testing of the Maghlaq Fault Zone in the 2D synthetic seismic images. In addition to the base-case models just described, changing the base cases to include different conceptual fault geometries and geological structures further broaden the investigation and sensitivity testing of the seismic images. Ten scenarios with different level of geological complexities were modelled for each of the three localities, with the aim to investigate differences in their seismic signatures (Fig. 11). The structures and geometries implemented in the geological models to enhance their complexity were chosen because they are typical elements encountered in fault zones (Fig. 5). For instance, fault lenses can be observed in multiple outcrops along the Maglaqh Fault, e.g., localities 1 (Fig. 17c) and 2 (Fig. 20b). There are lenses derived from the GL, both brecciated and intact, and lenses that contain relatively intact LCL. Lens thicknesses are within the interval of expected thickness from other studies (Childs et al., 2009, and references therein). Furthermore, the alteration of the fault geometry to a segmented fault and multiple overlapping segments was based on the actual fault geometry of the Maghlaq Fault mapped and interpreted by Bonson et al. (2007) (Fig. 13). However, fault geometries like that are commonplace in all types of rocks hosting faults (e.g., Aarland and Skjerven, 1998; Childs et al., 2009). For instance, an overlapping segmented fault geometry links up and becomes connected when the fault segments grow and is critical in the

development of a through-going fault (Childs et al., 2017). Investigating the seismic signatures of segmented faults and overlapping segments can help seismic interpreters to map and understand faults and associated deformation in seismic images. All the generated 2D geological models with conceptual fault geometry and structures can be found in Appendix I.

5.2 Seismic modelling of 2D models

The workflow described in Chapter 4 was applied to the various geological models. The seismic modelling was especially useful to illustrate seismic signatures of the geological features within a fault zone as a function of different dominant frequencies. In the following subchapters, the seismic modelling results are presented. A total of 90 synthetic seismic images were generated but not all of them are addressed in this thesis (Fig. 12). First, the base cases are addressed with the results from modelling with different dominant frequencies. Then, examples of seismic images of each of the different geological complexities are presented.

5.2.1 Changing the dominant frequency in the base cases

First, seismic modelling of the three base cases was done. Each case was modelled using dominant frequencies of 20, 40, and 60 Hz, which resulted in a total of nine base-case models. The purpose of the modelling was to investigate how the base cases are imaged when using the chosen modelling properties (Table 2). From the average velocity (Vp), the tuning thicknesses (λ/4) were estimated to be ca. 60, 40, and 20 m, from the lowest to the highest dominant frequency, respectively. Using a 45º as the steepest illuminated dip gives in practice a lateral resolution of λ/2, which is twice as large as the vertical resolution. Changing the dominant frequency changes the seismic response significantly, especially in terms of resolution. A description of each base case at the three localities will now be provided. For each seismic image, the corresponding PSF is displayed to illustrate resolution and illumination.

Table 2: Input properties used for seismic modelling.

Locality:	Average Vp (km/s)	Incident angle (º)	Illumination (º)	Ricker wavelet (Hz)
Locality 1	4.7	0	45	20, 40, 60
Locality 2	5.1	0	45	20, 40, 60
Locality 3	4.8	0	45	20, 40, 60

Locality 1

The termination of footwall reflections and clearly imaged folded hangingwall reflections along the fault make it possible to distinguish the Maghlaq Fault in the three seismic images of Locality 1 (Fig. 25). The BC seismic response shows a negative reflection (blue) at the top and a positive reflection (red-yellow) at the base. Regardless of the frequency, BC reflections dragged along the fault surface show strong seismic amplitudes when illuminated. This behavior is related to high contrasts in acoustic impedance across the layer interfaces. Fig. 25b displays the 20 Hz base case at Locality 1. The GL-BC interface is resolved as a high-amplitude positive reflection, whereas the BC and damaged rock layers are merged to a single high-amplitude, negative reflection because of limitations in resolution. Indeed, the top damaged rock boundary has a negative reflector in the reflectivity model (Fig. 25a) but appears as a positive reflection on the seismic image because its seismic signal is weaker than the BC side lobe (Fig. 25b zoomed area). In addition, destructive interference results in low amplitude at the top damaged rock boundary. The layers have steps in the reflections where they are too steep to be illuminated (Fig. 25b). A lower dip causes the UCL to be illuminated but the latter is not characterized by high amplitudes because of the low internal lithological variability (low reflectivity). The apparent dip of a folded hangingwall reflection, measured from one point to another in the seismic image, is ca. 43º compared to ca. 48º in the reflectivity model (Fig. 25a). In the 40 Hz case in Fig. 25c, more details are visible. An increased amount of visible seismic imaging artefacts are present extending along the fault surface, i.e., 45º-steep reflection-like signals resulting from the cross-pattern of the PSF because of its limited illumination (Lecomte et al., 2015). Note that these effects are also part of the 20 Hz image, but the lack of resolution in that case prevent their identification. Modelling at 40 Hz shows the damaged rock layer being resolved and with several reflection discontinuities in the folded hangingwall layers. The antithetic fault situated in the UCL is represented in the 40 Hz image by such a discontinuity. The apparent dip of the same hangingwall reflection measured in the 20 Hz image is ca. 46º in the 40 Hz case. Modelling at 60 Hz generates a seismic image with even higher level of detail, which leads to better detectability of the discontinuity indicating the presence of the small antithetic fault in the UCL (Fig. 25d). Additionally, reflection discontinuities visible in the steeply dipping hangingwall layers, caused by the 45º illumination effect, are more evident. This makes it more challenging to trace the reflections dragged along the fault in the seismic image without consulting the reflectivity model (Fig. 25a). The apparent dip of the hangingwall reflection in the image is also lower than in the reflectivity model. However, the apparent dip

of the reflection increases with increasing dominant frequency so that the reflection dips at 47º in the 60 Hz base case, which is close to the true dip of 48º.

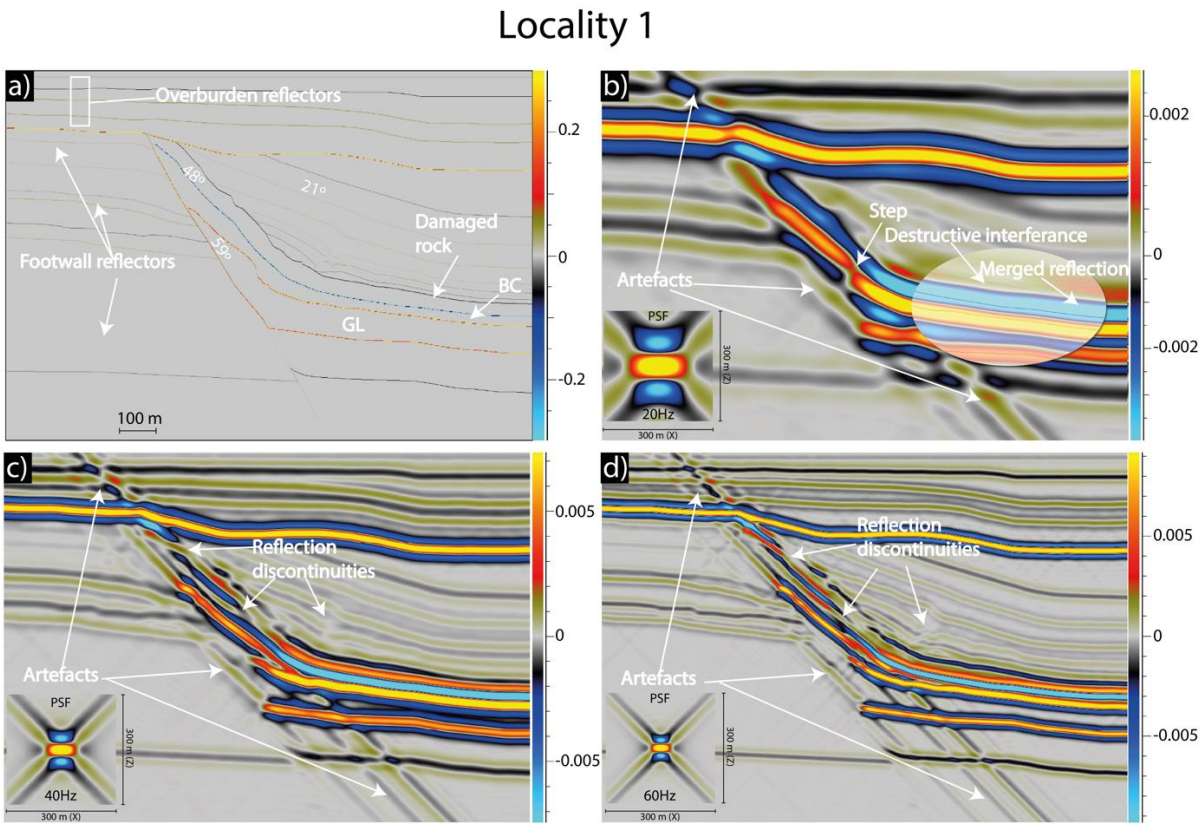

Fig 25: Base case reflectivity model and seismic images of Locality 1. a) Reflectivity model. b-d) Seismic images modelled with different dominant frequencies of 20, 40, and 60 Hz, respectively. The corresponding PSFs on each seismic image illustrate the resolution and 45º illumination effect.

Locality 2

In all the seismic images of Locality 2, the Maghlaq Fault is indicated by the termination of footwall reflections and bending of the hangingwall reflections (Fig. 26). High contrasts in acoustic impedance across the layer interfaces in the hangingwall causes the folded BC to show strong seismic amplitudes when illuminated. Modelling with a 20 Hz dominant frequency gives a low-resolution case where the expected tuning thickness is ca. 60 m and small details are hard to distinguish (Fig. 26b). In Fig. 26b, both a merged reflection and a dual reflection are present in the BC layer. The merged reflection is because the tuning thickness is too large. The side lobe of the upper BC reflection starts to interfere constructively with the main lobe of the base BC reflection, which leads to a high-amplitude single reflection. While, the dual reflection is the appearance of two negative reflections caused by increased thickness of the BC layer. This causes the side lobe of the upper BC boundary to be resolved (Fig. 26b). However, the BC layer

is still not completely resolved. Strong amplitudes are seen when reflections are flattening in the hangingwall, whereas lowered amplitudes are seen when layers are inclined. Illumination issues caused a dim area in the hangingwall, which is indicated by the white circle. The 5 m thick GS layer is not resolved in the 20 Hz image (Fig. 26b). More details can be distinguished in the 40 Hz image (Fig. 26c), where the tuning thickness has decreased to ca. 40 m. Inclined reflections parallel to the fault surface show some discontinuity and low amplitudes, but more sub-horizontal beds are resolved. Whereas, for the 60 Hz seismic image, the tuning thickness is ca. 30 m and the reflector spacing increases to near real layer thickness (Fig. 26d). Overall, the 60 Hz image (Fig. 26d) has a greater degree of detail compared to the 20 Hz (Fig. 26b) and 40 Hz (Fig. 26c) ones, as expected. However, the GS layer is still not resolved, and the top GS reflection continues to merge with the top BC reflection generating a single high-amplitude, negative reflection. The white circle has been kept constant to illustrate that the area characterized by low-amplitude reflections from the illumination effect has increased in the 60 Hz case and is not restricted to the white circle (Fig. 26d). Measuring the apparent dips of the hangingwall reflection in the 20, 40, and 60 Hz seismic images (Fig. 26b, c, and d) gives dips of ca. 40º, 42º, and 43º, respectively. This is lower than the ca. 52º dip in the reflectivity model (Fig. 26a).

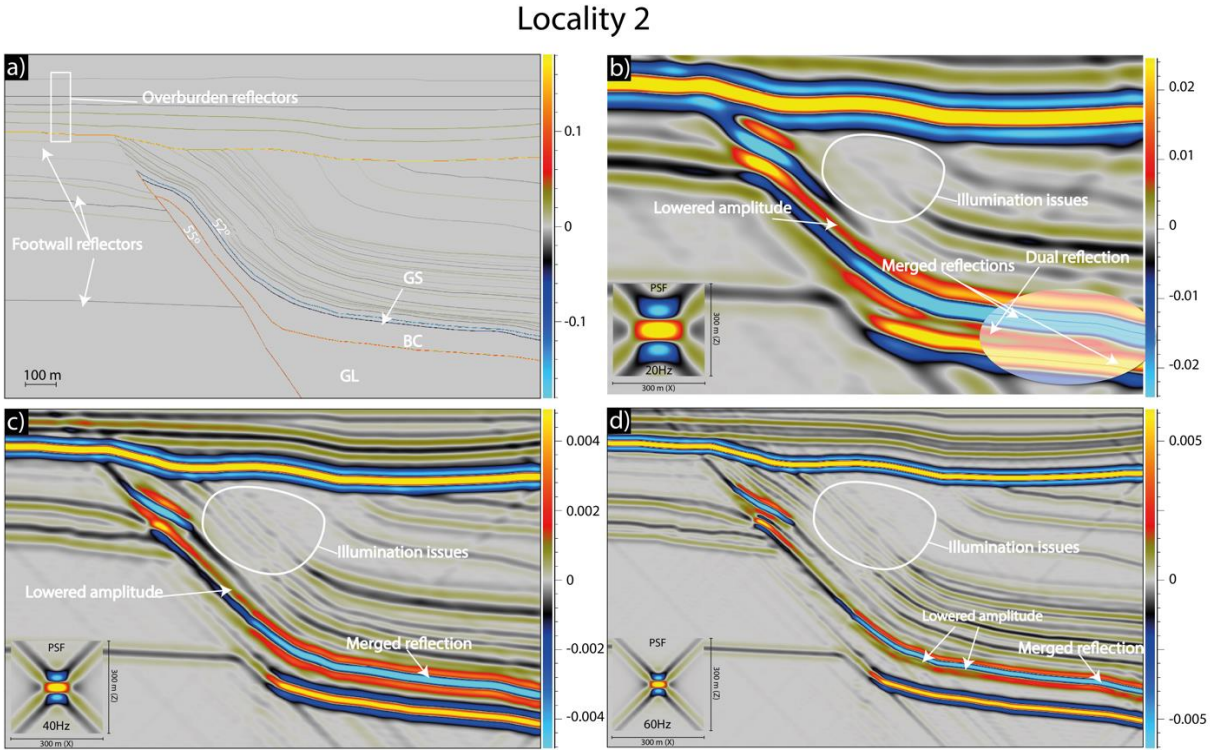

Fig 26: Base case reflectivity model and seismic images of Locality 2. a) Reflectivity model. b-d) Seismic images modelled with different dominant frequencies of 20, 40, and 60 Hz, respectively. The corresponding PSFs on each seismic image illustrate the resolution and 45º illumination effect.

Locality 3

In the seismic images of Locality 3, the Maghlaq Fault is indicated by the termination of footwall reflections and bending of the hangingwall reflections (Fig. 27). The 20 Hz image (Fig. 27b) shows high-amplitude reflections at the LCL-GL interface and GL-BC interface. The top damaged rock reflection is not resolved but is instead merged with the top BC reflection, generating a negative reflection of high amplitude. A step in the base overburden reflection is visible where the folded layers intersect the overburden layers. The small antithetic fault or the change in orientation of the hangingwall layers described in the geological model for Locality 3 are not seen because of the 45º limited-illumination effect on steeply dipping features. The fault and the change in orientation are seen in the reflectivity model (Fig. 27a). The white circle indicating the dim area caused by limitation in illumination is kept constant to show the change in extent of the dim area with increasing dominant frequency in the images. In the 40 Hz case the damaged rock layer is still not completely resolved but is represented by a thin negative reflection (Fig. 27c). A side lobe from the top BC reflection interacts with the base BC reflection, which results in constructive interference and a high amplitude positive reflection. The inclined hangingwall layers along the fault show an increased reflection discontinuity and a decreased amplitude resulting from the area of the actual outcrop with all its irregularities, which was mapped in detail. The visible artefacts are generated from the PSF cross-pattern originating from diffraction points as well as from the interference of surrounding, illuminated structures. Fig. 27b, c and d show examples where diffractions from hangingwall reflections along the fault interfere with the overburden planar reflections. The 60 Hz, shows a higher level of detail with more visible artefacts, as discussed earlier, and more reflection discontinuities in the steeply dipping layers of GL, BC, damaged rock, and UCL (Fig. 27d). The damaged rock layer is better resolved at 60 Hz and instead of a merged reflection in the BC layer, a dual reflection is now visible. The apparent dips of the hangingwall reflection are ca. 41º at 20 Hz, ca.43º at 40 Hz, and ca.44º at 60 Hz. Compared with the reflectivity model in Fig. 27a, with a true dip of ca. 53º, the apparent dip in the seismic images is significantly lower.

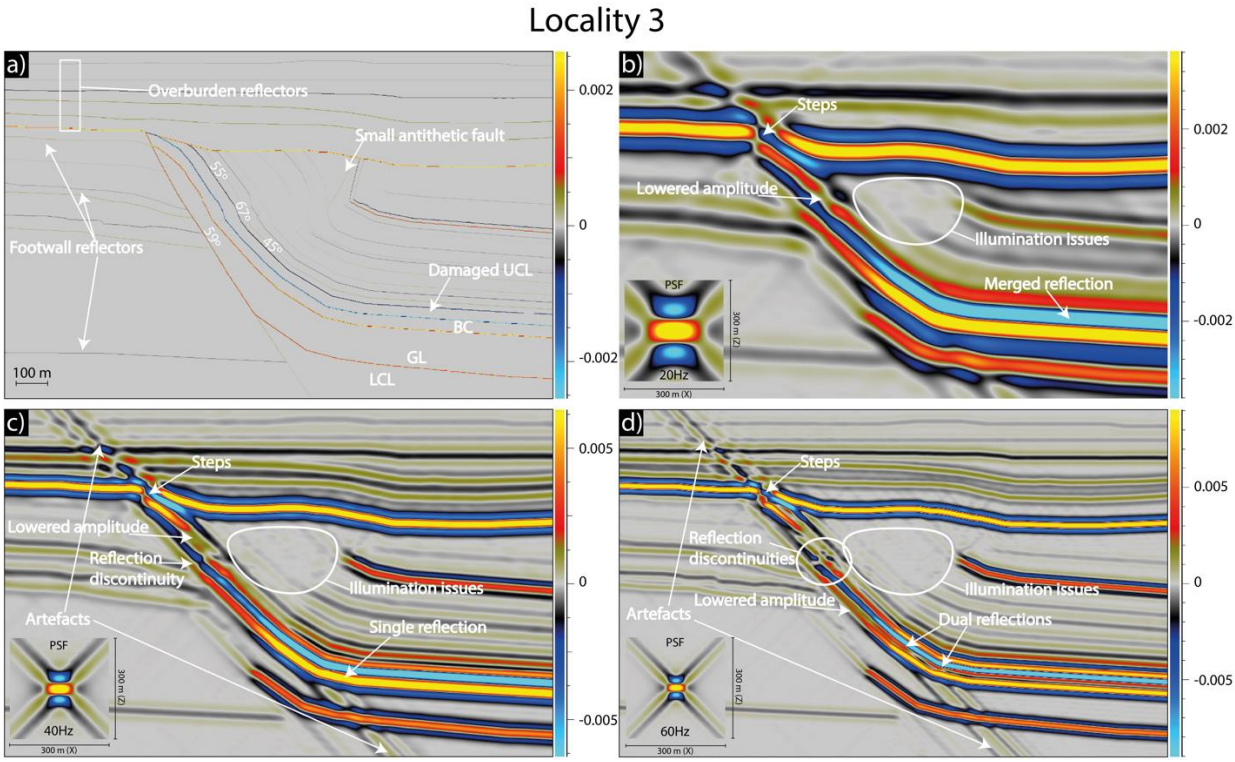

Fig 27: Base case reflectivity model and seismic images of Locality 3. a) Reflectivity model. b-d) Seismic images modelled with different dominant frequencies of 20, 40, and 60 Hz, respectively. The corresponding PSFs on each seismic image illustrate the resolution and 45º illumination effect.

5.2.2 Changing geological structures and geometries

As mentioned in the descriptions of the geological models in 5.1, the geological base-case models were altered in order to look at how variations in the fault zone architecture would affect the seismic image. Results from various geological structures and geometries such as i) segmented fault, ii) overlapping segments, iii) lenses, iv) fault rock will be described in the following sections.

Segmented fault

A segmentation in the fault was added to the base-case model of Locality 2 and modelled with the dominant frequency of 40 Hz (Fig. 28). In the reflectivity model, the GS is a thin layer represented by a negative reflector both at the top and the base (Fig. 28a). The GS layer is not resolved in the seismic image but merged with the BC reflection, which creates a high amplitude reflection within the segmented fault geometry. The geometry of the geological feature is visible and exhibits a step in the reflections of the GL-BC/GS interface and the BC/GS-UCL interface. Both reflectors are illuminated in the fault segment due to a dip less than 45° and thus appear on the seismic image. Where the corresponding reflections in the fault segment intersect

the base reflections in the overburden, a tuning effect results in destructive interference in the base of the overburden reflection (Fig. 29)

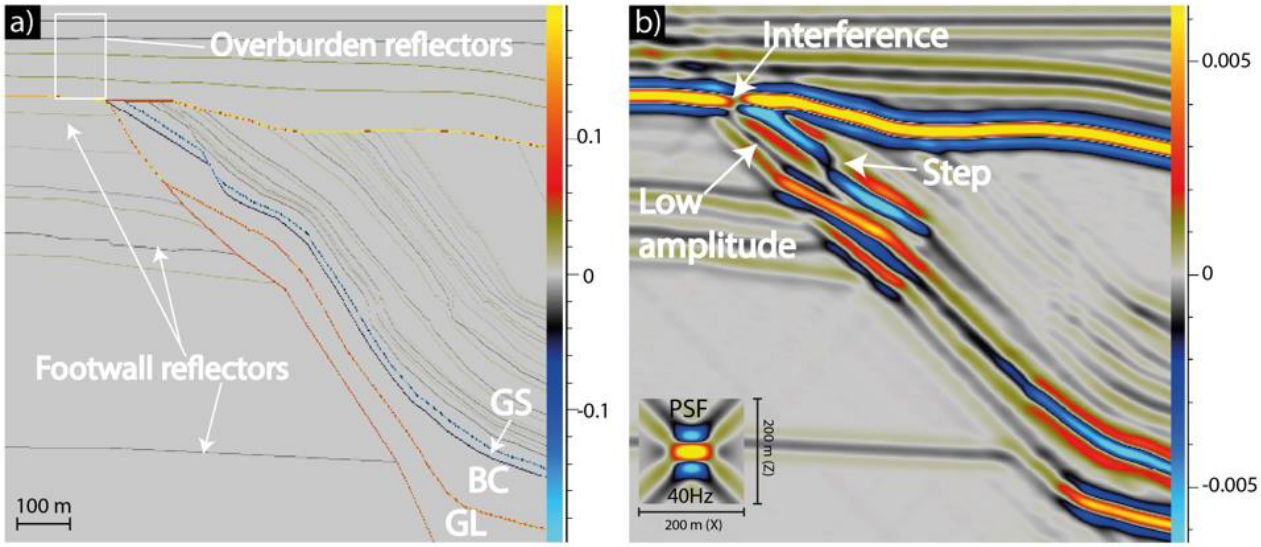

Fig 28: a) Reflectivity model generated from the 2D geological model of Locality 2 altered with a segmented fault geometry. b) Synthetic seismic image of the segmented fault modelled with the dominant frequency of 40 Hz.

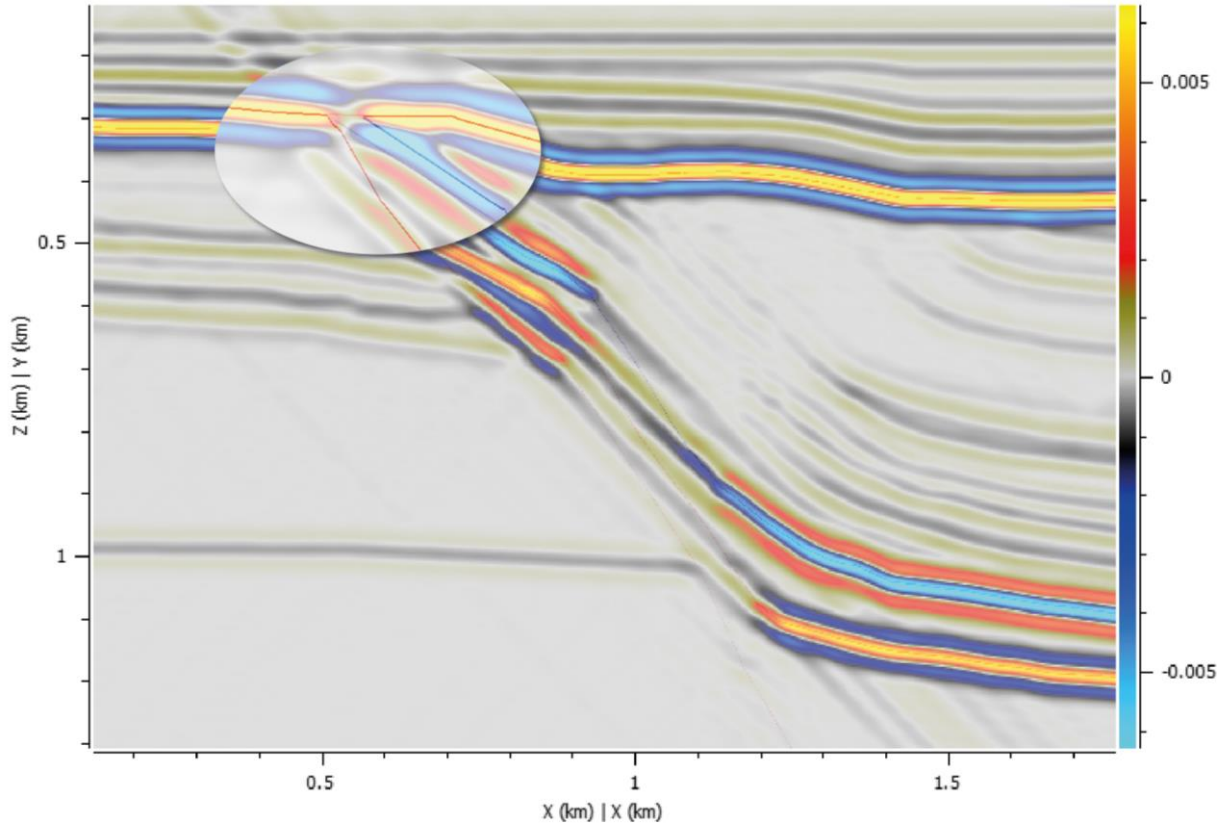

Fig 29: The zoomed area of the segmented fault seismic image shows where a significant decrease in the amplitude of the base overburden reflection occurs.

Overlapping segments

Synthetic seismic images were generated to study the Maghlaq Fault with an increased level of complexity in the fault geometry. The base-case model from Locality 3 has been altered to contain two overlapping segments in addition to the main slip surface, and further modelled with a 40 Hz dominant frequency (Fig. 30). The synthetic seismic image shows a similar step-like geometry of the down-faulted segments seen in the input reflectivity model. The reflection from the GL-BC interface are seen in the steps, whereas the damaged host rock layer is not resolved (Fig. 30b). Instead, a merged high-amplitude negative reflection is present. Additionally, a wavy interference pattern is detected within the GL layer. Interference between the base overburden reflection and the reflection within the segments occurs (Fig. 31 zoomed area 1). The interference is a result of internal variations in the geological model, closely spaced reflectors, and limitations in resolution. Another interesting observation in Fig. 31 is the appearance of the steeply dipping hangingwall reflections. The negative reflector of the BC-damaged rock interface in the reflectivity model appears with a positive reflection in the seismic image, whereas the opposite is the case for the reflection representing the GL-BC interface (Fig. 31 zoomed area 2). From the zoomed area 2 in Fig. 31, the reflectors in the reflectivity model show the true dip to be steeper than how the reflections appear in the synthetic seismic image.

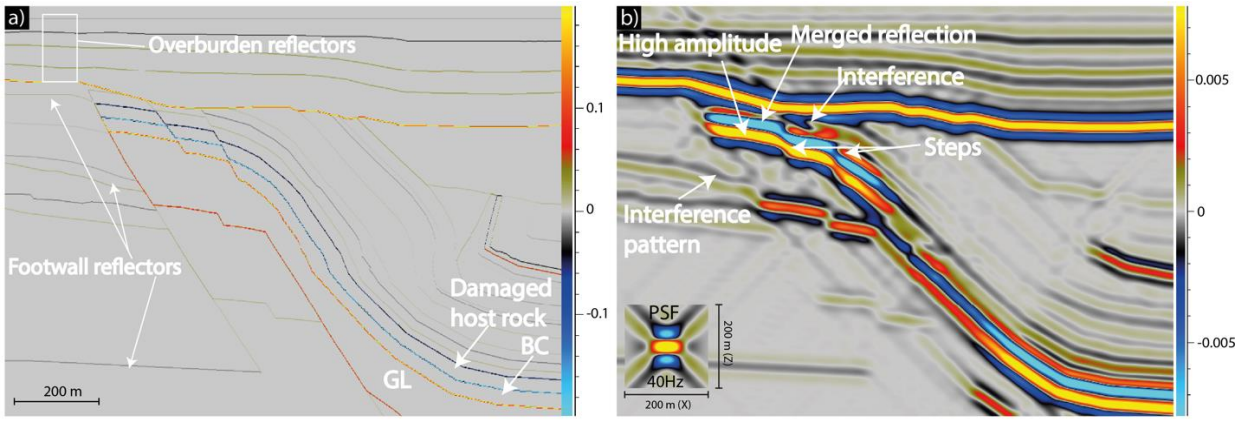

Fig 30: a) Reflectivity model generated from the 2D geological model of Locality 3 altered with multiple overlapping fault segments. b) Synthetic seismic image of the segments modelled with a dominant frequency of 40 Hz.

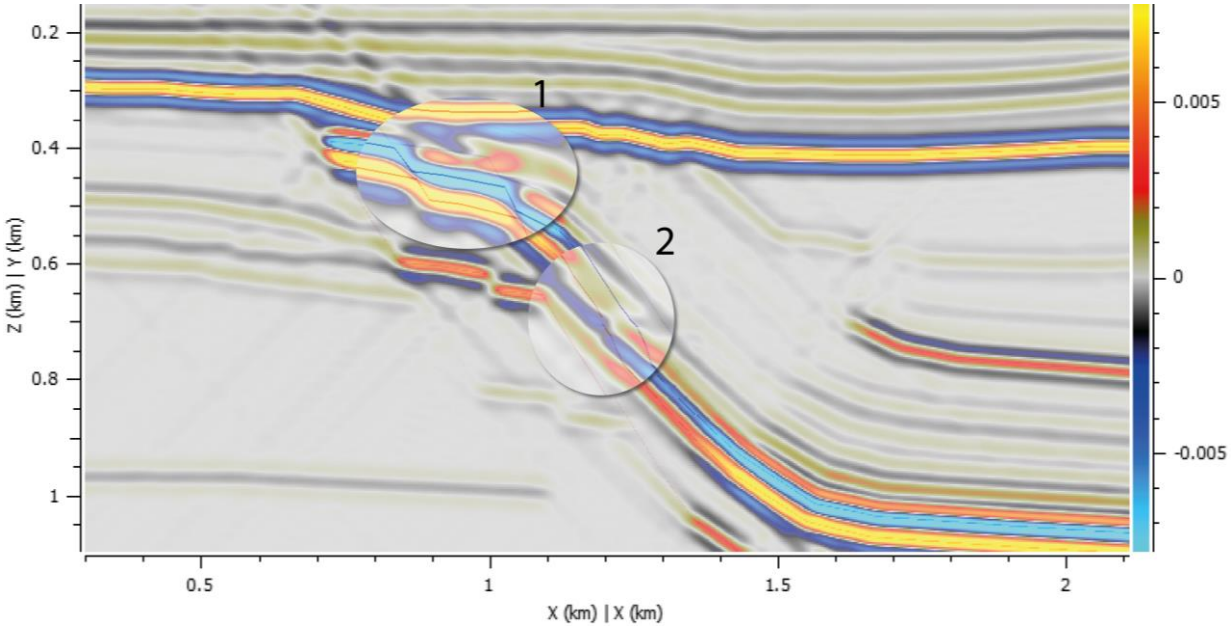

Fig 31: The zoomed area 1 in the segments shows interference between the sub-horizontal damaged rock reflection and the base overburden reflection. The zoomed area 2 shows the steeply dipping reflections, which appear with a different polarity in the seismic image compared to the reflectivity model.

Lens thickness variations and properties

The geological model from Locality 1 was modified slightly to include a lens along the Maghlaq Fault surface. Fig. 32 and 33 show the synthetic seismic images that were generated from this modified geological model, using the dominant frequencies of 20, 40, and 60 Hz for three different lens thicknesses (65, 100, 130 m). The lens was given properties as explained in the following section.

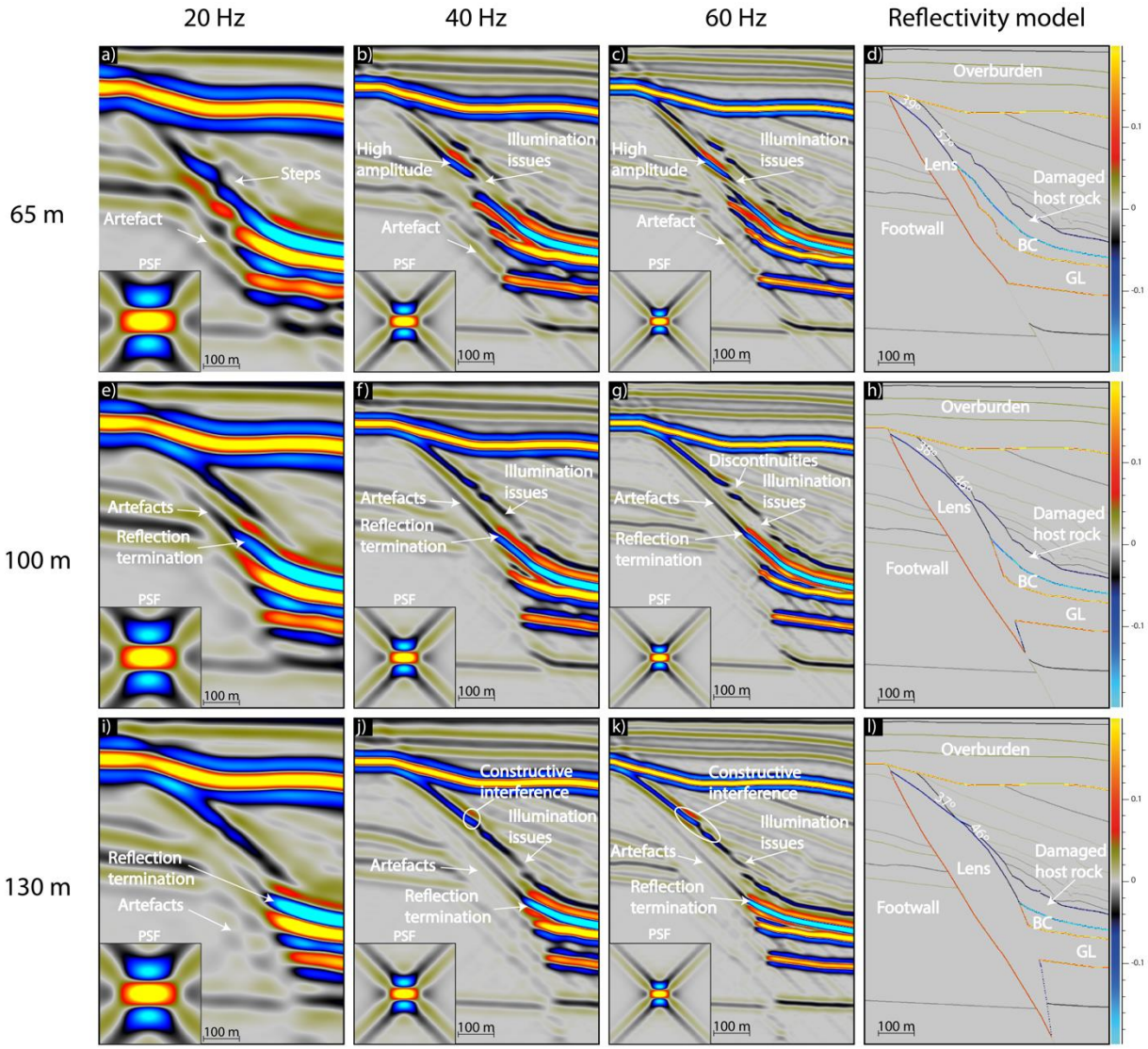

Fig 32: A set of synthetic seismic images, using three different dominant frequencies (20, 40, and 60 Hz) showing the seismic response from a GL lens (Vp=3.7 km/s) of three different thicknesses (65, 100, and 130 m). d), h), and l) are the input reflectivity models for the corresponding lens thickness.

The models were first run to study the synthetic seismic signature of a fault lens composed of brecciated GL (Vp=3.7 km/s). For the 65 m cases (Fig. 32a, b, and c), the overall lens shape and orientation is hard to identify in the seismic image because of illumination issues and complicated interference patterns (e.g., Fig. 32a and b), which result in less geometrical resembles to the input reflectivity model (Fig. 32d). At this lens thickness, the images are characterized by steps in reflections at 20 Hz (Fig. 32a) and reflection discontinuities along the lens path at the contact with hangingwall layers at 40 and 60 Hz (Fig. 32b and c). The steps and the high amplitudes pointed out in the Fig. 32a, b, and c, is where the reflection from the upper and lower boundary of the BC is a bit shallower and is cut by the GL lens. Seismic images of the 100 m thick lens lack the seismic artefact along the fault surface present in the 65 m case,

and a distinct transition between the lens and the footwall is not present (Fig. 32e, f, and g). In the seismic images of the largest lens thickness (130 m), the reflection bounding the upper part of the lens on the hangingwall side has a negative polarity. In Fig. 32j and k, the negative upper lens reflection constructively interferes with a folded hangingwall reflection resulting in a high-amplitude reflection. A large transparent zone within the lens is characterized by artefacts. In general, the 45º-limitation in illumination keeps a continuous reflection from surrounding the lens on all the seismic images in Fig. 32. However, termination of the hangingwall and footwall reflections does indicate vertical and lateral extent of the lens. From the input reflectivity model, one can see how the lens changes the wavelet polarity, from peak to trough, depending on which lithology it borders. Note that the lens lacks a reflector to the GL layer, which is because they have the same elastic properties (Fig. 32d, h, and l).

Another set of seismic images shows the same lens geometry, but different elastic properties (Fig. 33). Unlike the GL lens with a Vp of 3.7 km/s, the lens in the new models are assigned the elastic properties of a conceptual cemented LCL with Vp of 6.4 km/s (Table 1). In all the seismic images, no distinct transition occurs between the LCL lens and the footwall strata. In the reflectivity model, the reflector bounding the upper part of the lens has a positive polarity, which creates a destructive interference from the interface with the hangingwall layers. This is best illustrated in the models for the 100 m and 130 m lens thickness by low amplitude reflections (Fig. 33). The 20 Hz images are characterized by an overall wavy interference pattern because of a relatively large PSF. The lack of high-amplitude reflections makes it difficult to distinguish the lens geometry, hence the synthetic images do not geometrically resemble the input reflectivity model. The same images have illumination issues and internal lens artefacts are visible.

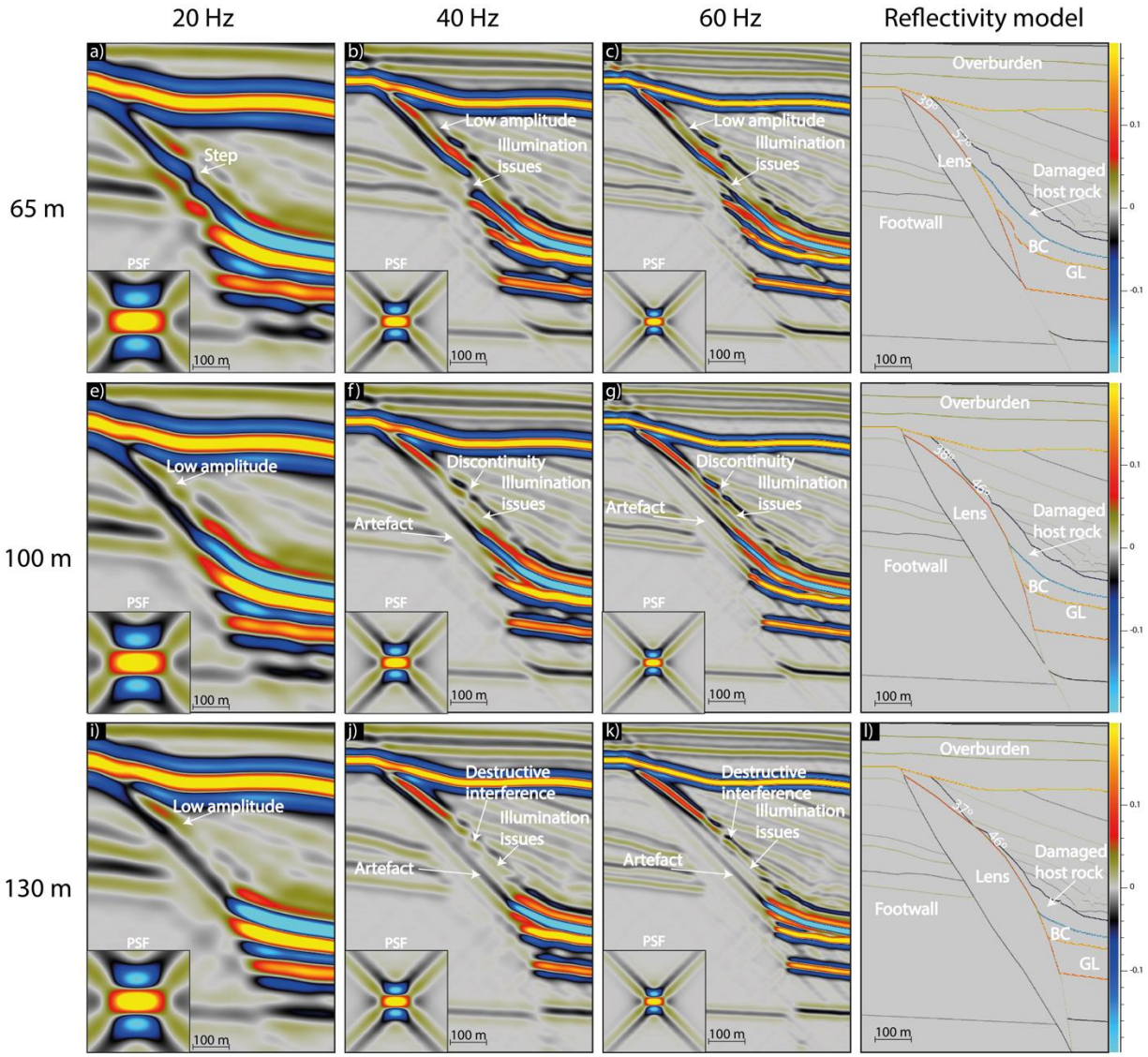

Fig 33: A set of synthetic seismic images, using three different dominant frequencies (20, 40, and 60 Hz) showing the seismic response from a cemented LCL lens (Vp=6.4 km/s) of three different thicknesses (65, 100, and 130 m). d), h), and l) are the input reflectivity models for the corresponding lens thickness.

The influence of a sub-seismic fault rock

The last seismic image shows the seismic response when including a 3-6 m thick, continuous and cemented LCL fault rock (Vp=6.4 km/s), in addition to a GL lens (65 m thick) in the geological model of Locality 1 (Fig. 34a). Adding another fault zone element increases the complexity of the geological model. The modelling was done at high resolution (60 Hz) with the aim to compare the resulting image with the 65 m thick GL lens image of the same frequency in order to detect differences and investigate the influence of a sub-seismic resolution fault rock. Modelling of the sub-seismic feature results in the fault rock to not be illuminated in the seismic image (Fig. 34b). Nevertheless, the LCL fault rock is detected by amplitude anomalies and a complex interference pattern in the footwall. In the input reflectivity model, the LCL fault rock-

GL lens interface is a positive reflection, whereas the LCL fault rock reflection bordering the footwall strata is a negative reflection (Fig. 34a).

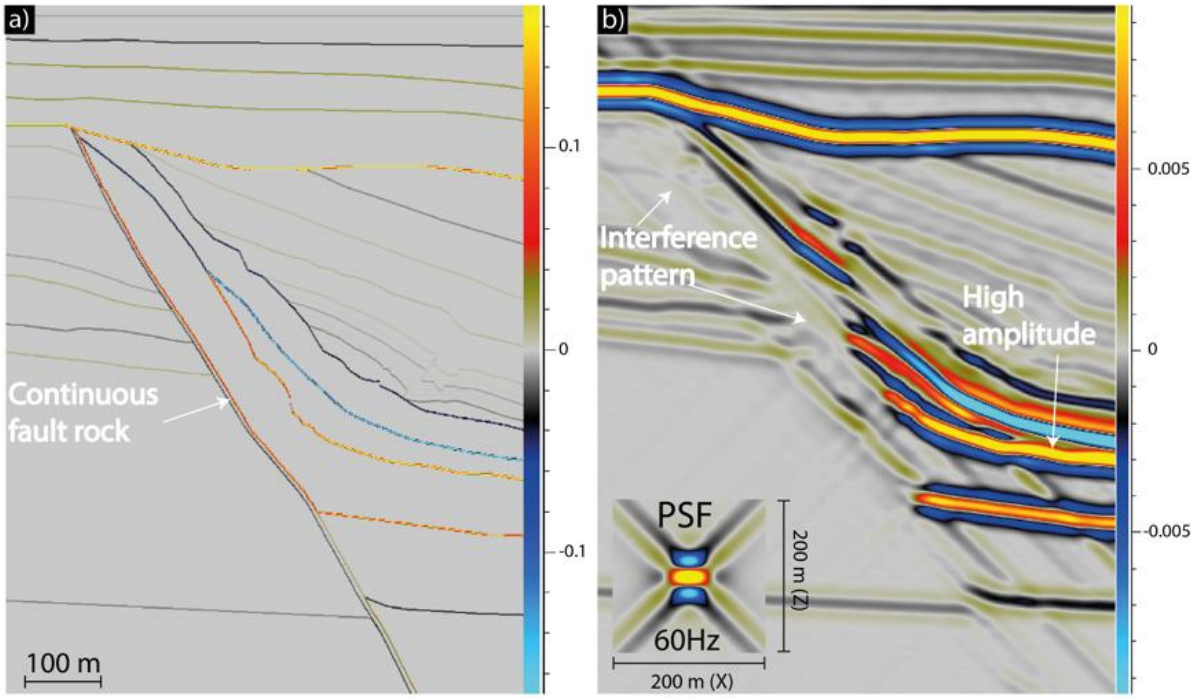

Fig 34: a) Reflectivity model generated from the 2D geological model of Locality 1 altered to contain a 3-6 m thick continuous fault rock (Vp=6.4 km/s) in addition to a 65 m thick GL lens (Vp=3.7 km/s). b) Synthetic seismic image of the fault rock modelled with the dominant frequency of 60 Hz.

6. DISCUSSION

In this chapter, the synthetic seismic images resulting from seismic modelling of outcrop data are discussed. First, challenges regarding the use of outcrop analogues and limitations in field data are addressed, followed by a discussion of the geological models and elastic properties along with related uncertainties. Next, the seismic images are discussed in terms of the variations in structure and geometry, as well as changes to the dominant frequencies and amplitude variations within the fault zone. The 2D seismic images are compared to isolate the seismic signatures of the different geological parameters. Typical issues related to the imaging of faults in seismic are discussed. Lastly, the implications and applications of the presented research are addressed.

6.1 Limitation in outcrop photogrammetry and field data

Drone photos and field data were used in the construction and interpretation of the virtual outcrop models. The use of outcropping surface analogues allows us to study the relationship between geology and the seismic response. However, several challenges are associated with the use of outcrop analogues. Poor exposure of lithologies can bias outcrop measurements, and heavily weathering of the outcrop does not provide a direct analogue between outcrop petrophysics and the subsurface. In addition, few outcrops have the appropriate scale to enable their use as direct analogues to subsurface reservoir systems (Howell et al., 2014). It is crucial to consider these challenges when extracting useful data from analogues and laying the base for seismic modelling. On the other hand, outcrop analogues provide information on all scales and give a better conceptual understanding of systems.

Photogrammetry obtained by a drone is a cost and time efficient method to build virtual outcrop models and gather geological information. Despite the high resolution of the drone camera, photo quality is highly dependent on weather conditions. Too much direct sun on the outcrop make the limestones reflect the light, which resulted in whitening of the rocks and a lack of visible details in the photos. Keeping the drone in the exact same distance and angle to the outcrop when gathering data is difficult because of 3D irregularities in the section. Furthermore, the geological models are based on outcrops of different size and varying exposure. Locality 2 has incoherent exposure from the fault surface throughout the damage zone (Fig. 21); whereas, at Locality 3, the fault surface was not visible at all (Fig. 23). This lack of exposure could lead to some mismatches of the geological features and less accurate interpretation. However,

disconnected parts in the outcrop at Locality 3 are few. The outcropping sections are fresh and show evident hangingwall geometries. The overall quality of the outcrops is sufficient to generate detailed geological models and corresponding seismic images.

6.2 Geological models and elastic properties

The units BC and GS create a low-velocity zone along the fault surface in the hangingwall which yield high acoustic impedance on the interface with the LCL, GL, and UCL (Table 1). GS is a thin bed, and its reflection merges with the upper BC reflection in the synthetic seismic images (e.g., Fig. 26). These reflections, together with the GL reflections, are prominent in the seismic images, and are helpful in studying the fault-related folding. Modelling of a stratigraphic succession with a large range in seismic properties (Vp: 1900-5900 m/s) causes complex interference patterns in the seismic images because of geometries that include vertically and horizontally dipping features (e.g., Fig. 30b). The results are similar to Rabbel et al. (2018), who studied the seismic signatures of igneous sill complexes in host rocks of evaporites, carbonates and organic rich shales with high variability in seismic properties (Vp: 3350-5950 m/s). Their results showed variations in the amplitude and interference patterns because of the elastic property variations in the host rock lithology, making it harder to define sill geometries. In spite of the geometries being sill complexes, their findings are similar to the complex interference and amplitude variations related to fault zone structures and geometries in the seismic images in this thesis.

6.2.1 Possible uncertainties related to the geological models and elastic properties

The 2D geological models were built on interpretations of the virtual outcrop models to create a simplified representation of the Maghlaq Fault Zone. In order to obtain applicable models, the folded hangingwall layers were extrapolated, using conceptual and simplified ideas, and then scaled to seismic. Although uncertainties should be associated with fault size scaling and extrapolation (Hardacre and Cowie, 2003; Færseth, 2006), the level of uncertainty connected to the geological models is largely because only a small part of the original succession was left onshore to examine. The outcrops are strongly eroded and have limited exposure, hence the extent of the drag zone related to the Maghlaq Fault is hard to define. The geological base-case models were also used in another MSc project, Andersen (2020). Their consensus was that because the models were created by two different persons, they were less consistent than if one person had created them. Furthermore, interpretations can be inaccurate and incorrectly

represent the hangingwall geometries and lithologies. Nevertheless, the main focus of the geological models is the area interpreted directly from the outcrops. This area is a direct representation of the fault zone geometries, with minimum extrapolation, hence a lower level of uncertainty.

All the synthetic seismic images and subsequent interpretations are dependent on the quality of the geological models and the input elastic properties (Vp, Vs, and density). No petrophysical properties were measured in the field, and no well-core data were available. Choosing reliable elastic properties in the seismic modelling was challenging. The choice of elastic properties is important because they have a strong influence on the resulting seismic images. As mentioned earlier, the elastic properties used in the modelling in this thesis are based on an empirical equation (Gardner's law) and simple relations (Vp/Vs) from literature, thus representing a simplification of the succession found in Malta. An uncertainty is connected to the equation and relations, especially since the Gardner relation is mainly valid for siliciclastic rocks. Anselmetti and Eberli (1993) suggested modifications for the equation to be valid for carbonates, whereas Miller (1992) found the calculated densities to be very consistent with the densities measured. Although limestones have been proven to have high variability in seismic properties (Vp of ca. 1.7-6.5 km/s) (Anselmetti and Eberli, 1993), the limestone succession in Malta is made of shallow-platform carbonates that typically have a high Vp.

6.3 Seismic modelling

6.3.1 Change of dominant frequencies

Seismic modelling was performed with constant incident angle and illumination, whereas the dominant frequency and geological scenarios of the fault zone were varied. All the dominant frequencies considered in this thesis allow for the imaging of the fault-related folding in the hangingwall, but the fault surface itself was not imaged due to illumination issues. The illumination issues are related to the inability to illuminate steep dipping (more than 45° in this thesis) and vertical seismic reflectors, which is highly influenced by the illumination pattern direction (Lecomte et al., 2016). The presence of the Maghlaq Fault is a discontinuity represented by the termination of footwall reflections and the fault-related strain (mainly folding) in the seismic images at all frequencies. Low-velocity layers (clay) found along the fault core in the hangingwall are characteristic for the fault zones. This finding is in agreement with those of Jeanne et al. (2012), who found that faults often have seismic signatures

corresponding to low-velocity bodies around the fault core. Such seismic signatures can be used in the detection of faults without a clear offset.

There are differences in the visualization regarding each of the respected dominant frequencies. In the synthetic seismic images, the level of detectable details increases with increasing dominant frequency. However, less hangingwall reflectors are illuminated in the seismic images of localities 2 and 3 (Fig. 26 and 27) because most of the layers are dipping more than 45°. A lower dip of the layers in the seismic images of Locality 1 (Fig. 25) results in illumination of the inclined hangingwall layers. In the 20 Hz seismic images details are not resolved because of the tuning effect and interference with other reflections. Additionally, the apparent dip of the fault surface is significantly lower in the 20 Hz seismic images compared to the input reflectivity model, as seen in Fig. 25, 26, and 27. This inconsistency reveals that interpretation of fault dip in real seismic data at 20 Hz is likely to be underestimated and crucial details may be overlooked when the vertical resolution is ca. 60 m. The vertical resolution significantly increases when modelling with higher frequencies (40 and 60 Hz). The bed thickness gets closer to the real thickness and creates better recognition of the structural geometries. At 40 Hz, which is the dominant frequency at shallow depths (ca. 1 km) (Eide et al., 2018), the vertical resolution is ca. 40 m. Most details are detected at 60 Hz where the vertical resolution is about 30 m. However, steeply dipping features are still not imaged because of the 45° limited-illumination effect. As seen in the reflectivity models of the base cases, many of the reflectors have dips greater than 45° and are not illuminated in the seismic images. Fig. 35 demonstrates the resulting seismic image of Locality 2 when modelled with perfect illumination at 40 Hz. In contrast to the seismic images modelled with a 45° limited-illumination, all the reflectors in the reflectivity model are illuminated. However, perfect illumination, is not possible to acquire in seismic data from the subsurface. Botter et al. (2014) showed that both frequency and illumination direction are important for imaging fault zones. By changing the illumination direction to avoid the middle pattern of the PSDM filter representing the illumination of the flat reflectors, they managed to highlight the internal structure of the fault zone (Fig 36). The direct illumination used in this thesis mainly highlights the horizontal reflections.

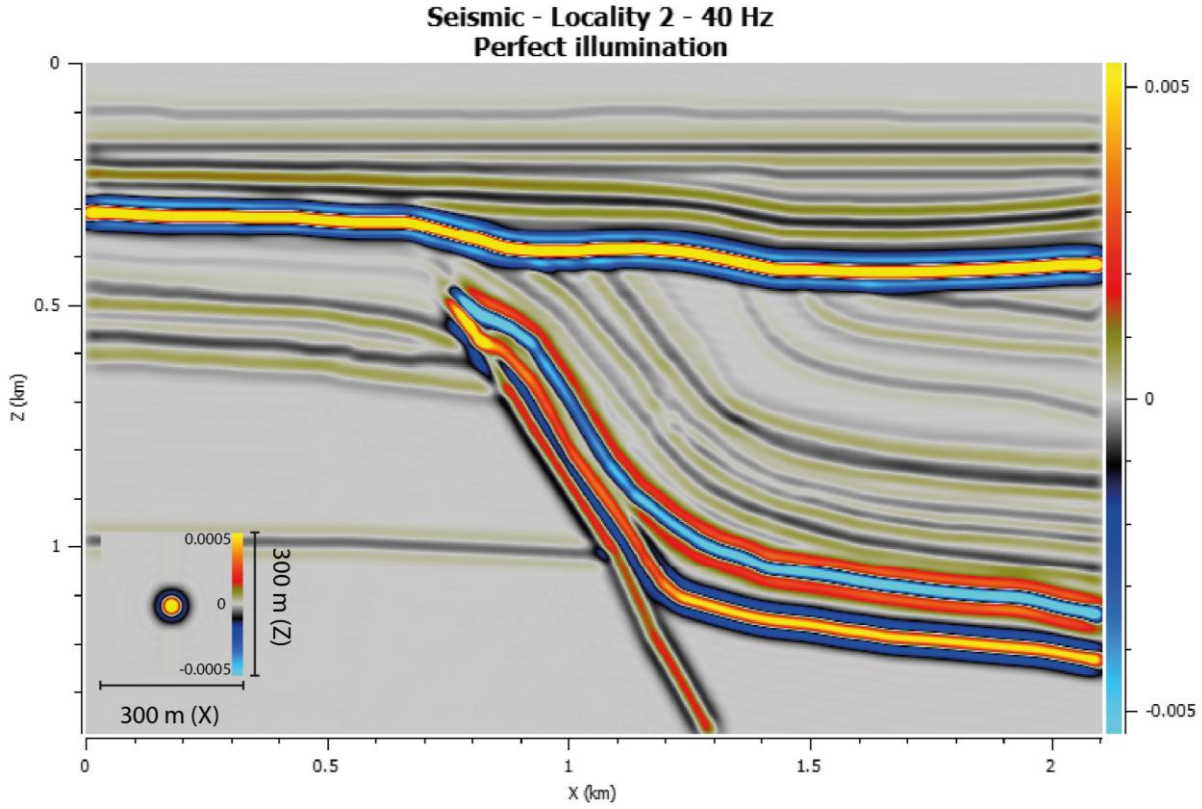

Fig 35: Seismic image of Locality 2 modelled with perfect illumination, illustrated by the PSF.

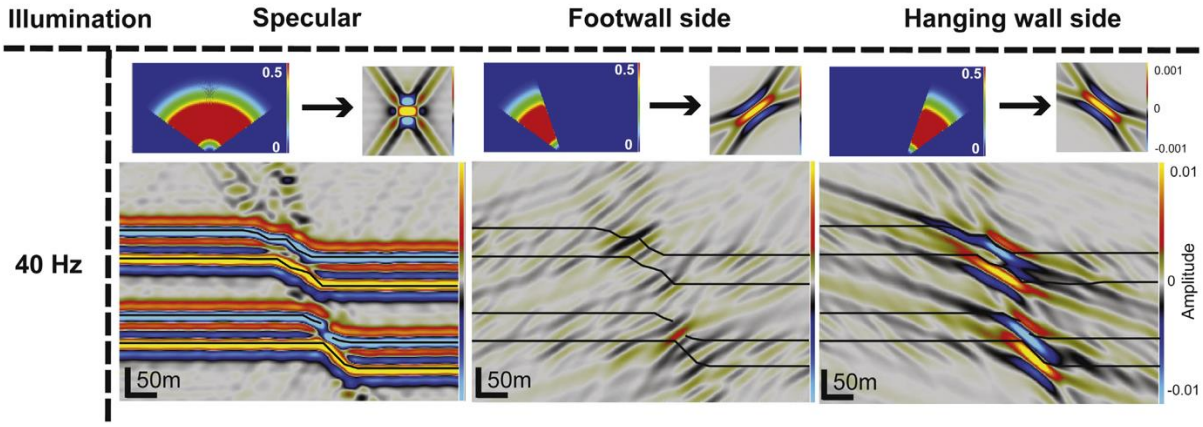

Fig 36: Seismic images of a normal fault modelled at 40 Hz with three different illumination directions. From left to right, the illumination direction in the seismic images are direct (specular), footwall side, and hangingwall side, respectively. The PSDM filter and corresponding PSF are shown at the top of each image. After Botter et al. (2014).

Another factor to consider is the wide range of seismic velocities in carbonates, which affects the resolution. In this case, the shallow platform carbonates have high seismic velocities, so the seismic resolution is lower compared to more typical exploration conditions where the vertical resolution is higher, e.g., ca. 40 m when Vp is 3.1 km/s at 20 Hz (Eide et al., 2018). It is indeed important for seismic interpreters to know the tuning thickness and the influence of thin layers when studying thin-bedded reservoirs. For instance, the thin GS layer is not resolved in Fig.

27d, instead, constructive interference occurs on the BC interface. In addition, a dominant frequency of 60 Hz is rare in conventional seismic acquisition because seismic energy is lost with depth. Nonetheless, the development of new methods, such as TopSeis and P-cable, means that high-frequency seismic may be acquired to image shallow reservoirs at high resolution. However, these new methods do not improve the seismic resolution issues related to deep reservoirs.

6.3.2 Amplitude variations in fault zones

Faults are known to have a complex 3D geometry and high variability in internal properties, yet fault interpretations are often hampered by a 2D approach to the interpretation and understanding of faults. Several fault zone models have been proposed (Chester and Logan, 1986; Caine et al., 1996; Childs et al., 2009), but these only give a simplified illustration and a broader 3D understanding of faults is needed. The seismic images generated in this thesis are all in 2D, while in real seismic sections, it is important to be aware of 3D complexity. An example of this complexity is discussed when addressing the lens interior later in this subchapter.

The simulated seismic images show amplitude variations across the fault zone (e.g., Fig. 26), which can be related to a variation in the elastic properties. A conspicuous difference between the two sets of images (Fig. 32 and 33) is the change occurring to the reflection bounding the upper part of the lens on the hangingwall side. Note that this change occurs because of the different elastic properties of the lens. The reflection appears as negative in the GL lens (Vp= 3.7 m/s) (Fig. 32), while the same reflection is positive for the cemented LCL lens (Vp= 6.4 m/s) (Fig. 33). The reflection has a higher amplitude and continuity when the lens is composed of GL rather than the cemented LCL (Fig. 37). The higher amplitude reflection is mainly because of constructive interference with a folded hangingwall layer, while the opposite (destructive interference) occurs when the lens is composed of cemented LCL. This inequality in seismic continuity between the two sets of seismic images is best shown in the seismic images of the 100 m and 130 m lens thickness (Fig. 32 and 33). A comparison between the 100 m lens models at 40 and 60 Hz is presented in Fig. 37. These differences imply that elastic properties impact the reflection characterization and further delineation of structural geometries with inclined and intersecting acoustic impedance boundaries. This is due to constructive and destructive interferences. The seismic differences associated with the lithological variation can be isolated, because the only difference between the two sets of lens models are the elastic

properties of the lens, whereas the lens and fault geometries are the same. This conclusion is of high relevance since acoustic properties of a rock may be altered as it undergoes structural deformation (Skurtveit et al., 2013). Botter et al. (2014) showed that modelling at 30-40 Hz gives a direct correlation between seismic amplitude variations and the input acoustic properties after faulting in a sandstone-shale sequence. Healy et al. (2015) showed a negative correlation between porosity and seismic velocity in faulted Oligocene-Miocene carbonates in Malta. In their study, the inner fault core has a lower porosity than the outer damage zone, correlating to increased and decreased seismic velocities, respectively. However, Matonti et al. (2012) investigated the distribution of Vp and the degree of cementation across a fault zone. They found a correlation between a strong porosity reduction and a Vp increase related to the cementation of pore volumes caused by chemical diagenesis. Cementation is not likely the cause of the variation in elastic properties in Malta because of a limited degree of diagenesis. This observation is supported by other field studies (Bonson et al., 2007; Michie et al., 2014; Cooke et al., 2018). Nevertheless, the cementation is a strong factor affecting the petrophysical properties of carbonate rocks and should be considered when studying carbonate rocks in the subsurface.

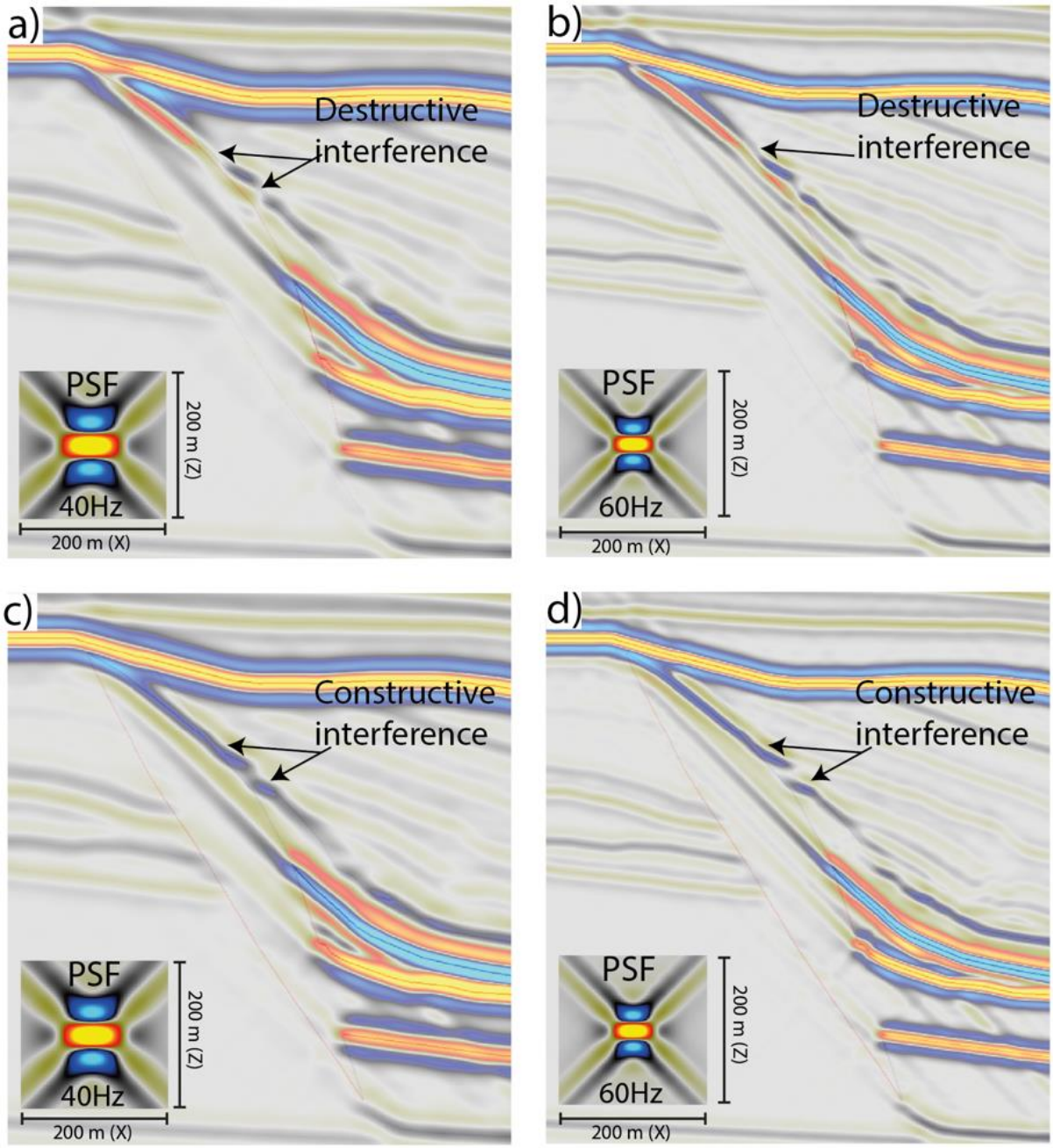

Fig 37: Superimposed plots between the reflectivity models and the 100 m thick lens modelled with different properties. a) 100 m thick cemented LCL lens at 40 Hz. b) 100 m thick cemented LCL lens at 60 Hz. c) 100 m thick GL lens at 40 Hz. d) 100 m thick GL lens at 60 Hz.

The discontinuity of the Maghlaq Fault increases in thickness when including a fault lens along the fault surface (Fig. 32 and 33). The lens interior is characterized by a transparent zone with seismic imaging artefacts, which can best be studied in the higher resolution seismic images of the 100 m and 130 m lens. In this thesis, all models are in 2D. In standard 3D seismic, the out-of-plane structures in the 3D geological model would also impact the studied vertical section because of the PSF footprint in all directions. In reality, the lens interior would be filled with imaging noise in addition to the cross-pattern generated by the PSF in 2D. Increasing the lens

size leads to an increased transparent zone within the fault zone. In addition, the increased thickness of the lens results in a lower dip of the reflector bounding the upper part of the lens in the hangingwall side. This lower dip leads to illumination that allows for a better delineation of the upper part of the lens. The reflector representing the footwall-lens interface is not illuminated, which make the transition diffuse. Similar illumination issues are identified for all the steep dipping features in the fault zone, such as the folded hangingwall layers and segments in Fig. 30. The enlarged area of the steeply dipping hangingwall layers in Fig. 31 shows the reflections in the seismic images with different polarity and with a lower dip than the reflectors in the reflectivity model. This deviation between the reflectors and reflections can only be revealed when comparing seismic images with the reflectivity model, which is of course not possible with real seismic data. Interpretation of steeply dipping layers must thus be executed with caution; recognizing structural geometries and preventing the mismatching of reflections can be challenging. Cunningham et al. (2019) showed that brightening in amplitude occurs when approaching the fault through a syncline and proved, e.g., that the variation in seismic amplitude can be related to the focusing of seismic signals. This brightening should be considered when studying the syncline geometry of the normal drag related to the hangingwall deformation along the Maghlaq Fault (Fig. 25, 26, and 27).

6.3.3 Imaging fault complexity

In the models where a higher degree of fault complexity was introduced (lenses, fault rock, segmentation, etc.) to study the impact on seismic images, a number of different effects were seen that are discussed in the following section. Altering the fault geometry to a segmented fault (Fig. 28) or to have several overlapping fault segments (Fig. 30) widens the imaged fault zone. In all the cases, the added faults are large enough to be recognized as steps in reflections and can be distinguished as individual faults. Another effect can be studied when comparing the seismic image of the fault rock to that of the fault lens (Fig. 38a and b). The only difference is that Fig. 38b has an additional sub-seismic continuous fault rock introduced in the fault zone. The fault rock is not illuminated, but minor differences in amplitudes and interference patterns are seen when the two seismic images are compared. For instance, the braided interference patterns in the footwall are more abundant in the seismic image containing the continuous fault rock (Fig. 38b) than in the seismic image where no such feature is included (Fig. 38a). Modelling of this thin fault rock (3-6 m thick), with a high velocity, causes large impedance contrasts with the GL layer (Fig 34a). Modelling of this sub-seismic structure has shared similarities to the seismic modelling of thin sills done by Eide et al. (2018) and Rabbel et al.

(2018). Their results show that thin sills on the meter scale, i.e., below resolution, are detectable on the images because of complex interference patterns. Figure 38b and c show similar frequency-dependent interference patterns within the dashed lines. Changing the fault rock to have low seismic velocities would likely alter the number of artefacts and types of interference patterns. This effect was seen when comparing the two sets of lens images with different elastic properties. The artefacts are more prominent in the GL lens (Fig. 32) than in the LCL lens (Fig. 33). However, in the interpretation of real seismic data, interference patterns related to the elastic properties is considered unlikely to be reliably tied to any geological feature or even detected because of acquisition noise. Another difference between the seismic images of the GL lens (Fig. 38a) and the fault rock (Fig. 38b) is the disappearance of the dual reflection present in the seismic image of the GL lens (Fig. 38a). In Fig. 38b, a tuning effect occurs in the BC layer, and the lower side lobe of the upper BC reflection has merged with the base BC reflection. These observations may imply that even thin (well below seismic resolution) bodies or membranes of high-velocity fault rock may adversely affect the seismic imaging and the detectability of fault zone detail.

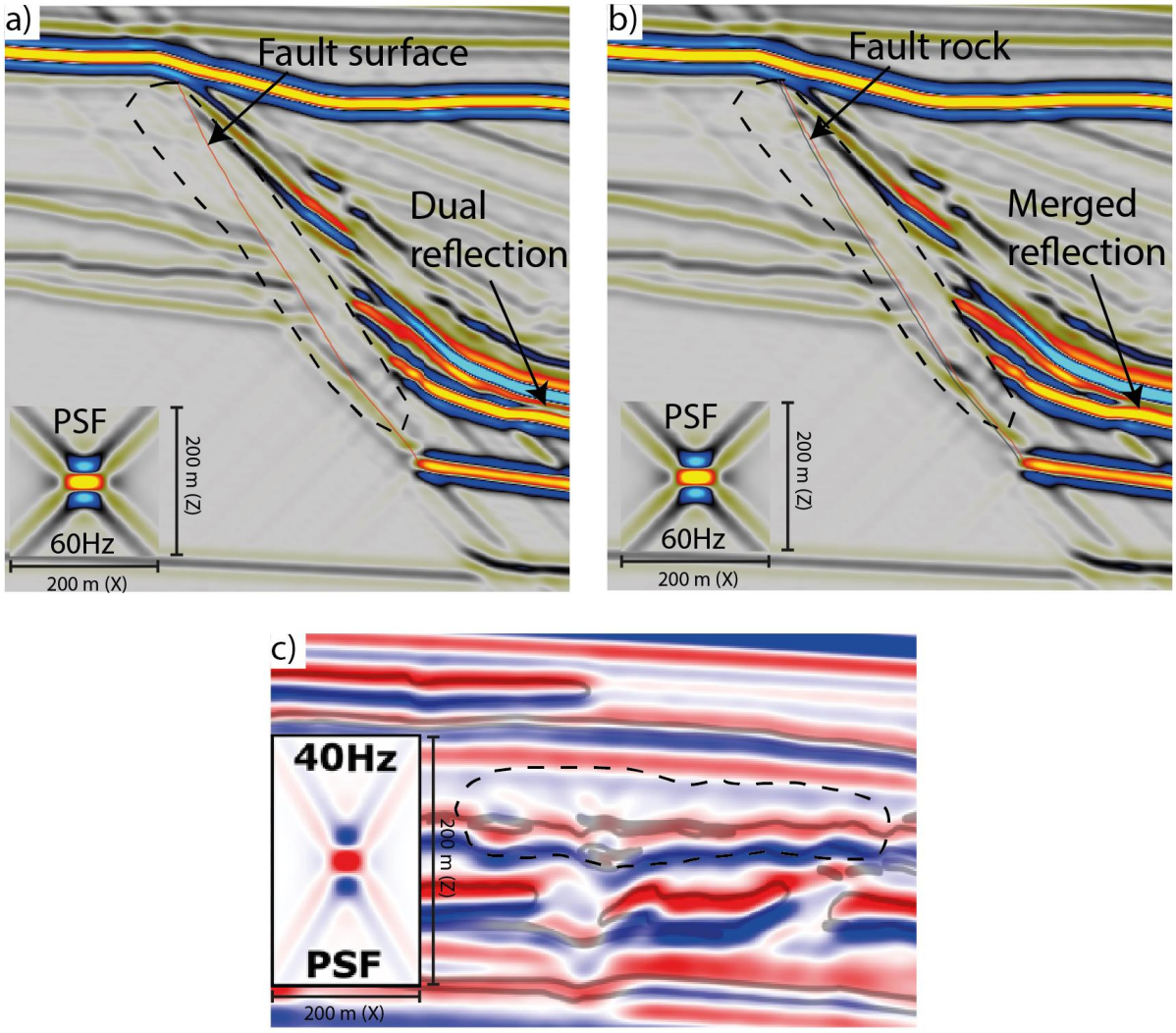

Fig 38: a) Seismic image of the 65 m thick GL lens model, including the fault surface reflector from the reflectivity model. b) Seismic image of the fault rock model, including the fault rock reflectors from the reflectivity model. c) Seismic image of thin sills detected by complex interference pattern from Rabbel et al. (2018). The dashed lines show the main areas that were compared in the seismic images.

6.4 Reflection seismic issues when imaging faults

The interpretation of faults as planar features is still common even though the literature has well established the variation in mechanical properties and fault-related deformation of faults in 3D (Childs et al., 1997; Faulkner et al., 2010). How faults are characterized in seismic is highly related to the illumination pattern and resolution of seismic images. Botter et al. (2014; 2016) found that low resolution results in the fault being displayed as a single plane in both 2D and 3D. This chapter discussed the changes in resolution related to the variation in dominant frequencies and illumination effect. The resolution of layers and internal fault zone details was shown to increase with increasing frequency. The seismic resolution still presents a problem when interpreting faults on a sub-seismic scale and interpreters have a difficult time in describing fault geometry from low-resolution seismic images. Therefore, it is crucial to have

knowledge about fault systems while doing seismic interpretation (e.g., Townsend et al., 1998, Long and Imber, 2011).

Another challenge associated with discontinuities, e.g., faults, is the related diffraction of seismic energy. Distortion from the diffraction makes it harder to interpret the fault in the seismic images. In Fig. 25b-d, diffracted energy from the folded hangingwall layers along the fault surface interferes with overburden and the underlying layers in the seismic images. Diffraction is especially visible at higher frequencies (Fig. 25c and d). Nonetheless, Botter et al. (2014; 2016) used diffraction and fault internal interaction of reflectors to approximately define the extent of the fault. However, diffractions are typically weaker than reflections, thus processing of seismic data is usually done for reflections and diffractions are removed during data migration (Landa, 2012).

6.5 Implications and applications

Faults and fractures exert strong control on fluid flow in subsurface reservoirs, which is dependent on the properties of the internal structural heterogeneities. These properties can be implemented when performing reservoir modelling to understand fluid flow (Kolyukhin et al., 2017). However, faults are rarely drilled, and in some cases, only seismic data are available to study. Including fault zone elements of different sizes and geometries in seismic modelling, such as in this study, provides a better understanding of the relationship between the seismic image and the geological and elastic properties of faults and internal fault zone features (fault rock, lenses, etc.). Although a direct correlation between the image and the specific geological structures and rock properties has not been made, studies like this contribute to a more informed fault interpretation. Using seismic amplitude variations may increase the understanding of the internal properties of a fault, but are not sufficient for an interpreter to decide whether a fault acts as a barrier or a conduit to fluids. Botter et al. (2016) took it a step further by mapping geobodies of fault damage in 3D seismic, which better related seismic amplitudes to the distribution of elastic properties. Rock physics modelling can be used to first generate elastic properties from petrophysics and fluids (e.g., Johansen, 2018). Then cases with different fluid contents across the fault can be modelled to better appreciate what could be detected. However, modelling of elastic properties where fluids were especially considered was not done in this thesis. Besides, rock physics in carbonate rocks and reservoirs are difficult because of their heterogeneity in porosity and permeability at all scales. As seen in the seismic images modelled with different dominant frequencies (e.g., Fig. 25, 26, and 27), information retrieved from

seismic is highly dependent on the resolution and illumination, and important structures may be overlooked, e.g., Fig. 34. An understanding of reservoir connectivity should consider sub-seismic structures in reservoir simulation because of their impact on fluid flow (Rotevatn and Fossen, 2011). Qu and Tveranger (2016) demonstrated that reservoir models that included damage zone properties exhibit different responses when compared to models without these properties. Modelling of fault facies has mainly focused on siliciclastic reservoirs even though carbonates account for approximately 50% of today's hydrocarbon production (e.g., Fredman et al., 2008; Burchette, 2012). A major challenge with carbonates are the high and local variations in porosity and permeability making them strongly heterogeneous (Mazzullo, 2004). Nevertheless, they share similar fault zone elements with siliciclastics, such as lenses, breccias, slip surfaces, cataclasis, and deformation band. In carbonates, fault cores are considered barriers to fluid flow, whereas the damage zone works as a conduit for flow (e.g., Bonson et al., 2007; Bastesen and Braathen, 2010).

7. CONCLUSIONS AND FURTHER WORK

7.1 Conclusions

The main aim of this thesis was to improve the understanding of seismic imaging of faults in carbonate rocks through seismic modelling of geological cross-sections across the Maghlaq Fault in Malta. The investigating of seismic signatures of fault geometries and different fault zone elements contribute to an improved understanding of seismic response of carbonate hosted normal faults. Based on the results presented in this thesis, the main conclusions are:

1. Vertical and horizontal resolution of the seismic image is strongly controlled by the illumination and dominant frequency. The Maghlaq Fault is recognized at 20, 40, and 60 Hz by the termination of footwall reflections and fault-related ductile deformation in the hangingwall reflections. At low frequencies (20 Hz), there are few details resolved and the apparent dip of the fault is significantly lower than the true dip.
2. Steeply dipping (more than 45°) fault zone structures on seismic scale are not resolved due to illumination issues. Instead, they contribute to increased discontinuity, complex interference patterns, and artefacts generated from the PSF cross-pattern originating from diffraction points as well as interference from surrounding, illuminated structures.
3. Elastic properties impact the reflection characterization and delineation of structural geometries with inclined and intersecting acoustic impedance boundaries due to constructive and destructive interference.
4. Segmented and overlapping fault segments are recognized as individual steps in reflections, and result in increased apparent thickness of the fault zone.
5. Including a high velocity, sub-seismic structure (fault rock) in the 2D geological model generates complex interference patterns in the synthetic seismic image and may deteriorate seismic detectability due to an increased mean velocity in the model.

The results from the 2D seismic modelling in this thesis may help contribute towards more informed fault interpretations. By providing an investigation into the effects of various fault zone complexities on synthetic seismic images, such insight may help seismic interpreters better understand the relationship between seismic images and structures in the subsurface, which in turn is a prerequisite to understanding fluid flow in subsurface reservoirs, e.g., for hydrocarbons, groundwater or for geologic carbon storage.

7.2 Suggested further work

This project is a contribution to a better understanding of seismic imaging of carbonate-hosted faults. There are several avenues for future work building on this study:

- Include acquisition noise to make the seismic images more comparable to real seismic and to investigate the degree to which it affects the detectability of sub-seismic structures.
- Include a complex overburden in order to investigate how the seismic signal is affected.
- Further investigation on the seismic response through sensitivity analysis of changing the seismic survey parameters, such as survey geometry, wavelet, and illumination angle.
- Include a velocity- and density change with depth in the geological models for more realistic modelling.
- Generate 3D synthetic seismic from outcrop data of the Maghlaq Fault to better investigate the impact of 3D structures in seismic sections.

8. REFERENCES

ADAM, L., BATZLE, M., LEWALLEN, K. & VAN WIJK, K. 2009. Seismic wave attenuation in carbonates. *Journal of Geophysical Research: Solid Earth,* 114**,** 14.

AGOSTA, F., PRASAD, M. & AYDIN, A. 2007. Physical properties of carbonate fault rocks, fucino basin (Central Italy): implications for fault seal in platform carbonates. *Geofluids,* 7**,** 19-32.

ANDERSEN, I. G. 2020. *Effects of geophysical parameters on the seismic expression of the Maghlaq Fault, Malta: insights from outcrop-based 2D seismic modeling.* The University of Bergen.

ANSELMETTI, F. S. & EBERLI, G. P. 1993. Controls on sonic velocity in carbonates. *Pure and Applied geophysics,* 141**,** 287-323.

ARGNANI, A. 1990. The Strait of Sicily rift zone: foreland deformation related to the evolution of a back-arc basin. *Journal of Geodynamics,* 12**,** 311-331.

ARGNANI, A. 2009. Evolution of the southern Tyrrhenian slab tear and active tectonics along the western edge of the Tyrrhenian subducted slab. *Geological Society, London, Special Publications,* 311**,** 193-212.

BASTESEN, E. 2010. Facies composition and scaling of extensional faults in sedimentary rocks and its applications to modelling of fault zones.

BASTESEN, E. & BRAATHEN, A. 2010. Extensional faults in fine grained carbonates–analysis of fault core lithology and thickness–displacement relationships. *Journal of Structural Geology,* 32**,** 1609-1628.

BIJU-DUVAL, B. & DERCOURT, J. 1980. Les bassins de la Mediterranee orientale representent-ils les restes d'un domaine oceanique, la Mesogee, ouvert au Mesozoique et distinct de la Tethys? *Bulletin de la societe Geologique de France,* 7**,** 43-60.

BILLI, A., SALVINI, F. & STORTI, F. 2003. The damage zone-fault core transition in carbonate rocks: implications for fault growth, structure and permeability. *Journal of Structural geology,* 25**,** 1779-1794.

BONSON, C. G., CHILDS, C., WALSH, J. J., SCHOPFER, M. P. J. & CARBONI, V. 2007. Geometric and kinematic controls on the internal structure of a large normal fault in massive limestones: The Maghlaq Fault, Malta. *Journal of Structural Geology,* 29**,** 336-354.

BOSCH, M., MUKERJI, T. & GONZALEZ, E. F. 2010. Seismic inversion for reservoir properties combining statistical rock physics and geostatistics: A review. *Geophysics,* 75**,** 75A165-75A176.

BOSENCE, D. W. & PEDLEY, H. M. 1982. Sedimentology and palaeoecology of a Miocene coralline algal biostrome from the Maltese Islands. *Palaeogeography, palaeoclimatology, palaeoecology,* 38**,** 9-43.

BOSMAN, A., CALARCO, M., CASALBORE, D., CHIOCCI, F., COLTELLI, M., CONTE, A., MARTORELLI, E., ROMAGNOLI, C. & SPOSATO, A. 2008. Submarine volcanic features in the Pantelleria offshore revealed by high resolution swath bathymetry. *Rendic Soc Geol Ital,* 3**,** 128-129.

BOTTER, C., CARDOZO, N., HARDY, S., LECOMTE, I. & ESCALONA, A. 2014. From mechanical modeling to seismic imaging of faults: A synthetic workflow to study the impact of faults on seismic. *Marine and Petroleum Geology,* 57**,** 187-207.

BOTTER, C., CARDOZO, N., HARDY, S., LECOMTE, I., PATON, G. & ESCALONA, A. 2016. Seismic characterisation of fault damage in 3D using mechanical and seismic modelling. *Marine and Petroleum Geology,* 77**,** 973-990.

BRANDSÆTER, I., MCILROY, D., LIA, O., RINGROSE, P. & NÆSS, A. 2005. Reservoir modelling and simulation of Lajas Formation outcrops (Argentina) to constrain tidal reservoirs of the Halten Terrace (Norway). *Petroleum Geoscience,* 11**,** 37-46.

BRAATHEN, A., TVERANGER, J., FOSSEN, H., SKAR, T., CARDOZO, N., SEMSHAUG, S., BASTESEN, E. & SVERDRUP, E. 2009. Fault facies and its application to sandstone reservoirs. *AAPG bulletin,* 93**,** 891-917.

BUCKLEY, S. J., RINGDAL, K., NAUMANN, N., DOLVA, B., KURZ, T. H., HOWELL, J. A. & DEWEZ, T. J. 2019. LIME: Software for 3-D visualization, interpretation, and communication of virtual geoscience models. *Geosphere,* 15**,** 222-235.

BURCHETTE, T. P. 2012. Carbonate rocks and petroleum reservoirs: a geological perspective from the industry. *Geological Society, London, Special Publications,* 370**,** 17-37.

CAINE, J. S., EVANS, J. P. & FORSTER, C. B. 1996. Fault zone architecture and permeability structure. *Geology,* 24**,** 1025-1028.

CASTAGNA, J., BATZLE, M., KAN, T. & BACKUS, M. 1993. Rock physics—The link between rock properties and AVO response. *Offset-dependent reflectivity—Theory and practice of AVO analysis: SEG.* 8 ed. Houston: Society of Exploration Geophysicists.

CAVAZZA, W. & WEZEL, F. C. 2003. The Mediterranean region-a geological primer. *Episodes,* 26**,** 160-168.

CELLO, G. 1987. Structure and deformation processes in the Strait of Sicily "rift zone". *Tectonophysics,* 141**,** 237-247.

CHESTER, F. & LOGAN, J. M. 1986. Implications for mechanical properties of brittle faults from observations of the Punchbowl fault zone, California. *Pure and Applied Geophysics,* 124**,** 79-106.

CHESTER, F. M., EVANS, J. P. & BIEGEL, R. L. 1993. Internal structure and weakening mechanisms of the San Andreas fault. *Journal of Geophysical Research: Solid Earth,* 98**,** 771-786.

CHILDS, C., MANZOCCHI, T., NICOL, A., WALSH, J., SODEN, A., CONNEALLY, J. & DELOGKOS, E. 2017. The relationship between normal drag, relay ramp aspect ratio and fault zone structure. *Geological Society, London, Special Publications,* 439**,** 355-372.

CHILDS, C., MANZOCCHI, T., WALSH, J. J., BONSON, C. G., NICOL, A. & SCHÖPFER, M. P. 2009. A geometric model of fault zone and fault rock thickness variations. *Journal of Structural Geology,* 31**,** 117-127.

CHILDS, C., WALSH, J. & WATTERSON, J. 1997. Complexity in fault zone structure and implications for fault seal prediction. *Hydrocarbon seals: Importance for exploration and production,* 7**,** 61-72.

CIVILE, D., LODOLO, E., ACCETTELLA, D., GELETTI, R., BEN-AVRAHAM, Z., DEPONTE, M., FACCHIN, L., RAMELLA, R. & ROMEO, R. 2010. The Pantelleria graben (Sicily Channel, Central Mediterranean): an example of intraplate 'passive'rift. *Tectonophysics,* 490**,** 173-183.

CIVILE, D., LODOLO, E., TORTORICI, L., LANZAFAME, G. & BRANCOLINI, G. 2008. Relationships between magmatism and tectonics in a continental rift: the Pantelleria Island region (Sicily Channel, Italy). *Marine Geology,* 251**,** 32-46.

COOKE, A. P., FISHER, Q. J., MICHIE, E. A. & YIELDING, G. 2018. Investigating the controls on fault rock distribution in normal faulted shallow burial limestones, Malta, and the implications for fluid flow. *Journal of Structural Geology,* 114**,** 22-42.

CUNNINGHAM, J., CARDOZO, N., TOWNSEND, C., IACOPINI, D. & WAERUM, G. O. 2019. Fault deformation, seismic amplitude and unsupervised fault facies analysis: Snøhvit Field, Barents Sea. *Journal of Structural Geology,* 118**,** 165-180.

DART, C., BOSENCE, D. & MCCLAY, K. 1993. Stratigraphy and structure of the Maltese graben system. *Journal of the Geological Society,* 150**,** 1153-1166.

DE VOOGD, B., TRUFFERT, C., CHAMOT-ROOKE, N., HUCHON, P., LALLEMANT, S. & LE PICHON, X. 1992. Two-ship deep seismic soundings in the basins of the Eastern Mediterranean Sea (Pasiphae cruise). *Geophysical Journal International,* 109**,** 536-552.

DEWEY, J., HELMAN, M., KNOTT, S., TURCO, E. & HUTTON, D. 1989. Kinematics of the western Mediterranean. *Geological Society, London, Special Publications,* 45**,** 265-283.

DIMMEN, V., ROTEVATN, A., PEACOCK, D. C., NIXON, C. W. & NÆRLAND, K. 2017. Quantifying structural controls on fluid flow: Insights from carbonate-hosted fault damage zones on the Maltese Islands. *Journal of Structural Geology,* 101**,** 43-57.

DREYER, T., FÄLT, L. M., HØY, T., KNARUD, R., STEEL §, R. & CUEVAS, J. L. 1992. Sedimentary architecture of field analogues for reservoir information (SAFARI): a case study of the fluvial Escanilla Formation, Spanish Pyrenees. *The geological modelling of hydrocarbon reservoirs and outcrop analogues***,** 57-80.

DUTZER, J.-F., BASFORD, H. & PURVES, S. 2010. Investigating fault-sealing potential through fault relative seismic volume analysis. *Geological Society, London, Petroleum Geology Conference series,* 7**,** 509-515.

DVORKIN, J., WALLS, J. D. & MAVKO, G. 2001. Rock physics of marls. *SEG Technical Program Expanded Abstracts 2001***,** 1784-1787.

EBERLI, G. P., BAECHLE, G. T., ANSELMETTI, F. S. & INCZE, M. L. 2003. Factors controlling elastic properties in carbonate sediments and rocks. *The Leading Edge,* 22**,** 654-660.

EBERLI, G. P., MASAFERRO, J. L. & SARG, J. R. 2004. Seismic imaging of carbonate reservoirs and systems. *AAPG Memoir,* 81**,** 1-9.

EIDE, C. H., SCHOFIELD, N., LECOMTE, I., BUCKLEY, S. J. & HOWELL, J. A. 2018. Seismic interpretation of sill complexes in sedimentary basins: implications for the sub-sill imaging problem. *Journal of the Geological Society,* 175**,** 193-209.

ELTER, P., GRASSO, M., PAROTTO, M. & VEZZANI, L. 2003. Structural setting of the Apennine-Maghrebian thrust belt. *Episodes,* 26**,** 205-211.

ENGE, H. V. D. & HOWELL, J. A. 2010. Impact of deltaic clinothems on reservoir performance: Dynamic studies of reservoir analogs from the Ferron Sandstone Member and Panther Tongue, Utah. *AAPG bulletin,* 94**,** 139-161.

FAULKNER, D., JACKSON, C., LUNN, R., SCHLISCHE, R., SHIPTON, Z., WIBBERLEY, C. & WITHJACK, M. 2010. A review of recent developments concerning the structure, mechanics and fluid flow properties of fault zones. *Journal of Structural Geology,* 32**,** 1557-1575.

FAULKNER, D., MITCHELL, T., JENSEN, E. & CEMBRANO, J. 2011. Scaling of fault damage zones with displacement and the implications for fault growth processes. *Journal of Geophysical Research: Solid Earth,* 116.

FELIX, R. 1973. Oligo-Miocene stratigraphy of Malta and Gozo. *Veenman,* No.73-20.

FERRILL, D. A. & MORRIS, A. P. 2003. Dilational normal faults. *Journal of Structural Geology,* 25**,** 183-196.

FOSSEN, H. & GABRIELSEN, R. H. 1996. Experimental modeling of extensional fault systems by use of plaster. *Journal of Structural Geology,* 18**,** 673-687.

FOSSEN, H. & ROTEVATN, A. 2016. Fault linkage and relay structures in extensional settings—A review. *Earth-Science Reviews,* 154**,** 14-28.

FREDMAN, N., TVERANGER, J., CARDOZO, N., BRAATHEN, A., SOLENG, H., RØE, P., SKORSTAD, A. & SYVERSVEEN, A. R. 2008. Fault facies modeling: Technique and approach for 3-D conditioning and modeling of faulted grids. *AAPG bulletin,* 92**,** 1457-1478.

FURLANI, S., ANTONIOLI, F., GAMBIN, T., GAUCI, R., NINFO, A., ZAVAGNO, E., MICALLEF, A. & CUCCHI, F. 2017. Marine notches in the Maltese islands (central Mediterranean Sea). *Quaternary International,* 439**,** 158-168.

FÆRSETH, R. B. 2006. Shale smear along large faults: continuity of smear and the fault seal capacity. *Journal of the Geological Society,* 163**,** 741-751.

GARDINER, W., GRASSO, M. & SEDGELEY, D. 1995. Plio-pleistocene fault movement as evidence for mega-block kinematics within the Hyblean—Malta Plateau, Central Mediterranean. *Journal of geodynamics,* 19**,** 35-51.

GARDNER, G., GARDNER, L. & GREGORY, A. 1974. Formation velocity and density—The diagnostic basics for stratigraphic traps. *Geophysics,* 39**,** 770-780.

GAUTHIER, B. & LAKE, S. 1993. Probabilistic modeling of faults below the limit of seismic resolution in Pelican Field, North Sea, offshore United Kingdom. *AAPG bulletin,* 77**,** 761-777.

GRANATH, J. W. & CASERO, P. 2004. Tectonic setting of the petroleum systems of Sicily.

GUEGUEN, E., DOGLIONI, C. & FERNANDEZ, M. J. T. 1998. On the post-25 Ma geodynamic evolution of the western Mediterranean. *Tectonophysics,* 298**,** 259-269.

HARDACRE, K. & COWIE, P. 2003. Variability in fault size scaling due to rock strength heterogeneity: a finite element investigation. *Journal of structural geology,* 25**,** 1735-1750.

HEALY, D., NEILSON, J. E., HAINES, T. J., MICHIE, E. A., TIMMS, N. E. & WILSON, M. E. 2015. An investigation of porosity–velocity relationships in faulted carbonates using outcrop analogues. *Geological Society, London, Special Publications,* 406**,** 261-280.

HERRON, D. A. 2011. *First steps in seismic interpretation,* USA, Society of Exploration Geophysicists.

HOWELL, J. A., MARTINIUS, A. W. & GOOD, T. R. 2014. The application of outcrop analogues in geological modelling: a review, present status and future outlook. *Geological Society, London, Special Publications,* 387**,** 1-25.

ILLIES, J. H. 1969. An intercontinental belt of the world rift system. *Tectonophysics,* 8**,** 5-29.

ILLIES, J. H. 1981. Graben formation—the Maltese Islands—a case history. *Developments in Geotectonics.* Elsevier.

JEANNE, P., GUGLIELMI, Y. & CAPPA, F. 2012. Multiscale seismic signature of a small fault zone in a carbonate reservoir: Relationships between VP imaging, fault zone architecture and cohesion. *Tectonophysics,* 554**,** 185-201.

JOHANSEN, M. K. 2018. *A modelling workflow for seismic characterization of paleokarst reservoirs.* The University of Bergen.

JOLLEY, S., BARR, D., WALSH, J. & KNIPE, R. 2007. Structurally complex reservoirs: an introduction. *Geological Society, London, Special Publications,* 292**,** 1-24.

JONGSMA, D., VAN HINTE, J. E. & WOODSIDE, J. M. 1985. Geologic structure and neotectonics of the North African continental margin south of Sicily. *Marine and petroleum Geology,* 2**,** 156-179.

KEAREY, P., BROOKS, M. & HILL, I. 2002. An introduction to geophysical exploration. Third ed. Oxford: Blackwell Science Ltd.

KOLYUKHIN, D. R., LISITSA, V. V., PROTASOV, M. I., QU, D., RESHETOVA, G. V., TVERANGER, J., TCHEVERDA, V. A. & VISHNEVSKY, D. M. 2017. Seismic imaging and statistical analysis of fault facies models. *Interpretation,* 5**,** SP71-SP82.

LANDA, E. 2012. Seismic diffraction: Where's the value? *SEG Technical Program Expanded Abstracts 2012.* Society of Exploration Geophysicists.

LECOMTE, I. 2008. Resolution and illumination analyses in PSDM: A ray-based approach. *The Leading Edge,* 27**,** 650-663.

LECOMTE, I., LAVADERA, P. L., ANELL, I., BUCKLEY, S. J., SCHMID, D. W. & HEEREMANS, M. 2015. Ray-based seismic modeling of geologic models: Understanding and analyzing seismic images efficiently. *Interpretation,* 3**,** SAC71-SAC89.

LECOMTE, I., LAVADERA, P. L., BOTTER, C., ANELL, I., BUCKLEY, S. J., EIDE, C. H., GRIPPA, A., MASCOLO, V. & KJOBERG, S. 2016. 2 (3) D convolution modelling of complex geological targets beyond–1D convolution. *First Break,* 34.

LINES, L. R. & NEWRICK, R. T. 2004. *Fundamentals of geophysical interpretation,* Tulsa, OK, Society of Exploration Geophysicists.

LONG, J. J. & IMBER, J. 2011. Geological controls on fault relay zone scaling. *Journal of Structural Geology,* 33**,** 1790-1800.

LUBRANO-LAVADERA, P., SENGER, K., LECOMTE, I., MULROONEY, M. J. & KÜHN, D. 2019. Seismic modelling of metre-scale normal faults at a reservoir-cap rock interface in Central Spitsbergen, Svalbard: implications for CO2 storage. *Norwegian Journal of Geology,* 99**,** 329-347.

MALINVERNO, A. & RYAN, W. B. J. T. 1986. Extension in the Tyrrhenian Sea and shortening in the Apennines as result of arc migration driven by sinking of the lithosphere. *Tectonics,* 5**,** 227-245.

MANZOCCHI, T., CHILDS, C. & WALSH, J. 2010. Faults and fault properties in hydrocarbon flow models. *Geofluids,* 10**,** 94-113.

MATONTI, C., LAMARCHE, J., GUGLIELMI, Y. & MARIÉ, L. 2012. Structural and petrophysical characterization of mixed conduit/seal fault zones in carbonates: example from the Castellas fault (SE France). *Journal of Structural Geology,* 39**,** 103-121.

MAZZULLO, S. 2004. Overview of porosity evolution in carbonate reservoirs. *Kansas Geological Society Bulletin,* 79**,** 1-19.

MICALLEF, A., FOGLINI, F., LE BAS, T., ANGELETTI, L., MASELLI, V., PASUTO, A. & TAVIANI, M. 2013. The submerged paleolandscape of the Maltese Islands: Morphology, evolution and relation to Quaternary environmental change. *Marine Geology,* 335**,** 129-147.

MICARELLI, L., BENEDICTO, A. & WIBBERLEY, C. 2006. Structural evolution and permeability of normal fault zones in highly porous carbonate rocks. *Journal of Structural Geology,* 28**,** 1214-1227.

MICHIE, E., HAINES, T., HEALY, D., NEILSON, J., TIMMS, N. E. & WIBBERLEY, C. 2014. Influence of carbonate facies on fault zone architecture. *Journal of Structural Geology,* 65**,** 82-99.

MILLER, S. L. 1992. Well log analysis of Vp and Vs in carbonates. *Consurtium for Research in Elastic Wave Exploration Seismology (CREWES) Research Report,* 4**,** 1-12.

MORELLI, C., GANTAR, C. & PISANI, M. 1975. Bathymetry, gravity and magnetism in the Strait of Sicily and in the Ionian Sea. *Boll. Geofis. teor. appl,* 17**,** 39-58.

PEACOCK, D., FISHER, Q., WILLEMSE, E. & AYDIN, A. 1998. The relationship between faults and pressure solution seams in carbonate rocks and the implications for fluid flow. *Geological Society, London, Special Publications,* 147**,** 105-115.

PEDLEY, H. M., HOUSE, M. R. & WAUGH, B. 1976. The geology of Malta and Gozo. *Proceedings of the Geologists' Association,* 87**,** 325-341.

PICKETT, G. R. 1963. Acoustic character logs and their applications in formation evaluation. *Journal of Petroleum technology,* 15**,** 659-667.

QU, D. & TVERANGER, J. 2016. Incorporation of deformation band fault damage zones in reservoir models. *AAPG Bulletin,* 100**,** 423-443.

RABBEL, O., GALLAND, O., MAIR, K., LECOMTE, I., SENGER, K., SPACAPAN, J. B. & MANCEDA, R. 2018. From field analogues to realistic seismic modelling: a case study of an oil-producing andesitic sill complex in the Neuquén Basin, Argentina. *Journal of the Geological Society,* 175**,** 580-593.

REUTHER, C.-D. & EISBACHER, G. 1985. Pantelleria Rift—crustal extension in a convergent intraplate setting. *Geologische Rundschau,* 74**,** 585-597.

RICKER, N. 1940. The form and nature of seismic waves and the structure of seismograms. *Geophysics,* 5**,** 348-366.

ROSENBAUM, G., LISTER, G. S. & DUBOZ, C. 2002. Reconstruction of the tectonic evolution of the western Mediterranean since the Oligocene. *Journal of the Virtual Explorer,* 8**,** 107-130.

ROTEVATN, A. & FOSSEN, H. 2011. Simulating the effect of subseismic fault tails and process zones in a siliciclastic reservoir analogue: Implications for aquifer support and trap definition. *Marine and Petroleum Geology,* 28**,** 1648-1662.

SAMS, M., BEGG, P. & MANAPOV, T. 2017. Seismic inversion of a carbonate buildup: A case study. *Interpretation,* 5**,** T641-T652.

SHERIFF, R. E. 1977. Limitations on Resolution of Seismic Reflections and Geologic Detail Derivable from Them: Section 1. Fundamentals of Stratigraphic Interpretation of Seismic Data. *M 26: Seismic Stratigraphy - Applications to Hydrocarbon Exploration.* Tulsa, OK: AAPG.

SHERIFF, R. E. 2002. *Encyclopedic dictionary of applied geophysics,* SEG Books, Tulsa, OK, Society of exploration geophysicists.

SIBSON, R. 1977. Fault rocks and fault mechanisms. *Journal of the Geological Society,* 133**,** 191-213.

SIMM, R., BACON, M. & BACON, M. 2014. *Seismic Amplitude: An interpreter's handbook,* Cambridge, England, Cambridge University Press.

SKIRIUS, C., NISSEN, S., HASKELL, N., MARFURT, K., HADLEY, S., TERNES, D., MICHEL, K., REGLAR, I., D'AMICO, D. & DELIENCOURT, F. 1999. 3-D seismic attributes applied to carbonates. *The Leading Edge,* 18**,** 384-393.

SKURTVEIT, E., TORABI, A., GABRIELSEN, R. H. & ZOBACK, M. D. 2013. Experimental investigation of deformation mechanisms during shear-enhanced compaction in poorly lithified sandstone and sand. *Journal of Geophysical Research: Solid Earth,* 118**,** 4083-4100.

TOSAYA, C. & NUR, A. 1982. Effects of diagenesis and clays on compressional velocities in rocks. *Geophysical Research Letters,* 9**,** 5-8.

TOWNSEND, C., FIRTH, I., WESTERMAN, R., KIRKEVOLLEN, L., HÅRDE, M. & ANDERSEN, T. 1998. Small seismic-scale fault identification and mapping. *Geological Society, London, Special Publications,* 147**,** 1-25.

WAGNER, P. D. 1997. Seismic signatures of carbonate diagenesis. *Carbonate Seismology***,** 307-320.

WEBER, K. 1987. Computation of initial well productivities in aeolian sandstone on the basis of a geological model, Leman gas field, UK.

WIDESS, M. 1973. How thin is a thin bed? *Geophysics,* 38**,** 1176-1180.

APPENDIX I: GEOLOGICAL MODELS

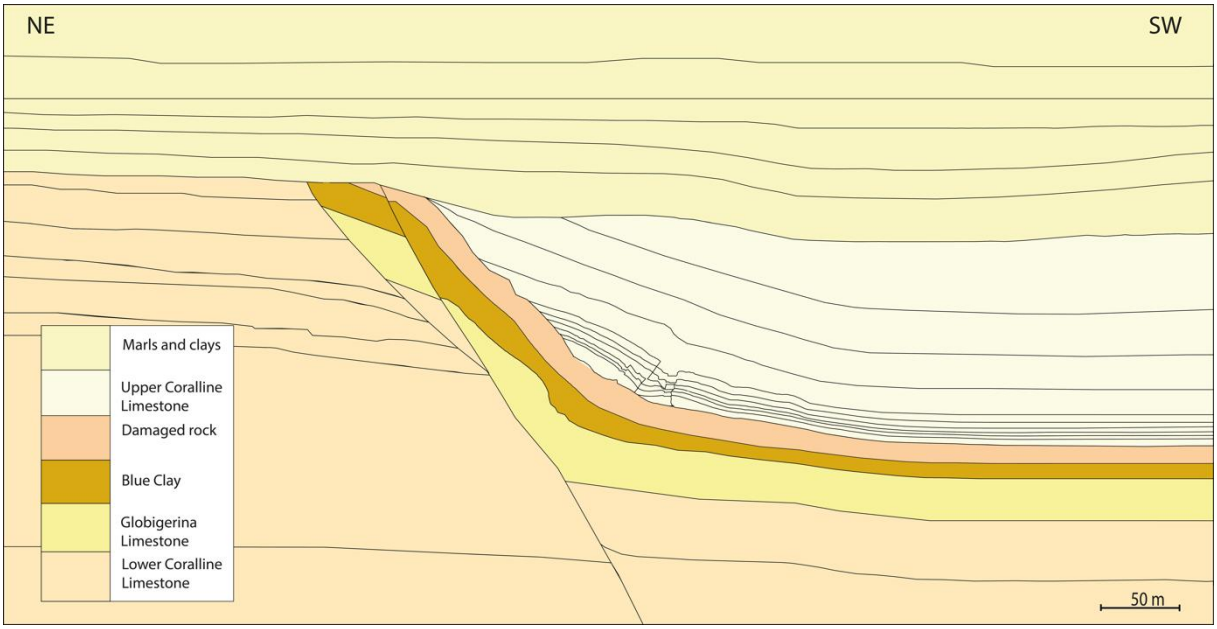

Fig. A 1: 2D Geological model of Locality 1 including a conceptual segmented fault

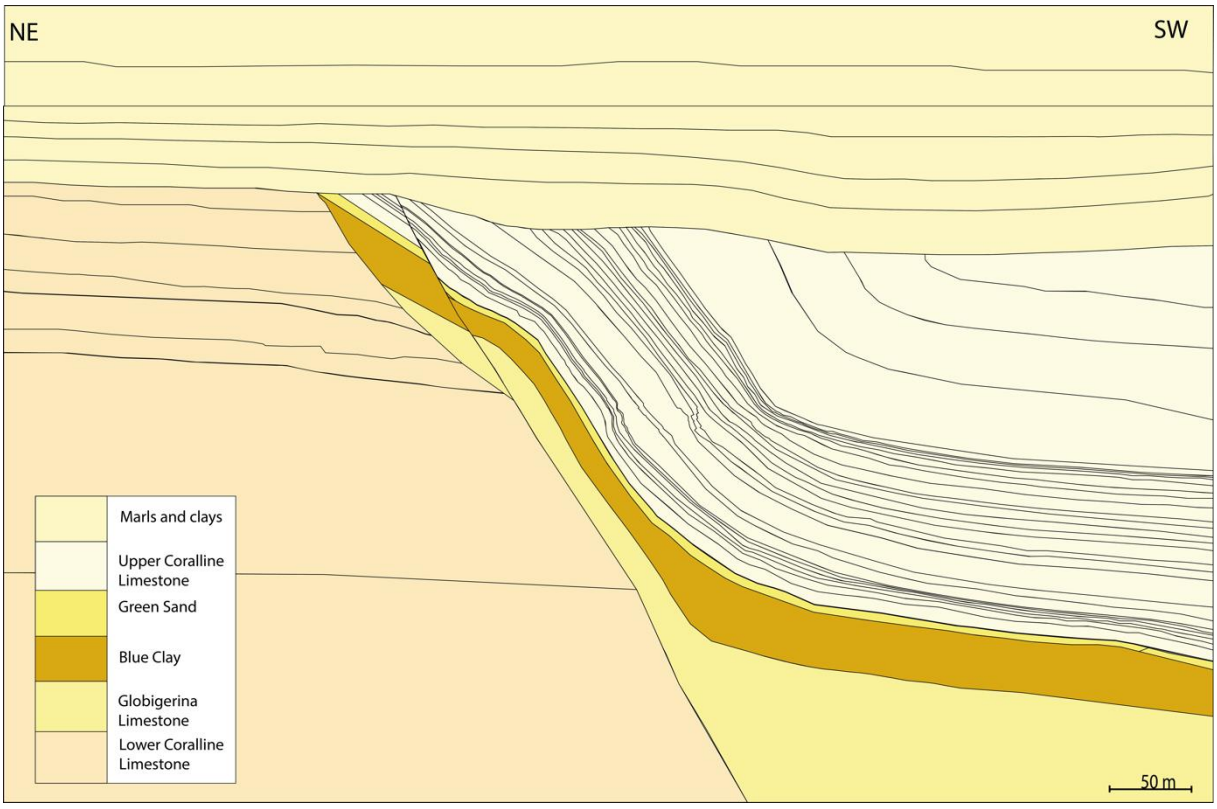

Fig. A 2: 2D Geological model of Locality 2 including a conceptual segmented fault.

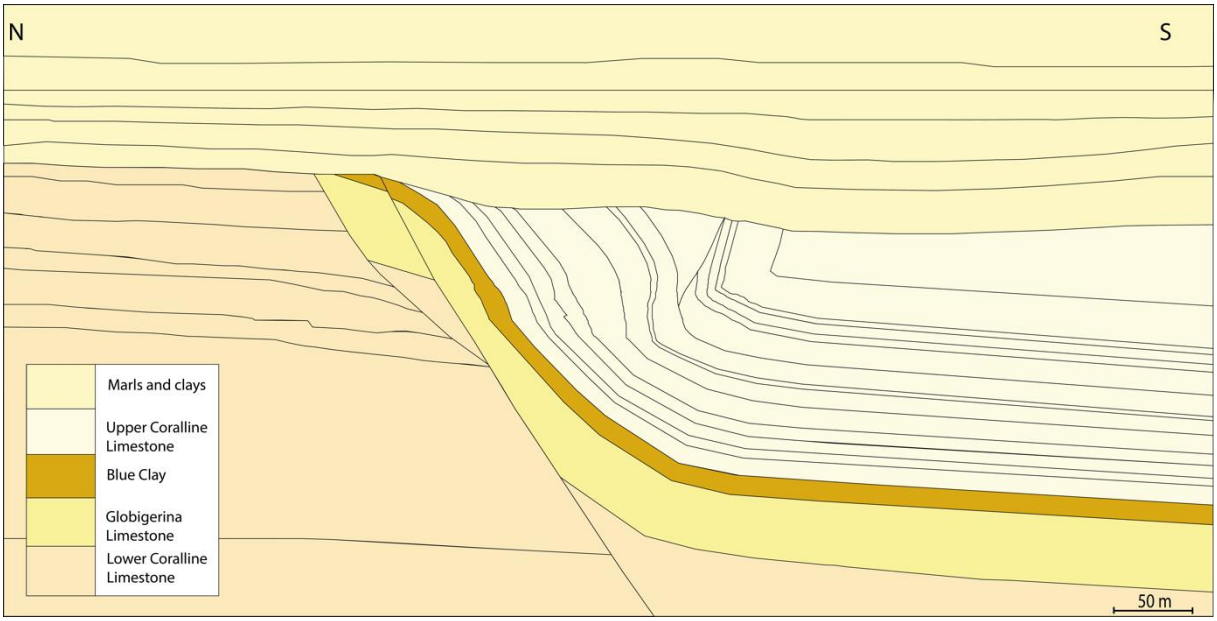

Fig. A 3: 2D Geological model of Locality 3 including a conceptual segmented fault.

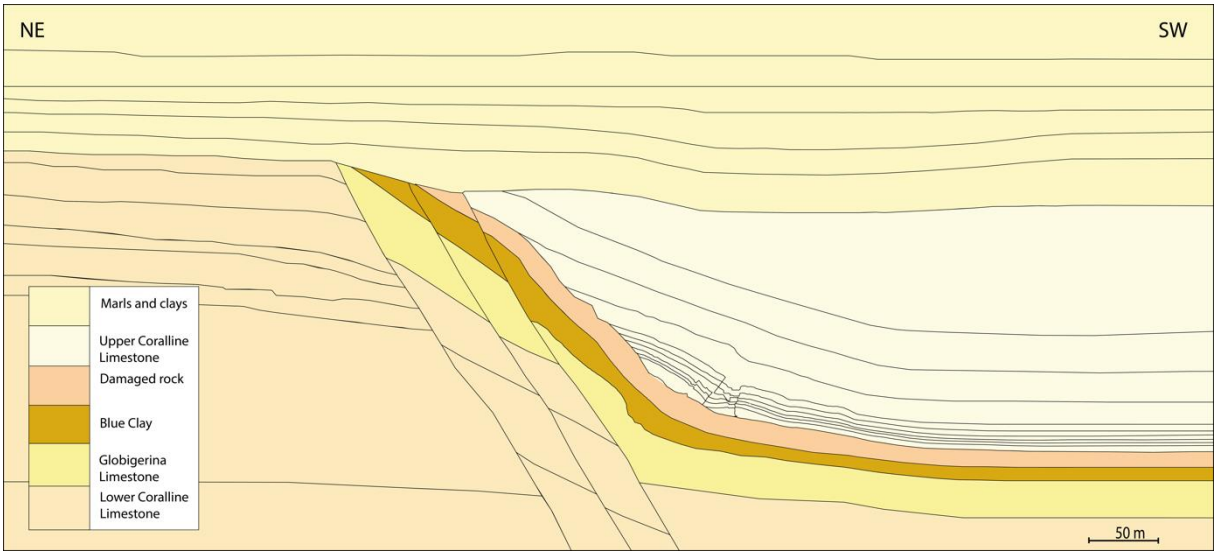

Fig. A 4: 2D Geological model of Locality 1 including conceptual overlapping fault segments.

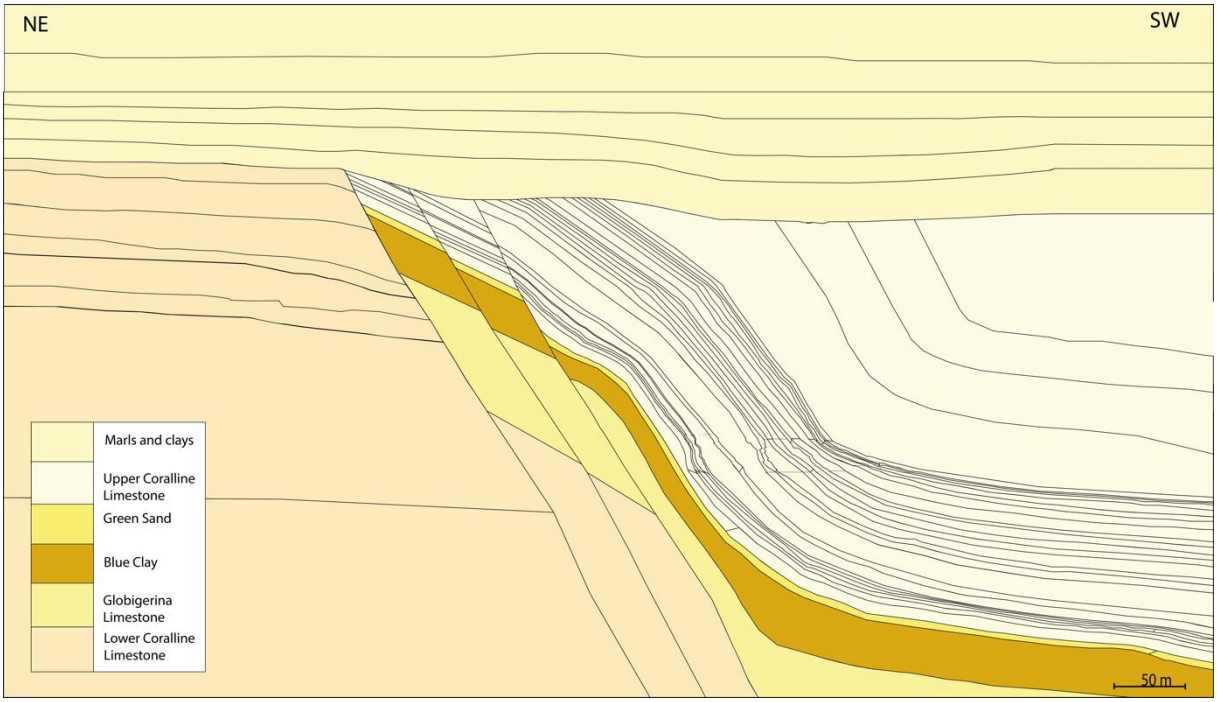

Fig. A 5: 2D Geological model of Locality 2 including conceptual overlapping fault segments.

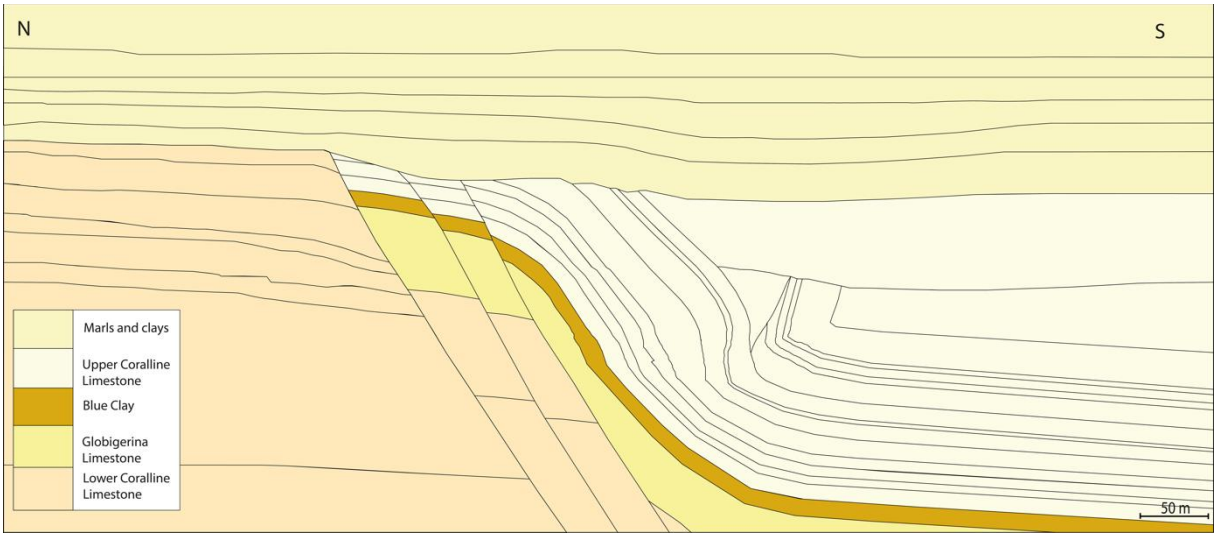

Fig. A 6: 2D Geological model of Locality 3 including conceptual overlapping fault segments.

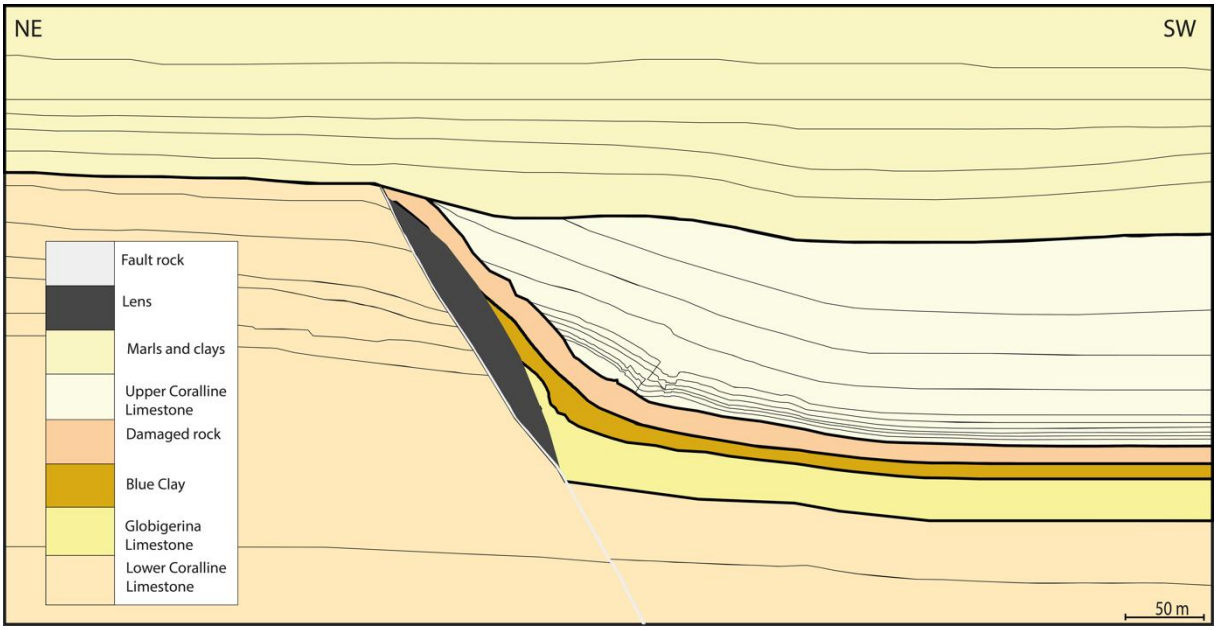

Fig. A 7: 2D Geological model of Locality 1 including a conceptual fault rock and a lens.

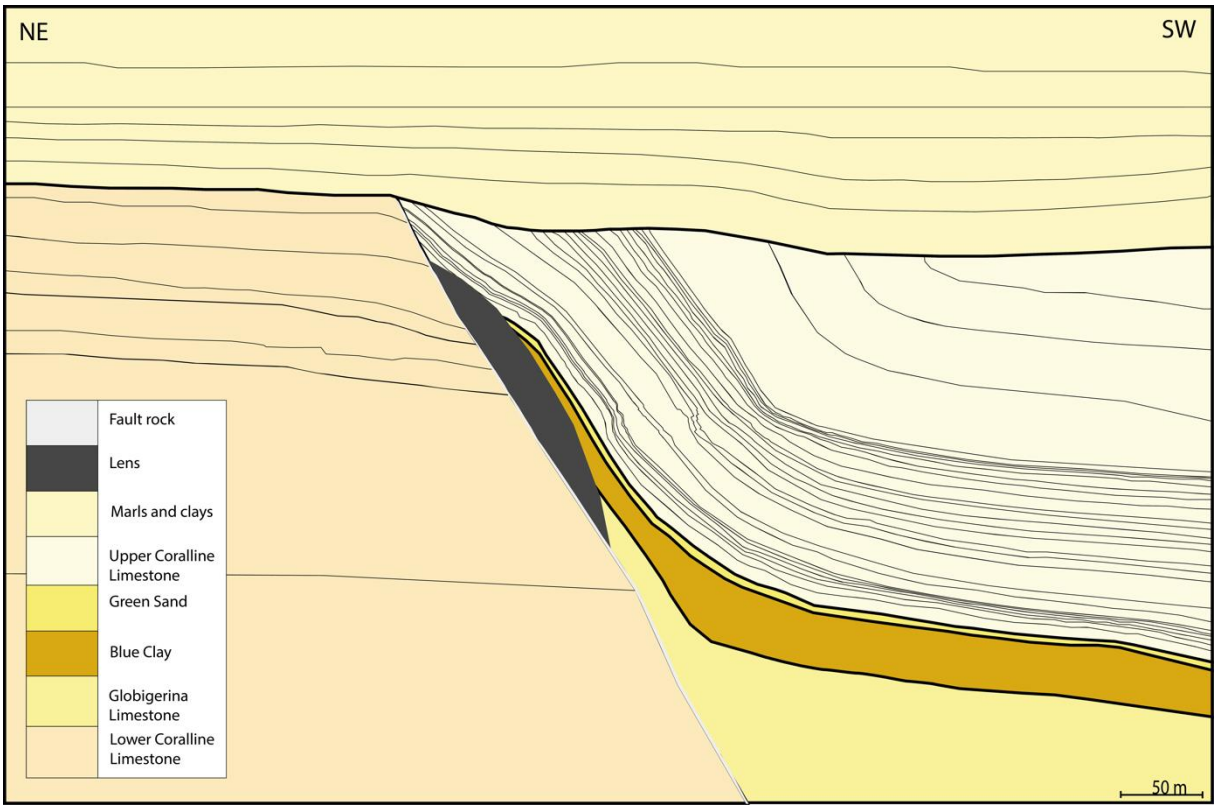

Fig. A 8: 2D Geological model of Locality 2 including a conceptual fault rock and a lens.

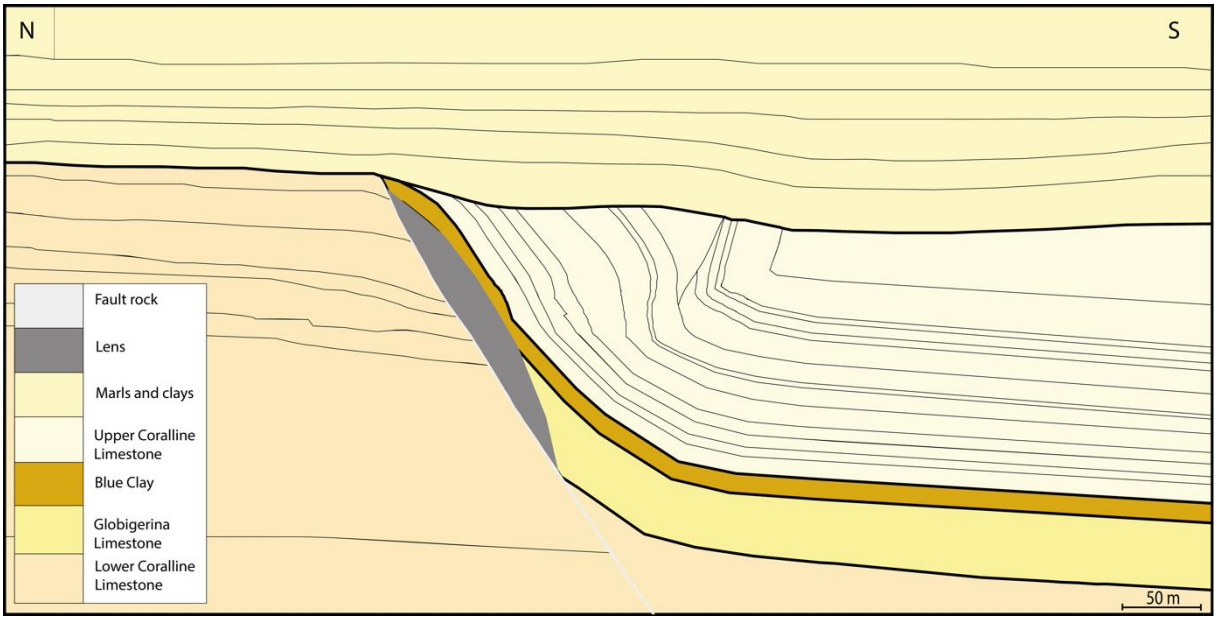

Fig. A 9: 2D Geological model of Locality 3 including a conceptual fault rock and a lens.

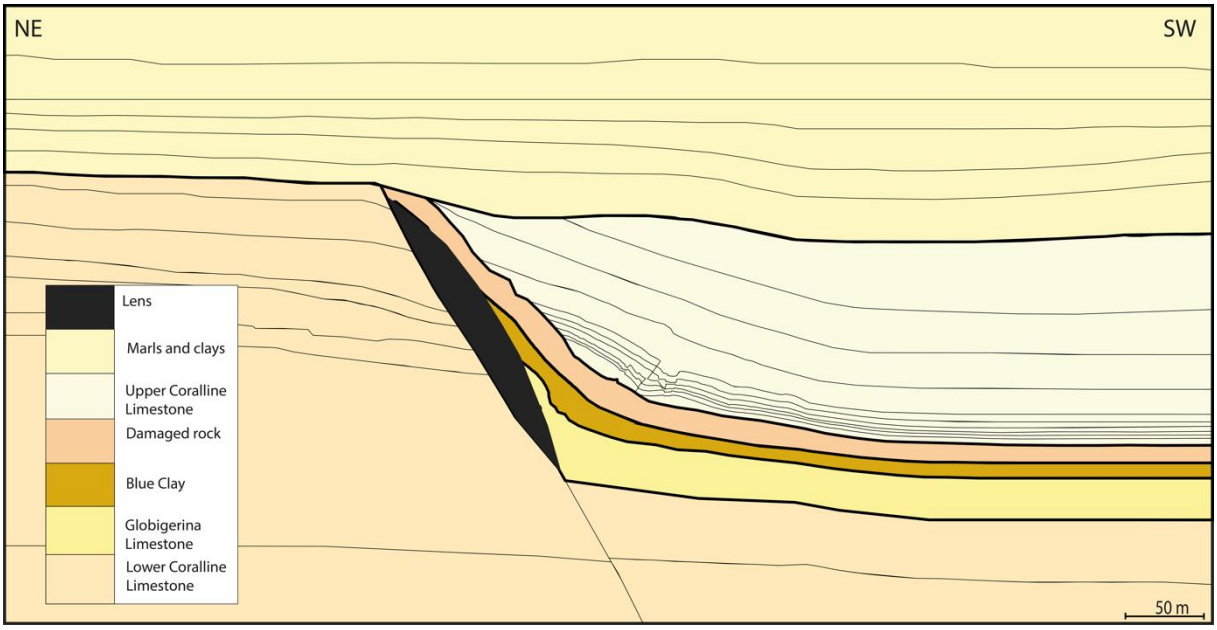

Fig. A 10: 2D Geological model of Locality 1 including a conceptual lens (65 m thick).

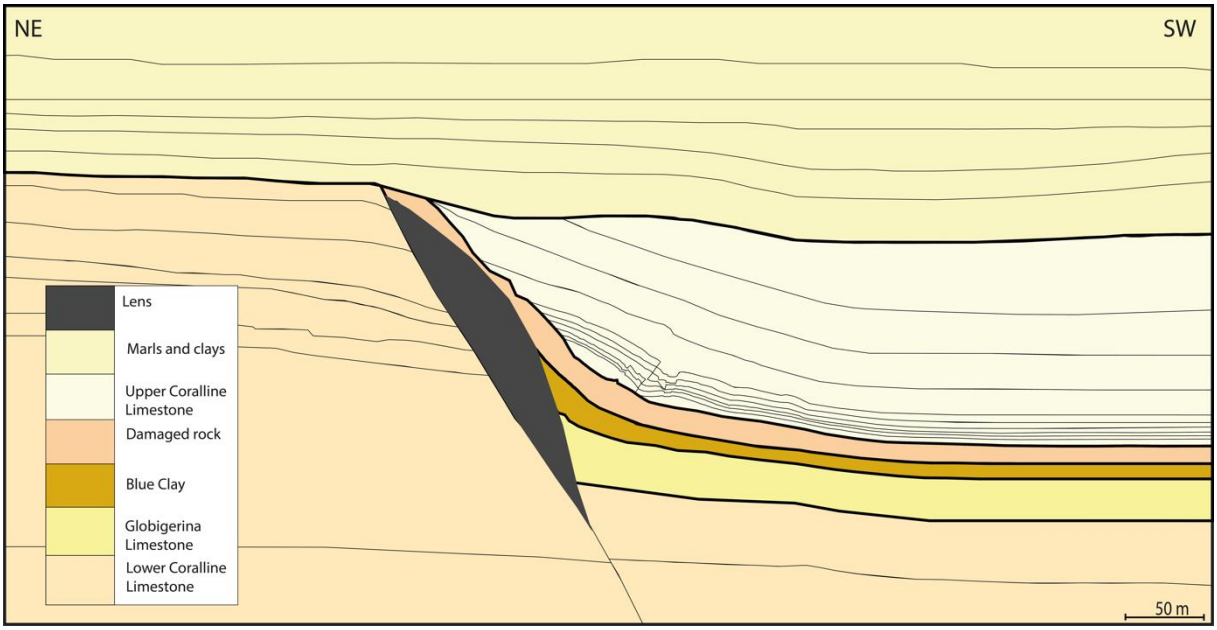

Fig. A 11: 2D Geological model of Locality 1 including a conceptual lens (100 m thick).

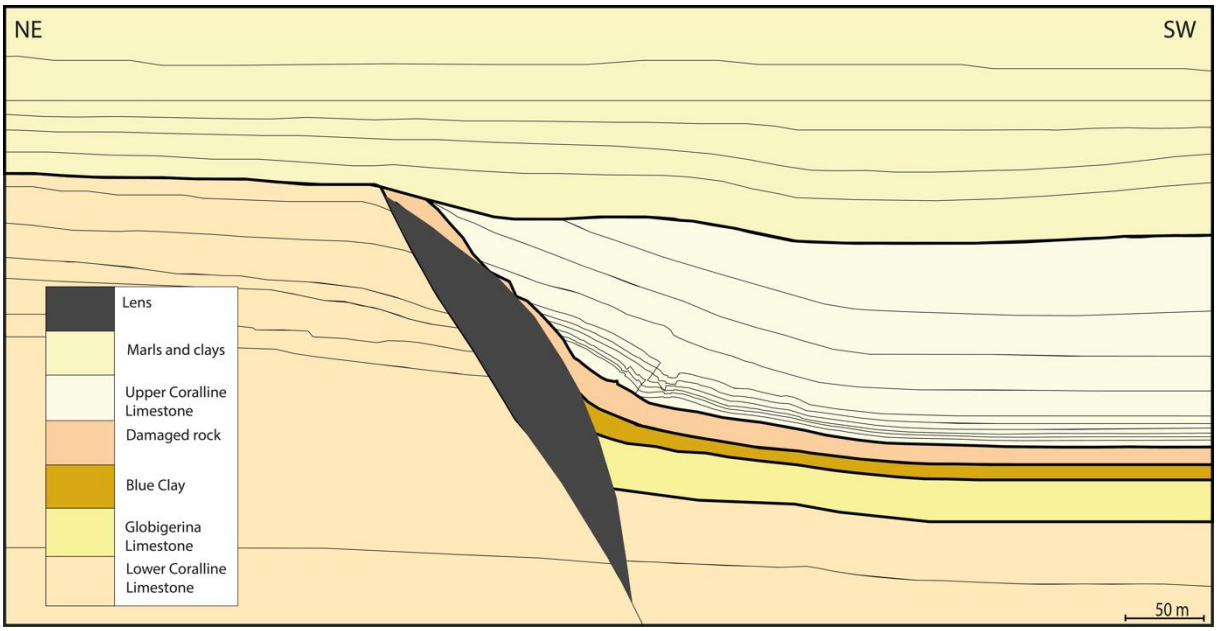

Fig. A 12: 2D Geological model of Locality 1 including a conceptual lens (130m thick).

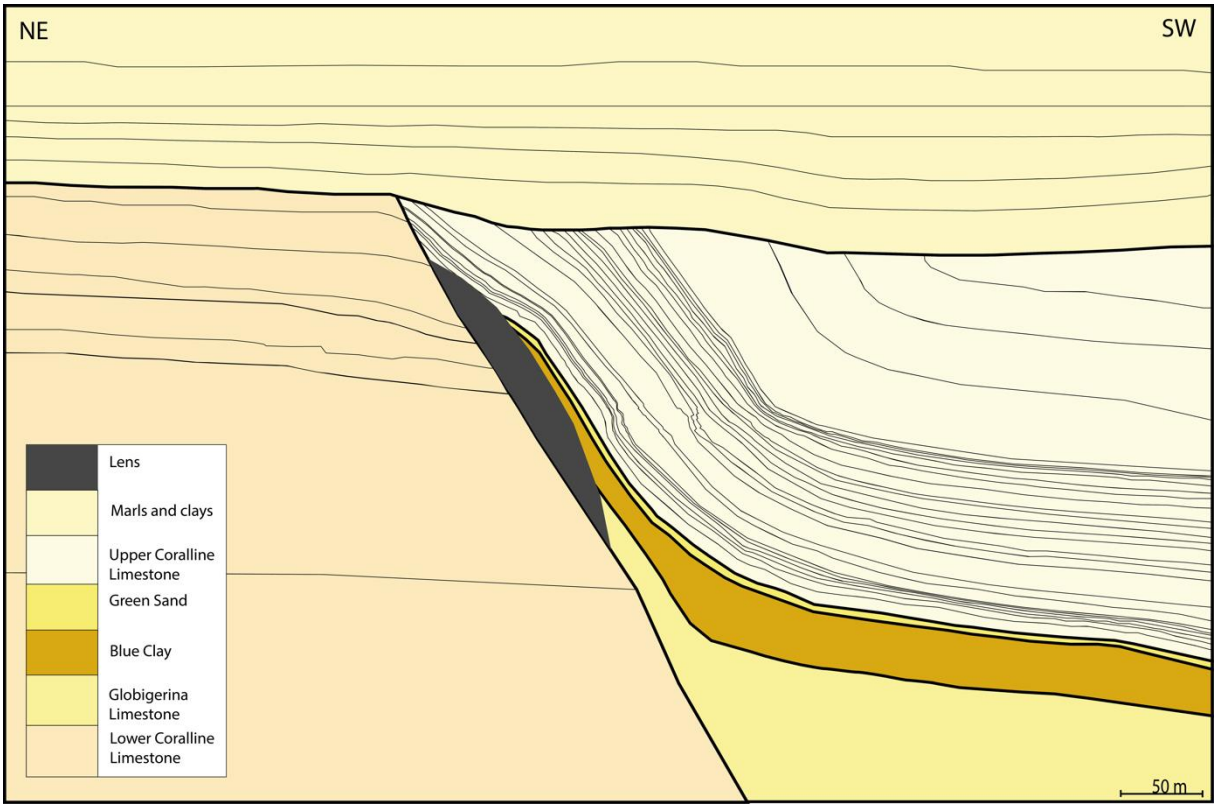

Fig. A 13: 2D Geological model of Locality 2 including a conceptual lens (65 m thick).

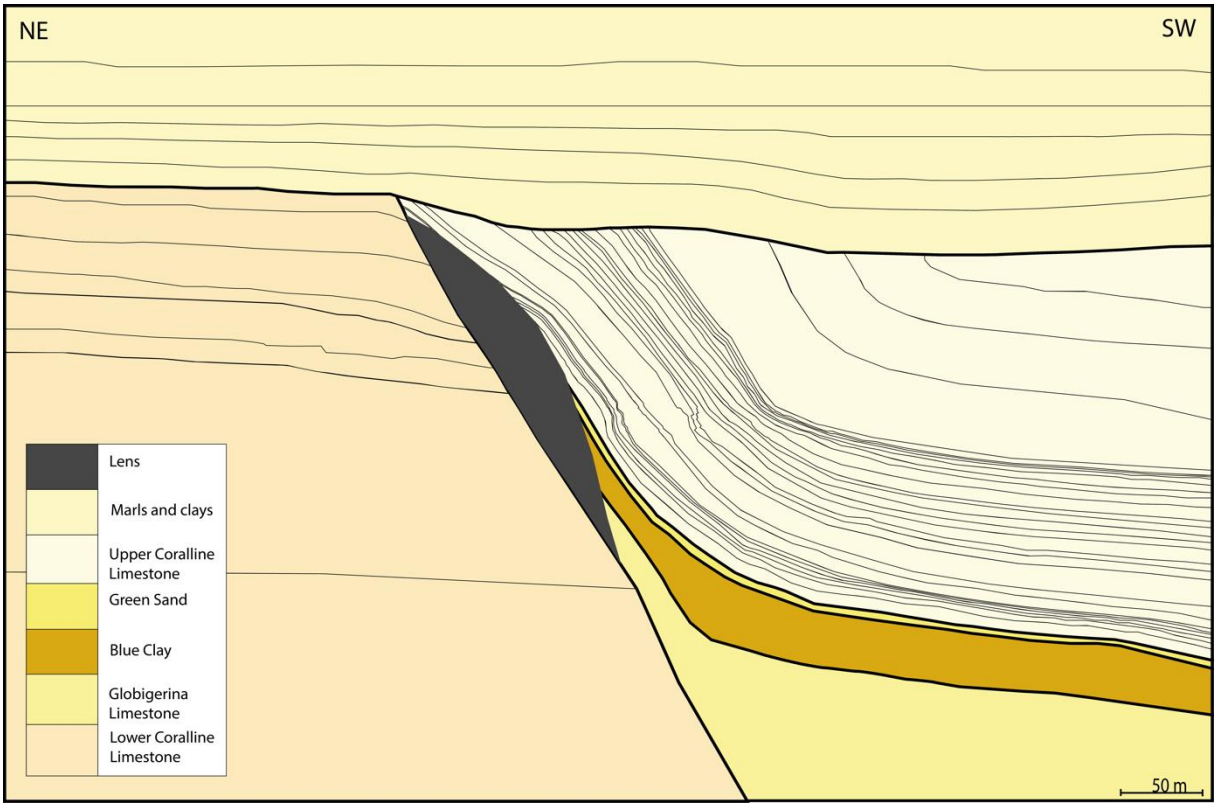

Fig. A 14: 2D Geological model of Locality 2 including a conceptual lens (100 m thick).

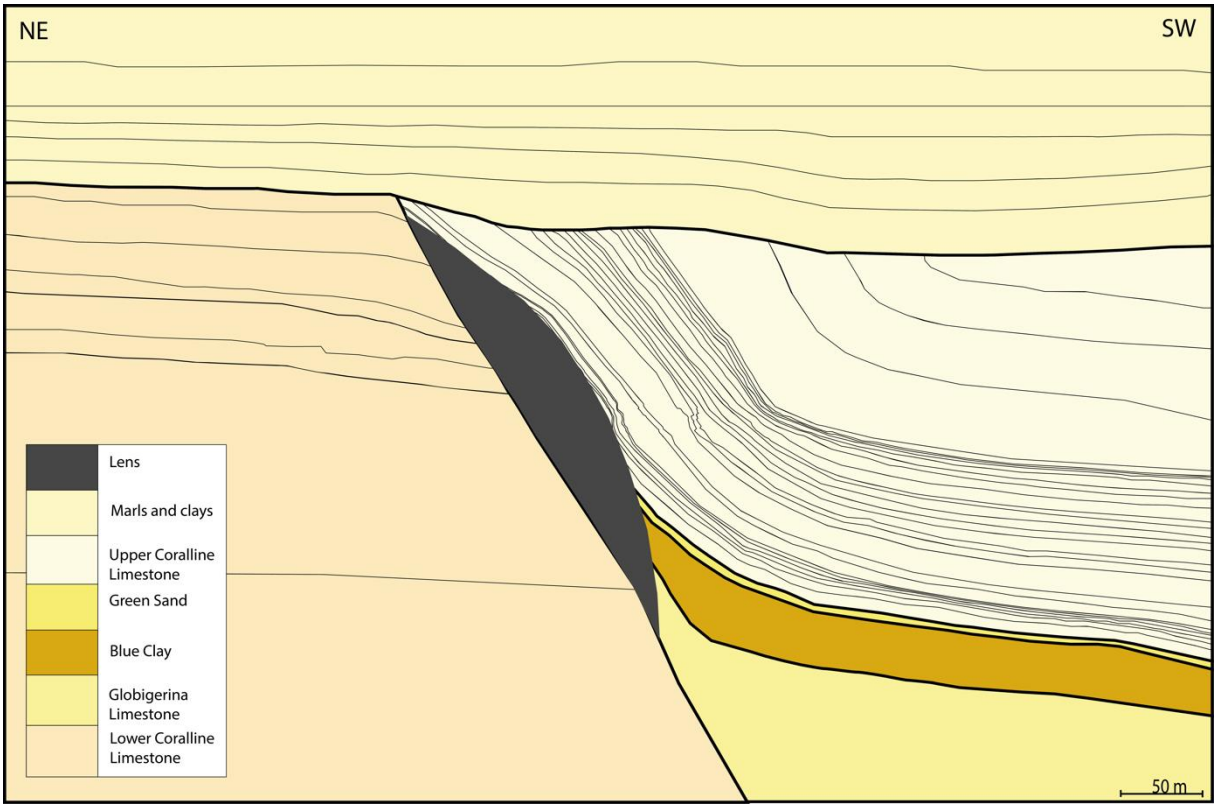

Fig. A 15: 2D Geological model of Locality 2 including a conceptual lens (130 m thick).

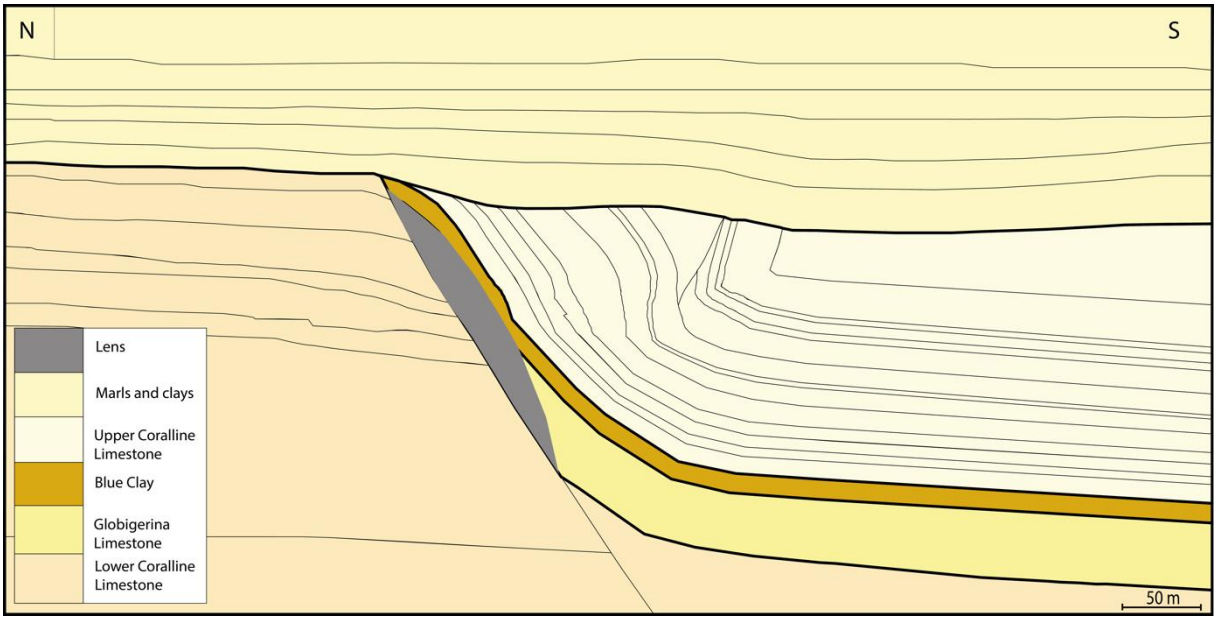

Fig. A 16: 2D Geological model of Locality 3 including a conceptual lens (65 m thick).

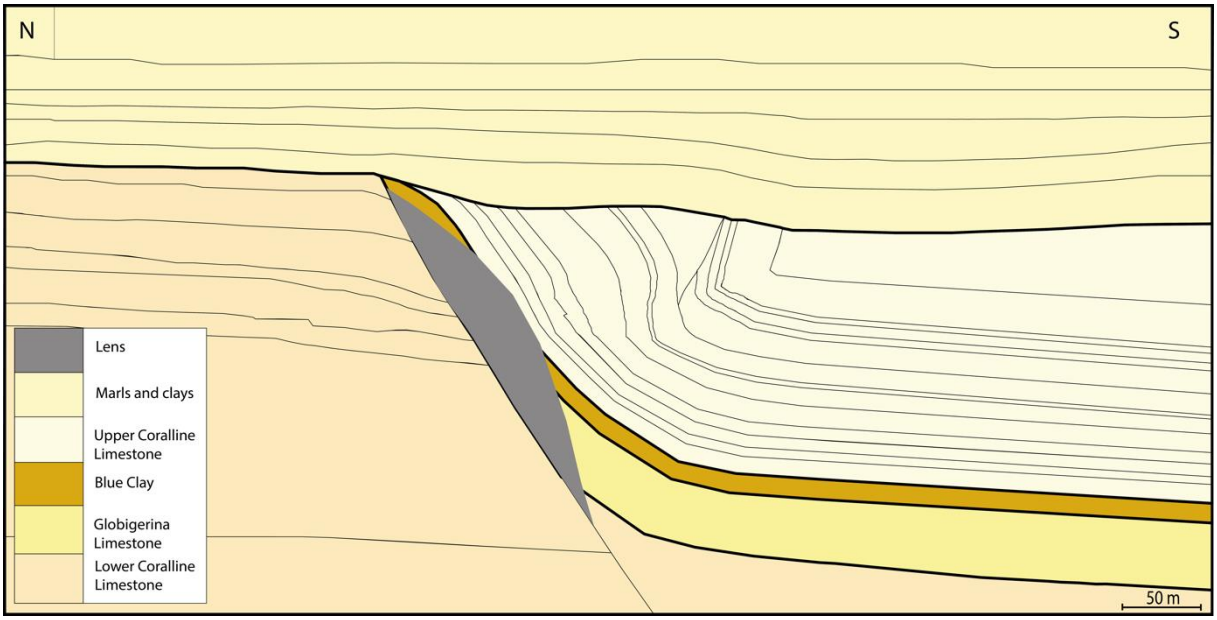

Fig. A 17: 2D Geological model of Locality 3 including a conceptual lens (100 m thick).

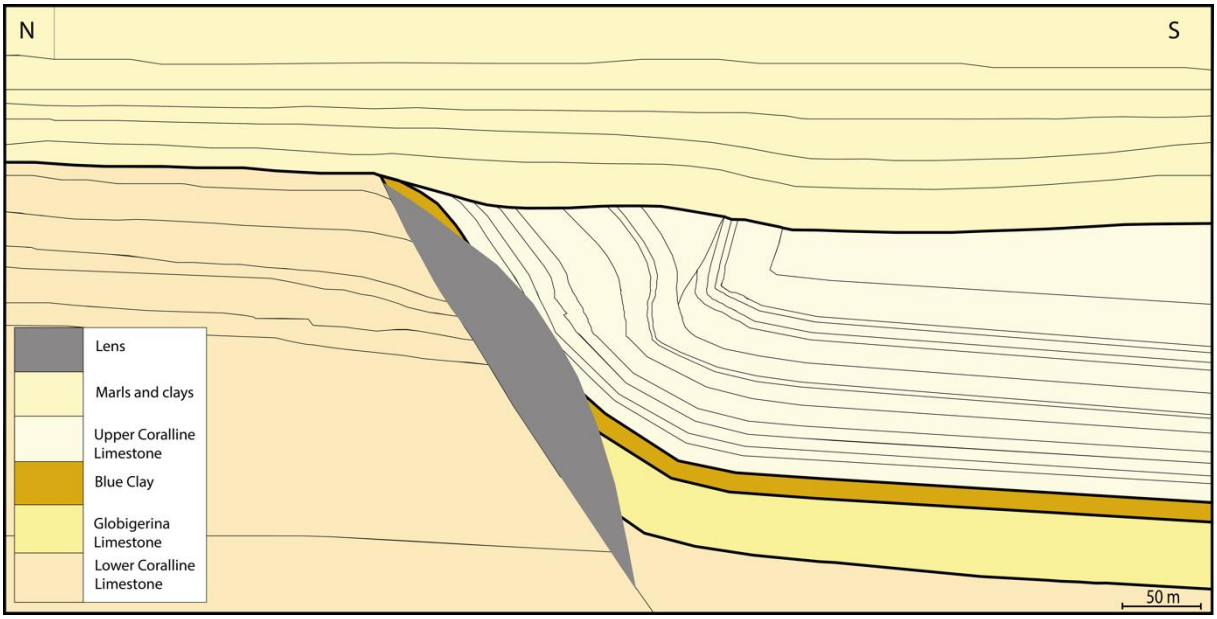

Fig. A 18: 2D Geological model of Locality 3 including a conceptual lens (130 m thick).

APPENDIX II: SYNTHETIC SEISMIC IMAGES

Segmented fault

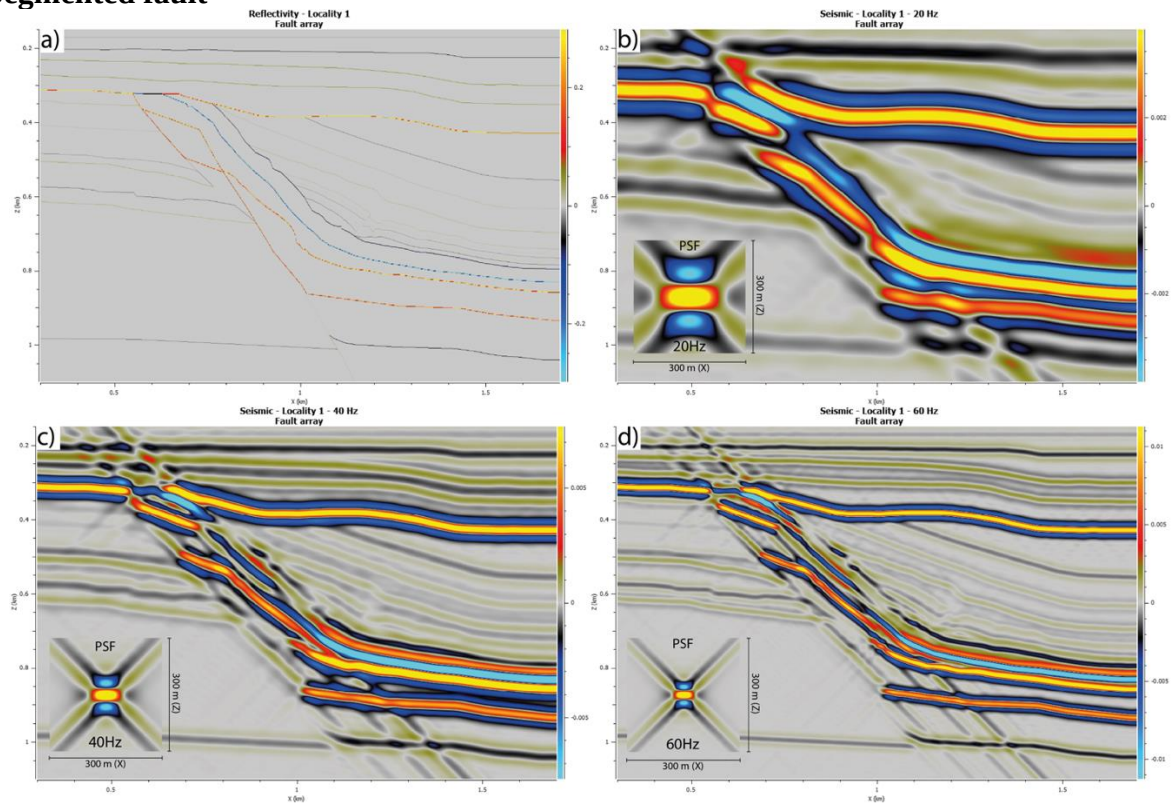

Fig. B 1: Seismic images of Locality 1 modelled with a segmented fault. a) Reflectivity model. b) 20 Hz seismic image. c) 40 Hz seismic image. d) 60 Hz seismic image.

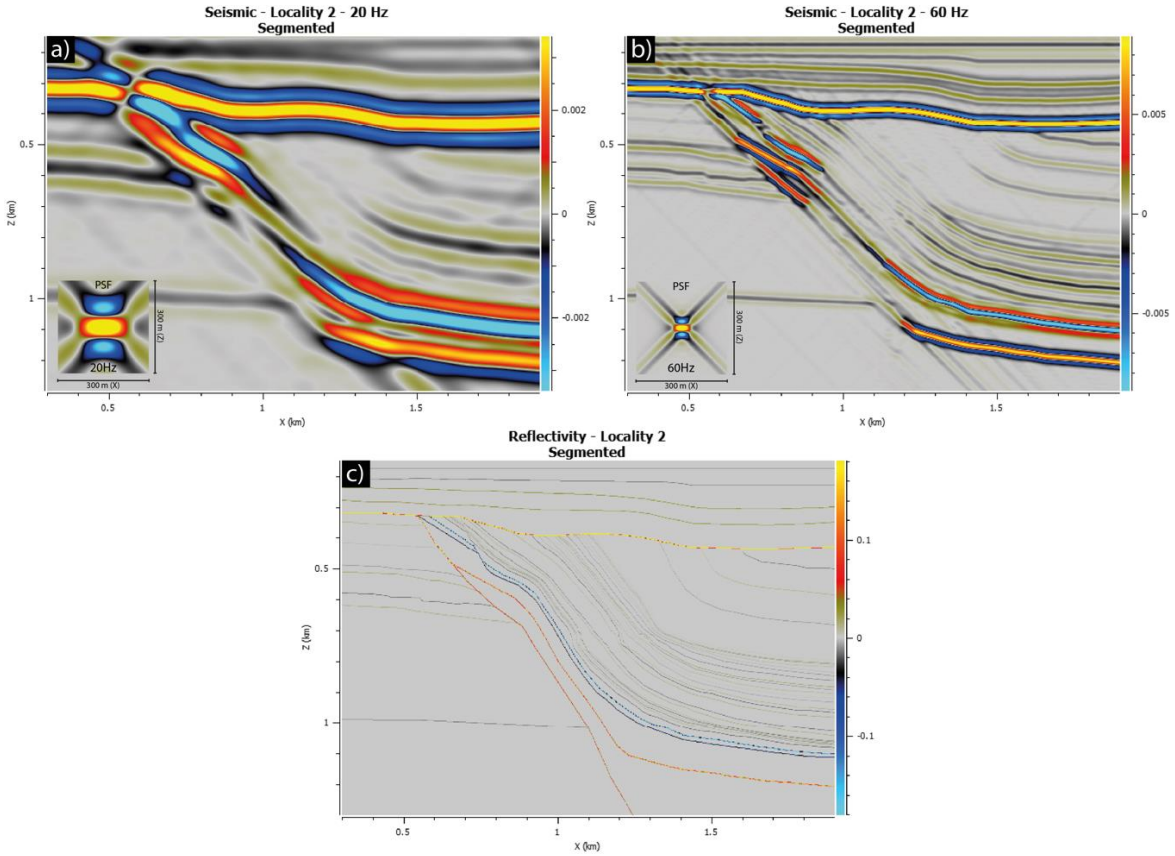

Fig. B 2: Seismic images of Locality 2 modelled with a segmented fault. a) 20 Hz seismic image. b) 60 Hz seismic image. c) Reflectivity model.

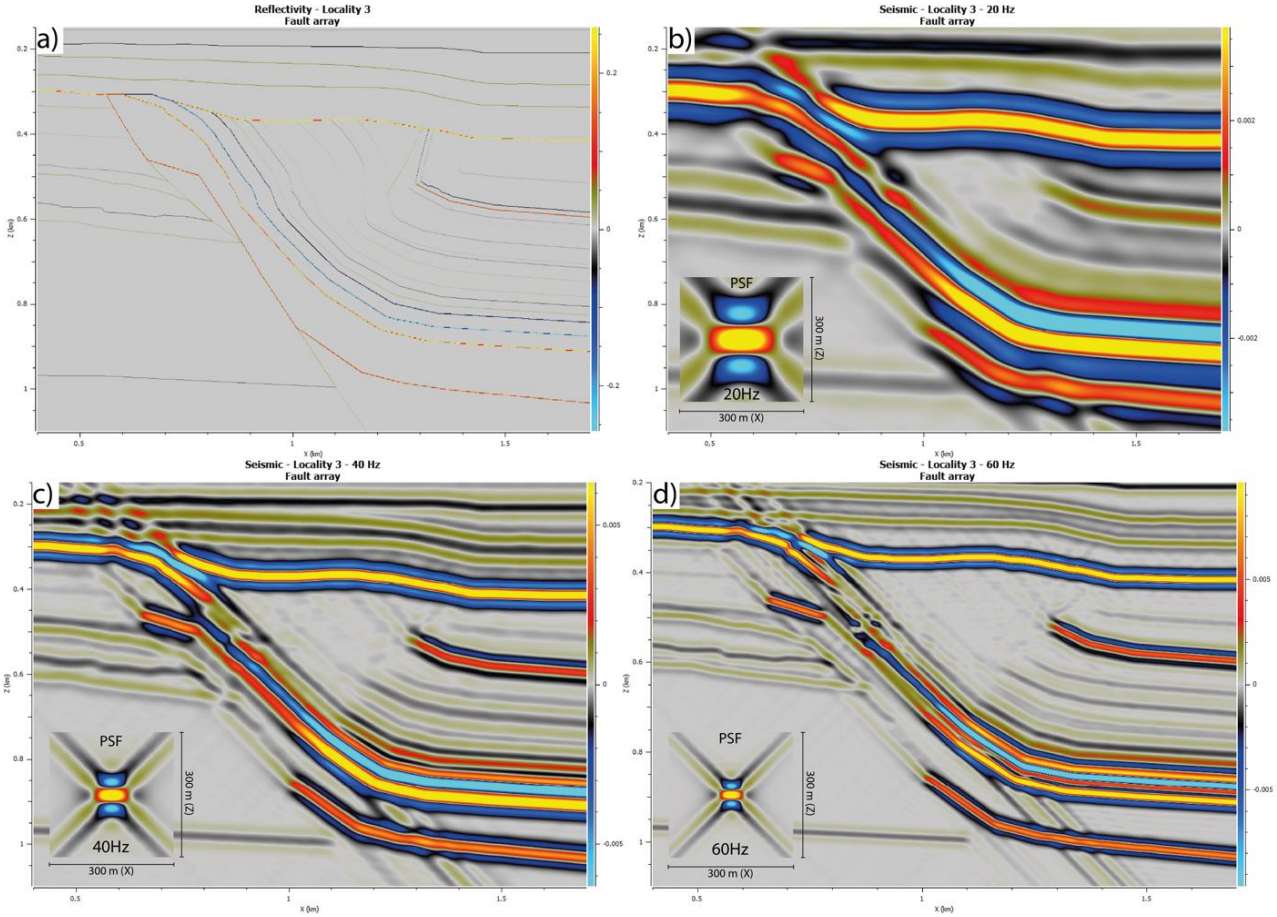

Fig. B 3: Seismic images of Locality 3 modelled with a segmented fault. a) Reflectivity model. b) 20 Hz seismic image. c) 40 Hz seismic image. d) 60 Hz seismic image.

Overlapping fault segments

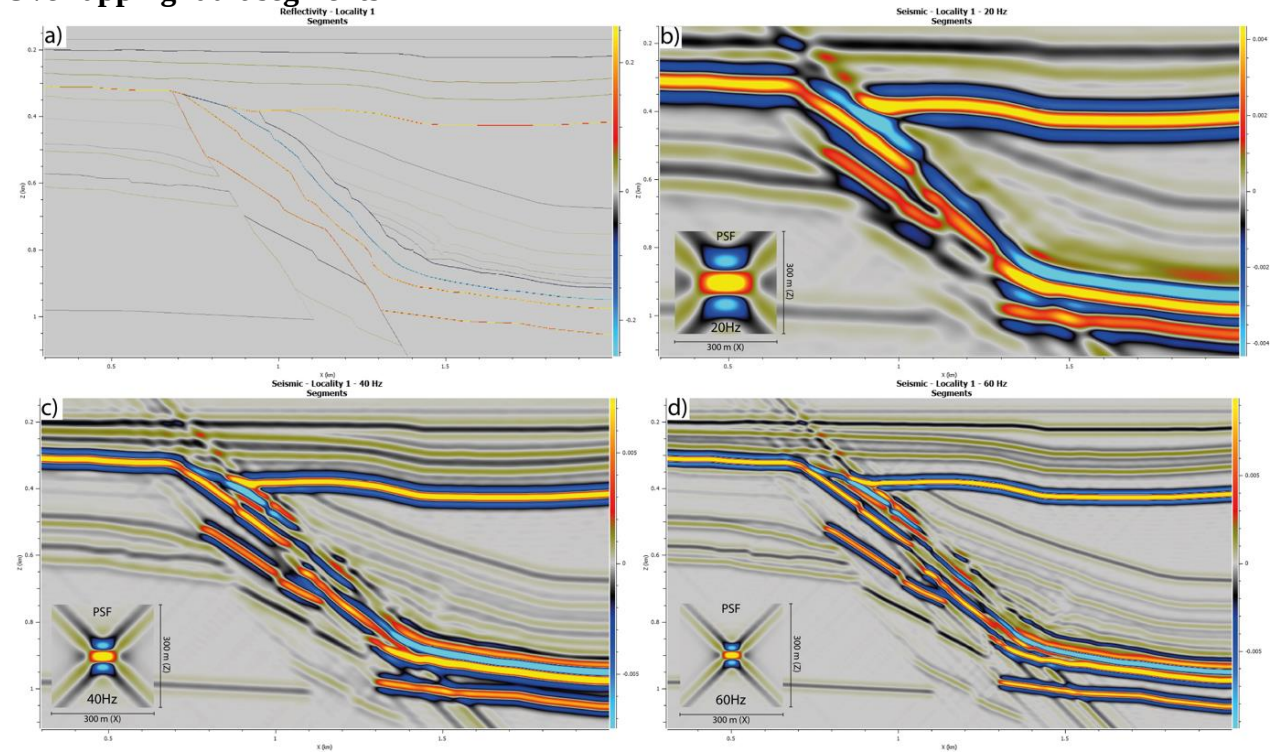

Fig. B 4: Seismic images of Locality 1 modelled with overlapping fault segments. a) Reflectivity model. b) 20 Hz seismic image. c) 40 Hz seismic image. d) 60 Hz seismic image.

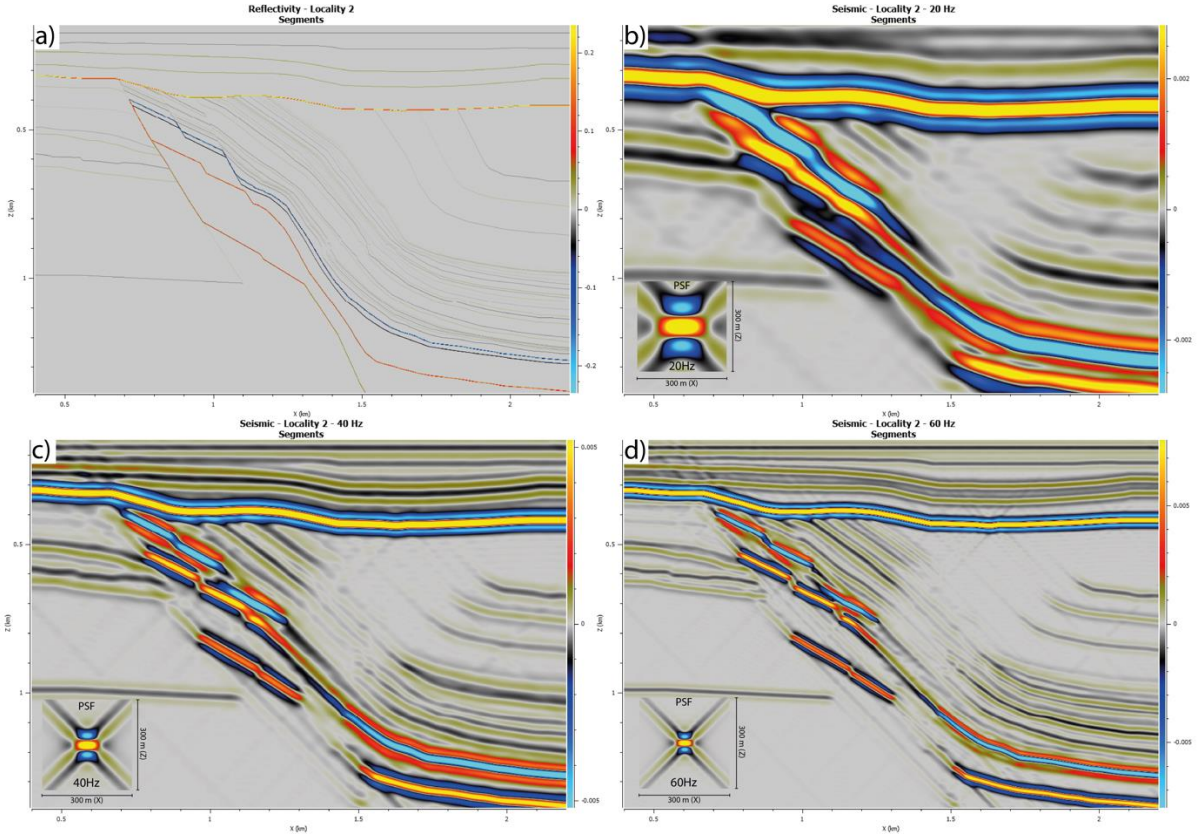

Fig. B 5: Seismic images of Locality 2 modelled with overlapping fault segments. a) Reflectivity model. b) 20 Hz seismic image. c) 40 Hz seismic image. d) 60 Hz seismic image.

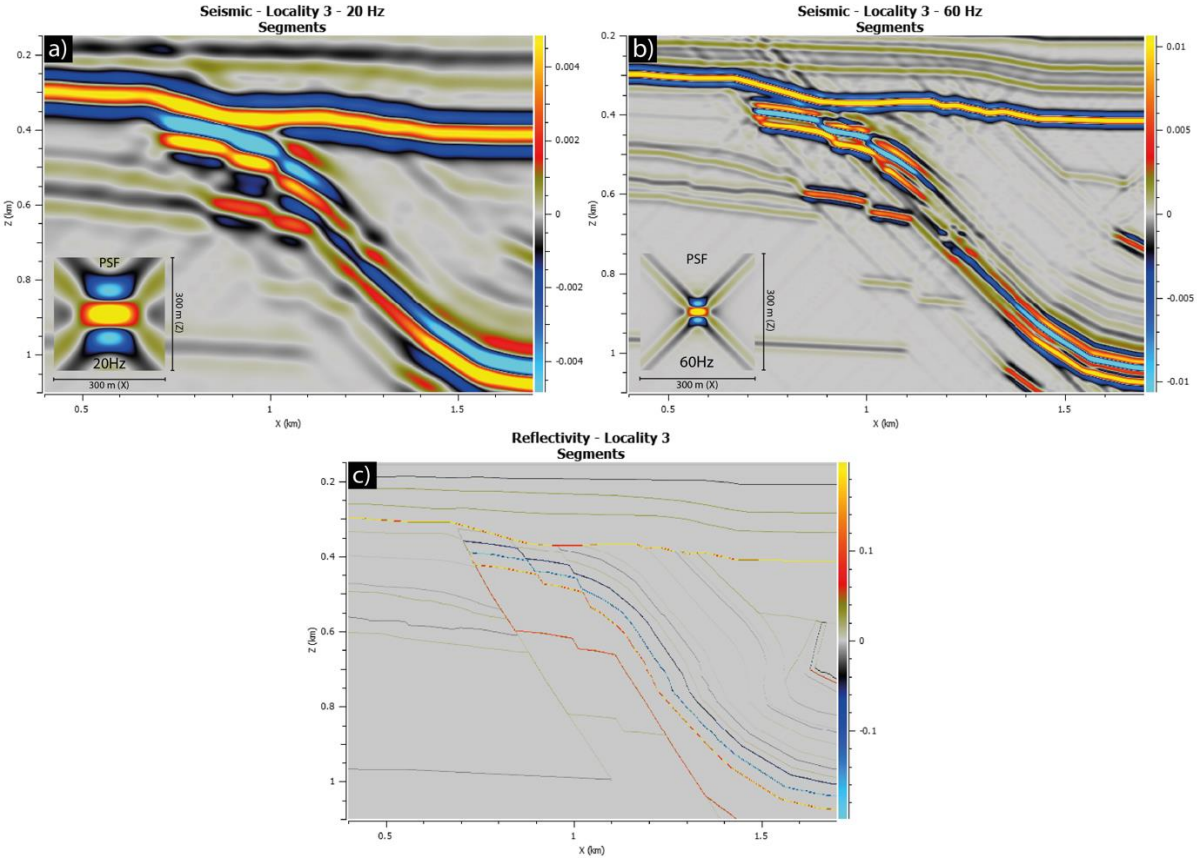

Fig. B 6: Seismic images of Locality 3 modelled with overlapping fault segments. a) 20 Hz seismic image. b) 60 Hz seismic image. c) Reflectivity model.

Fault rock

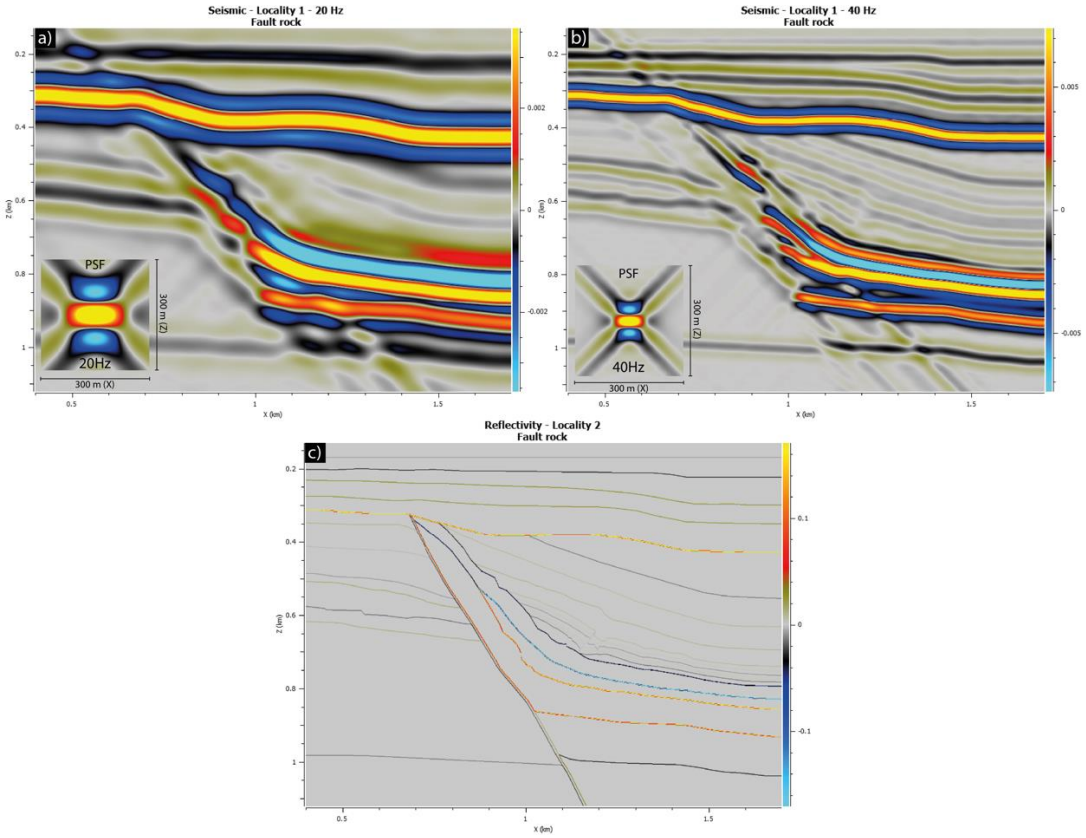

Fig. B 7: Seismic images of Locality 1 modelled with a fault rock and a GL lens. a) 20 Hz seismic image. b) 60 Hz seismic image. c) Reflectivity model.

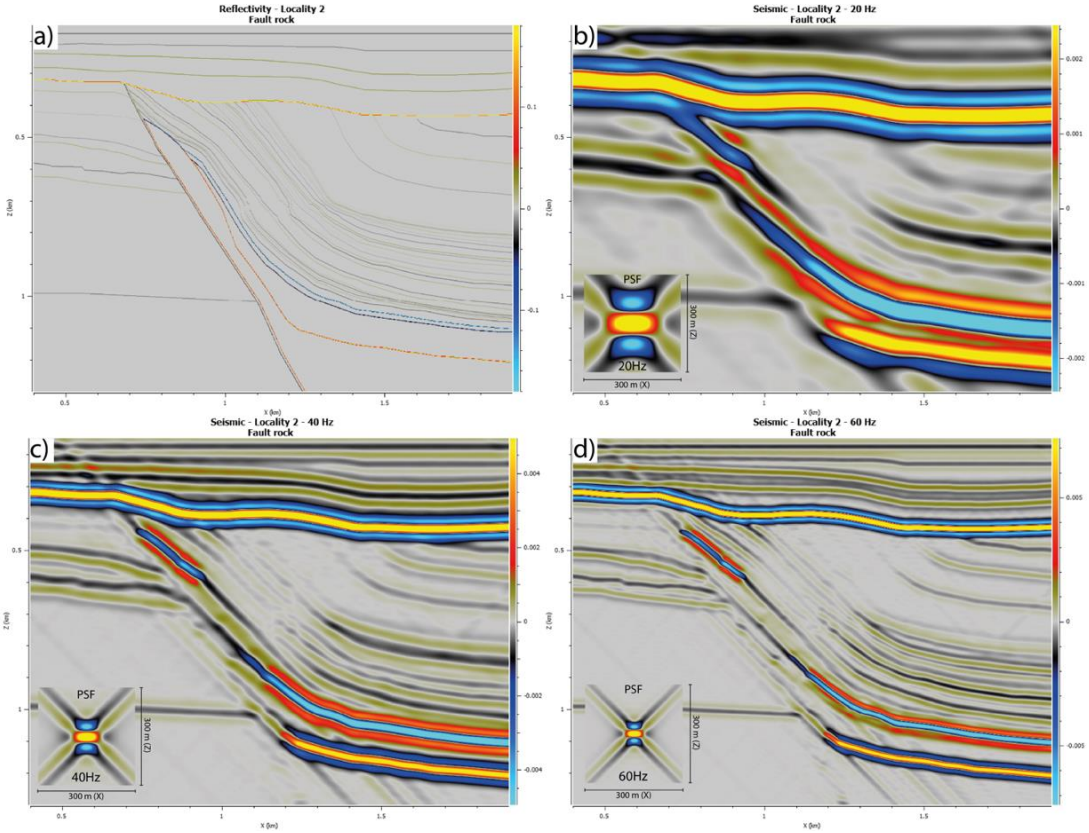

Fig. B 8: Seismic images of Locality 2 modelled with a fault rock and a GL lens. a) Reflectivity model. b) 20 Hz seismic image. c) 40 Hz seismic image. d) 60 Hz seismic image.

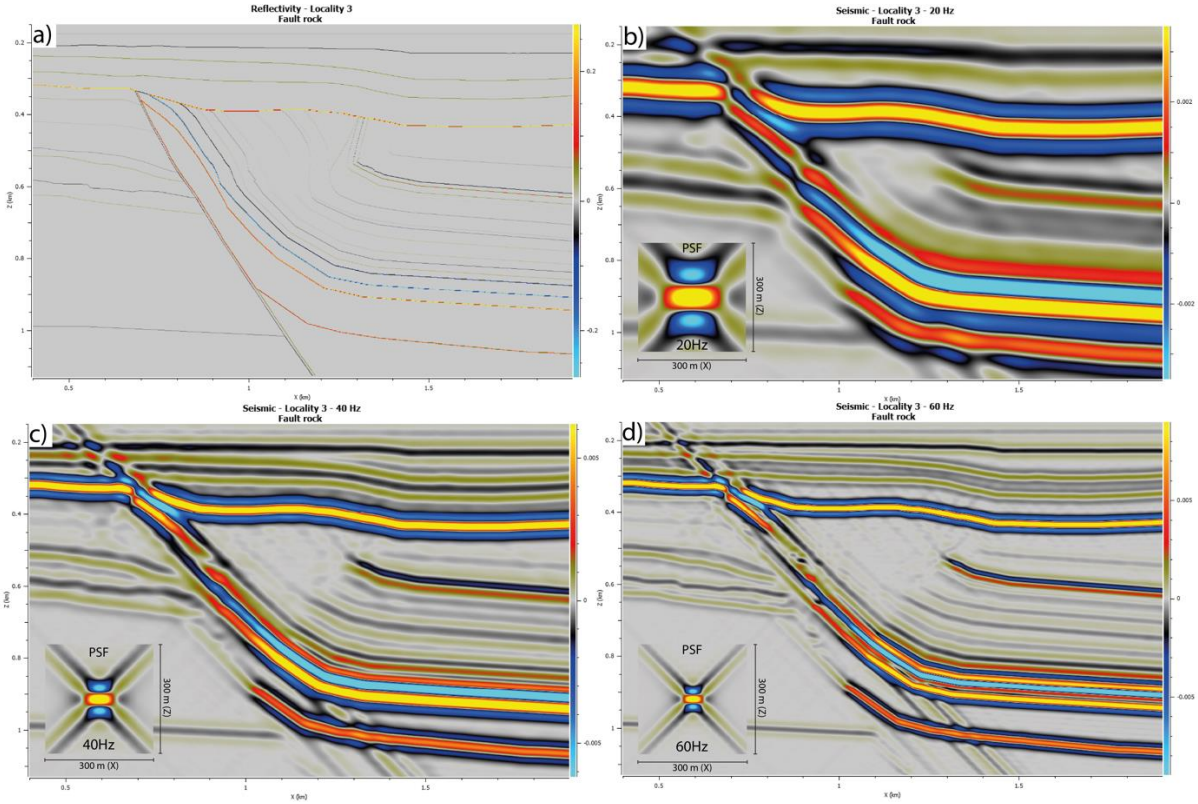

Fig. B 9: Seismic images of Locality 1 modelled with overlapping fault segments. a) Reflectivity model. b) 20 Hz seismic image. c) 40 Hz seismic image. d) 60 Hz seismic image.

GL lens

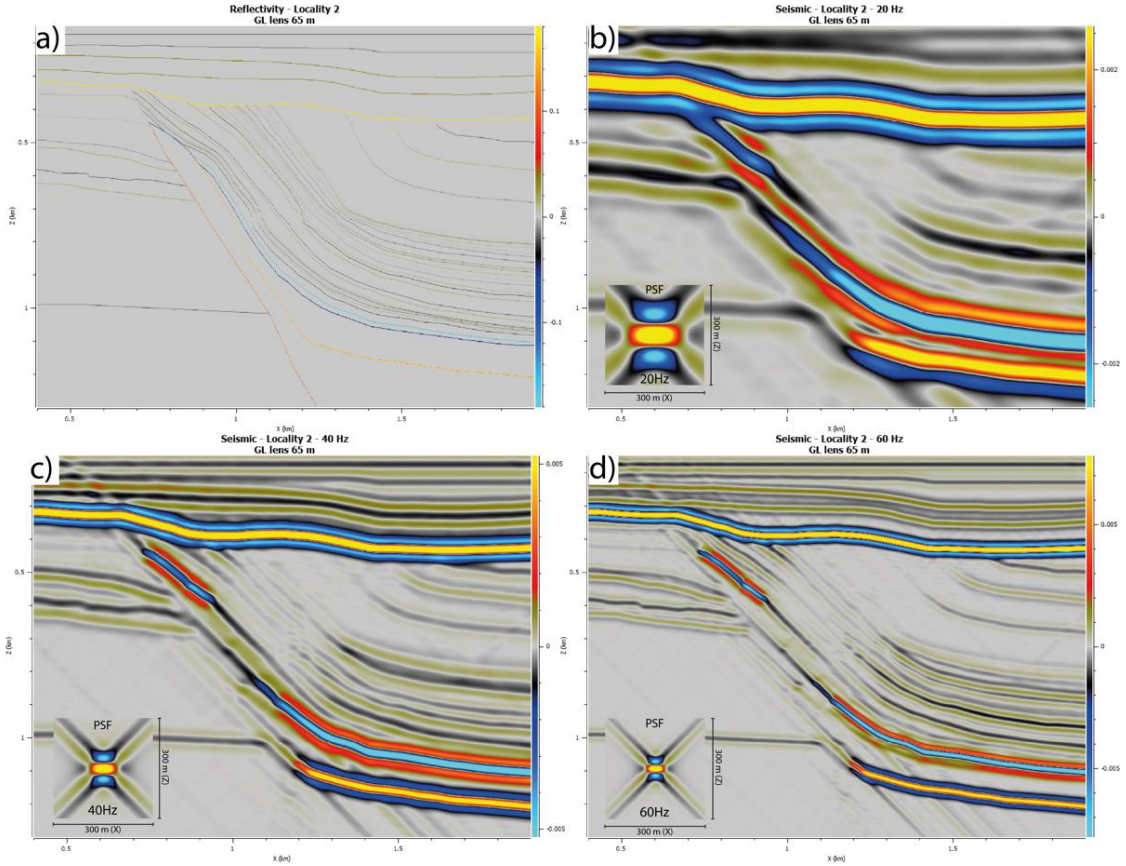

Fig. B 10: Seismic images of Locality 2 modelled with a 65 m thick GL lens. a) Reflectivity model. b) 20 Hz seismic image. c) 40 Hz seismic image. d) 60 Hz seismic image.

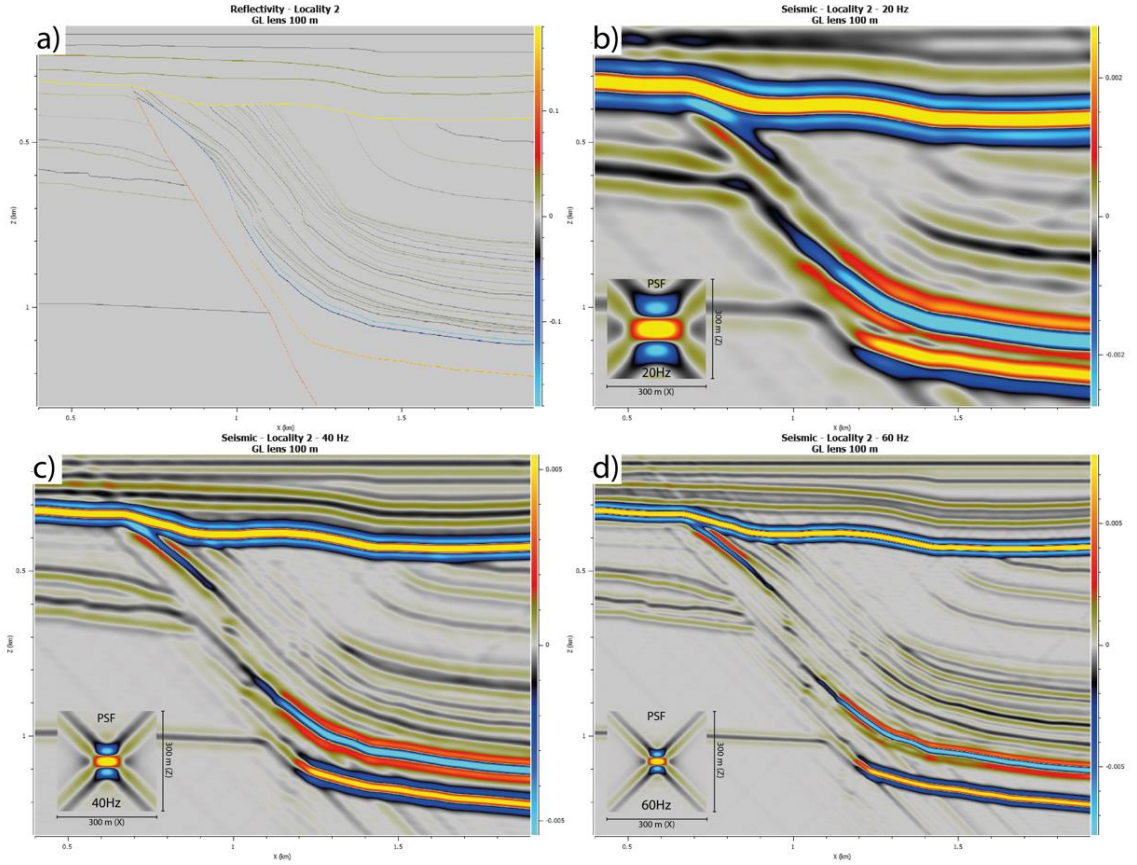

Fig. B 11: Seismic images of Locality 2 modelled with a 100 m thick GL lens. a) Reflectivity model. b) 20 Hz seismic image. c) 40 Hz seismic image. d) 60 Hz seismic image.

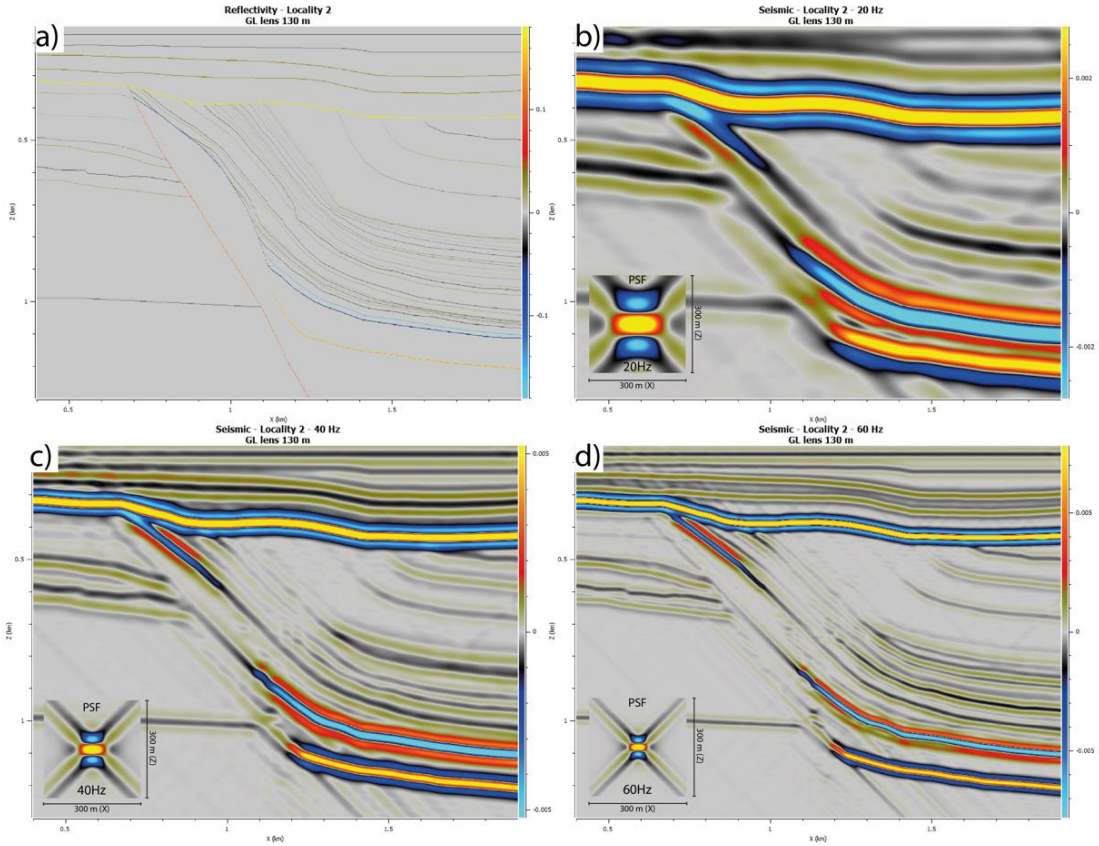

Fig. B 12: Seismic images of Locality 2 modelled with a 130 m thick GL lens. a) Reflectivity model. b) 20 Hz seismic image. c) 40 Hz seismic image. d) 60 Hz seismic image.

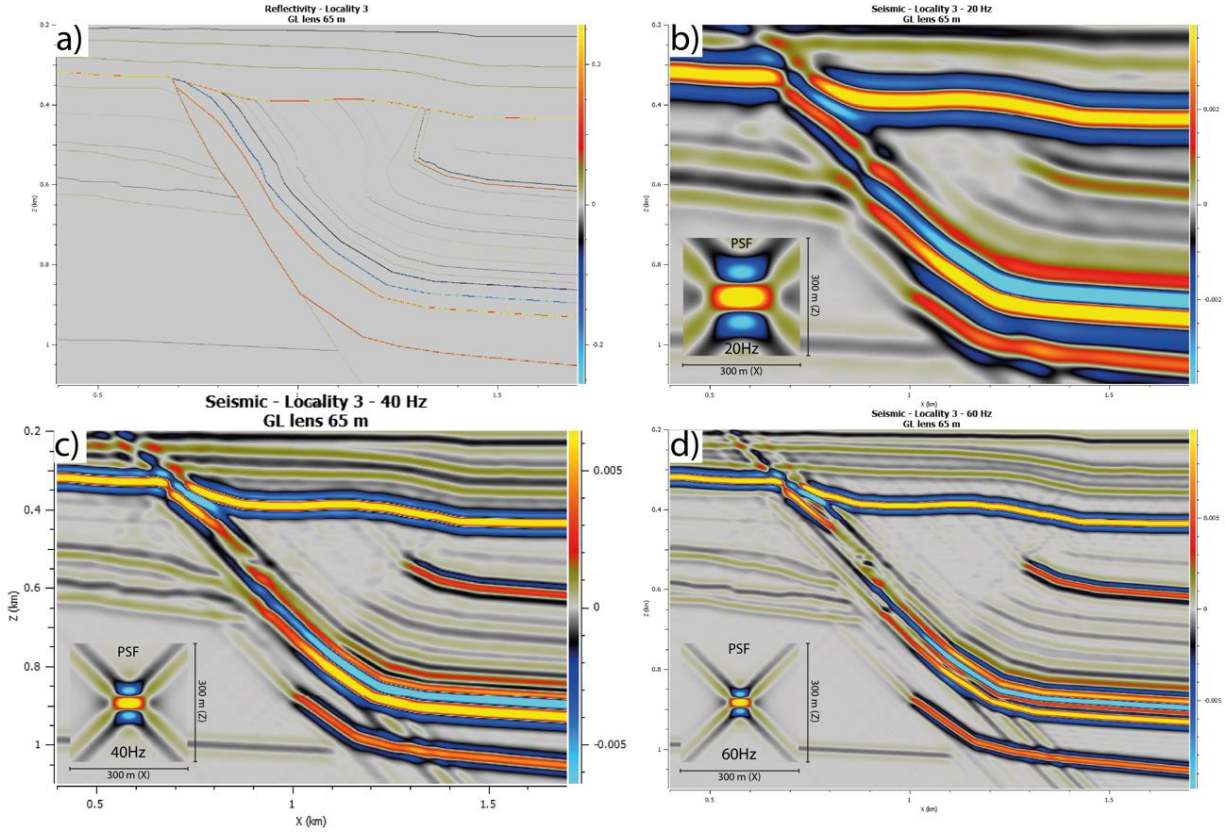

Fig. B 13: Seismic images of Locality 3 modelled with a 65 m thick GL lens. a) Reflectivity model. b) 20 Hz seismic image. c) 40 Hz seismic image. d) 60 Hz seismic image.

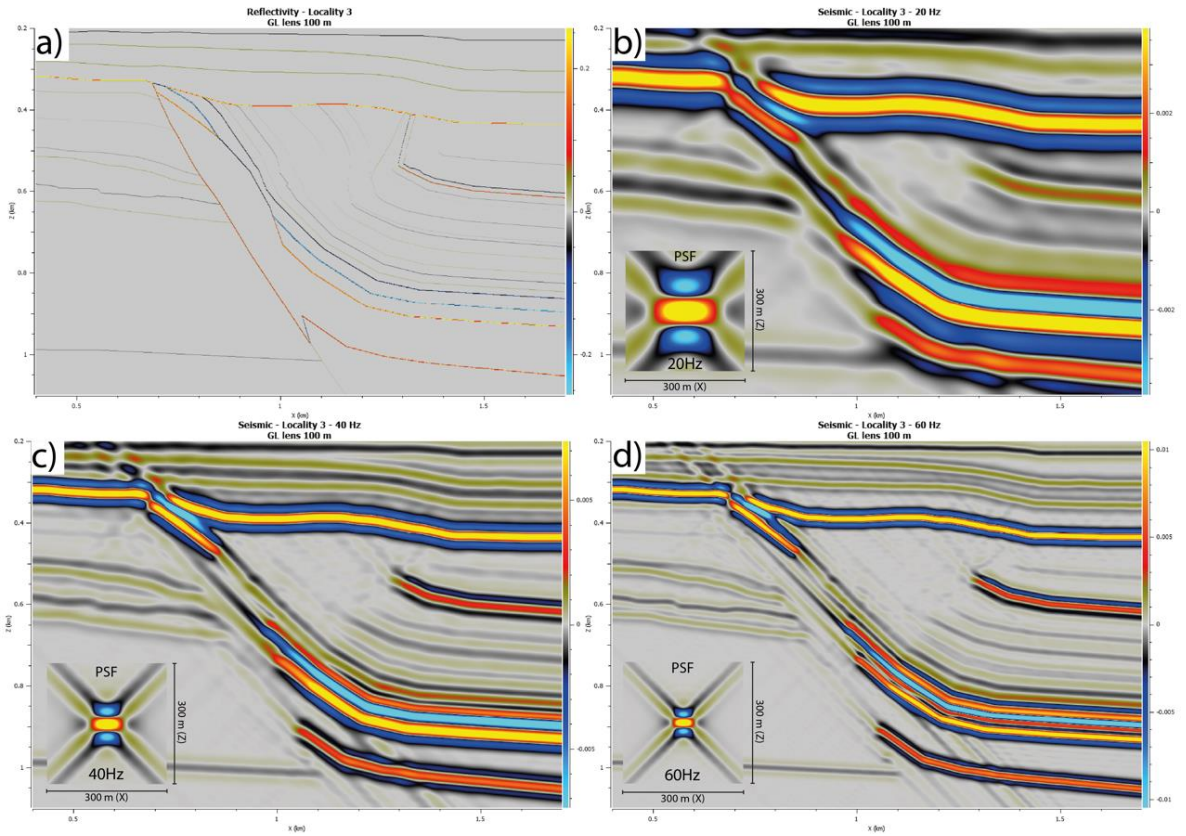

Fig. B 14:Seismic images of Locality 3 modelled with a 100 m thick GL lens. a) Reflectivity model. b) 20 Hz seismic image. c) 40 Hz seismic image. d) 60 Hz seismic image.

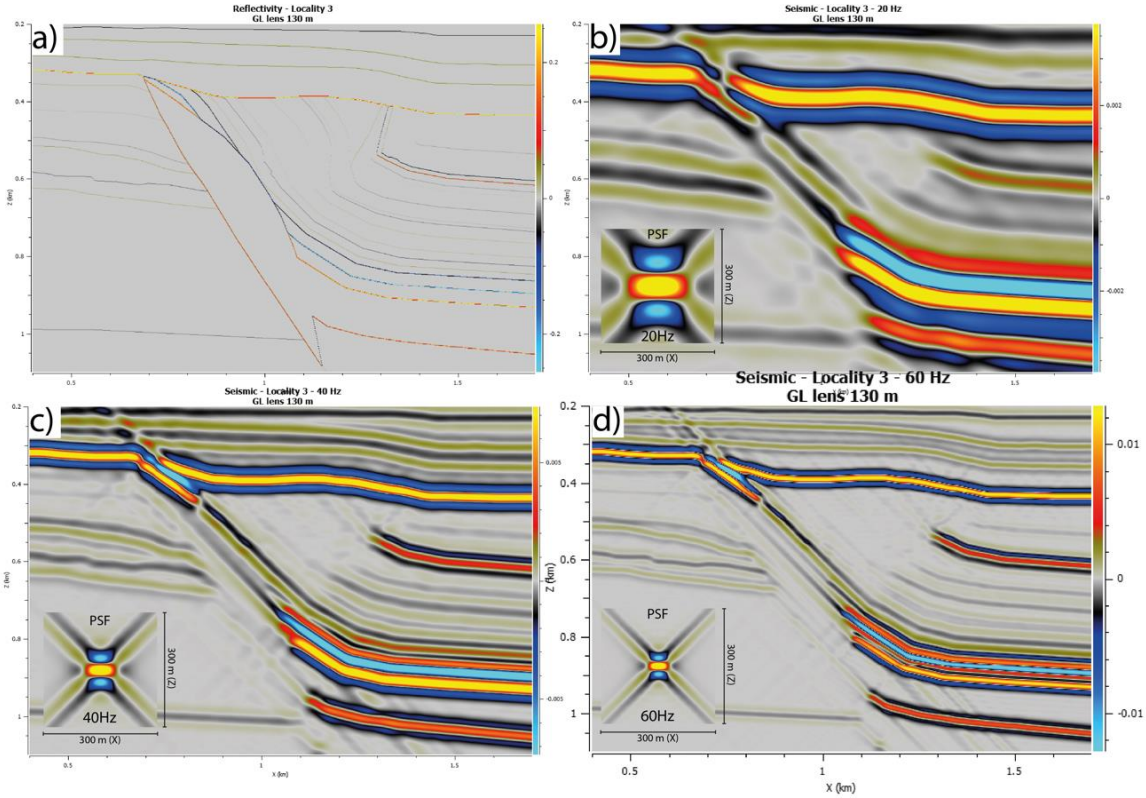

Fig. B 15: Seismic images of Locality 3 modelled with a 130 m thick GL lens. a) Reflectivity model. b) 20 Hz seismic image. c) 40 Hz seismic image. d) 60 Hz seismic image.

LCL lens

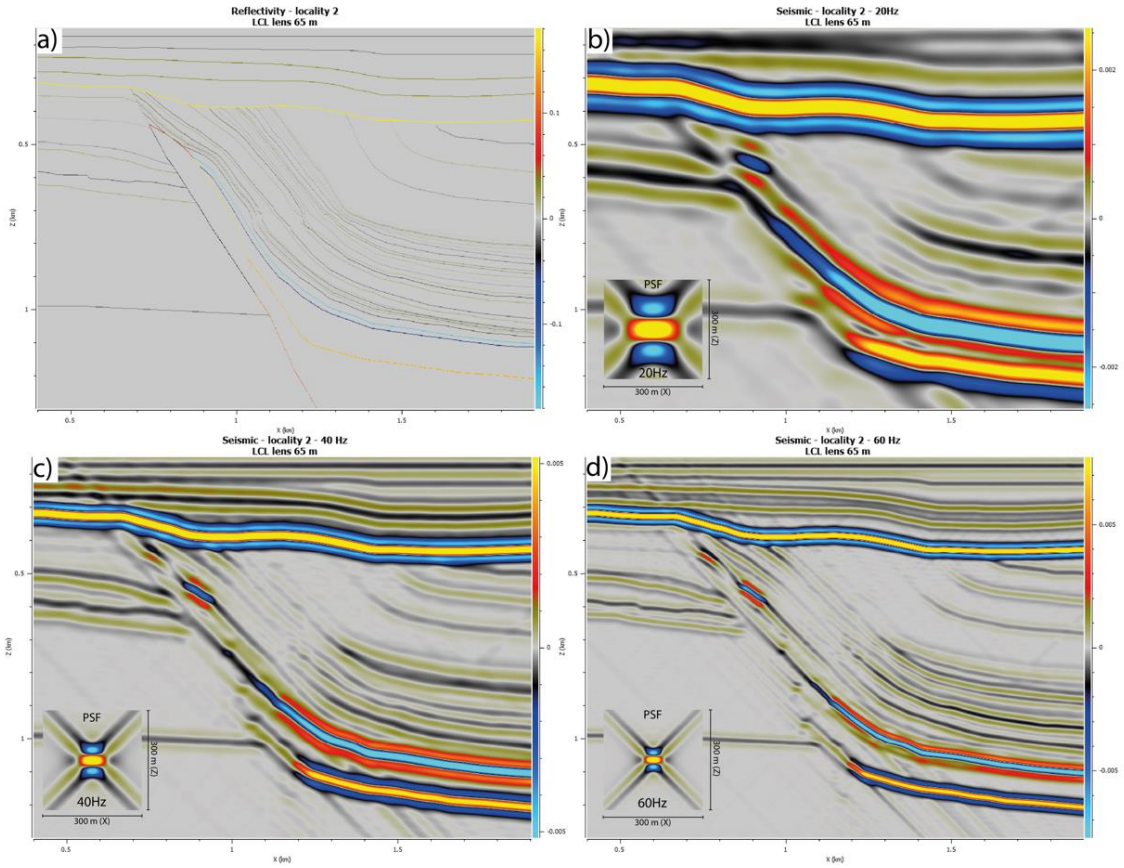

Fig. B 16: Seismic images of Locality 2 modelled with a 65 m thick LCL lens. a) Reflectivity model. b) 20 Hz seismic image. c) 40 Hz seismic image. d) 60 Hz seismic image.

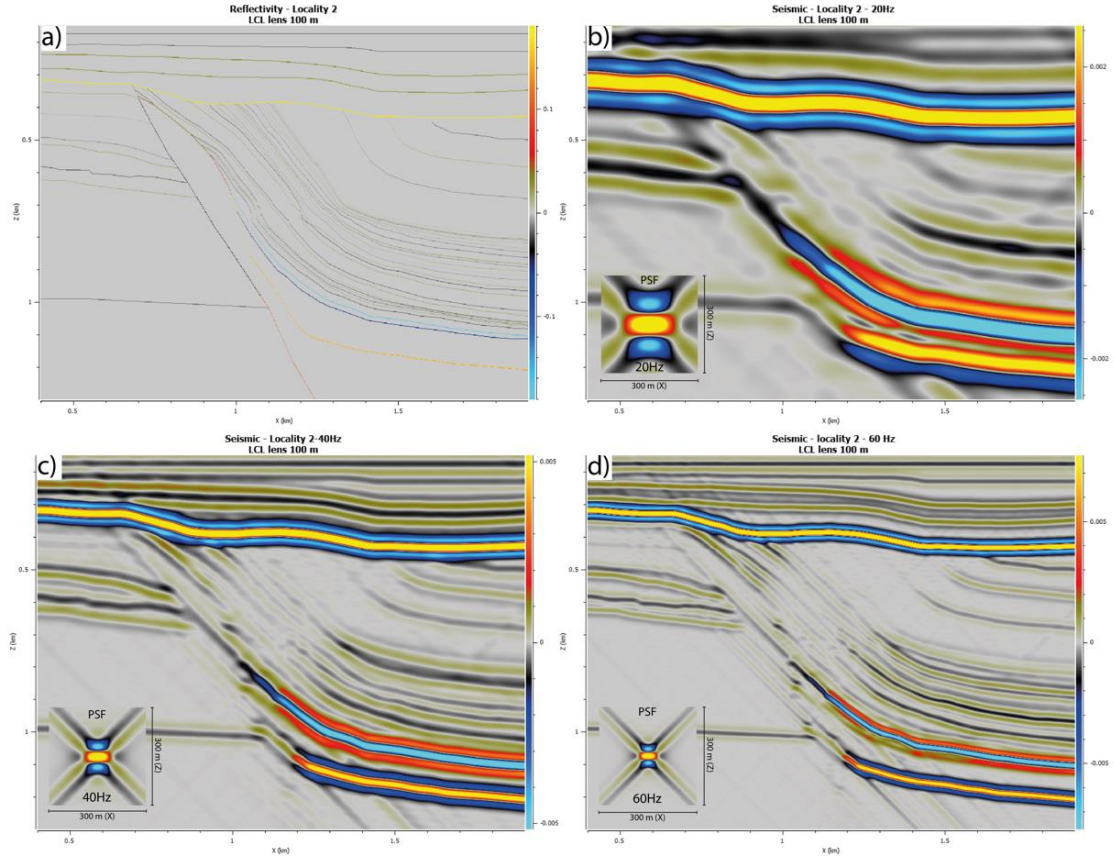

Fig. B 17: Seismic images of Locality 2 modelled with a 100 m thick LCL lens. a) Reflectivity model. b) 20 Hz seismic image. c) 40 Hz seismic image. d) 60 Hz seismic image.

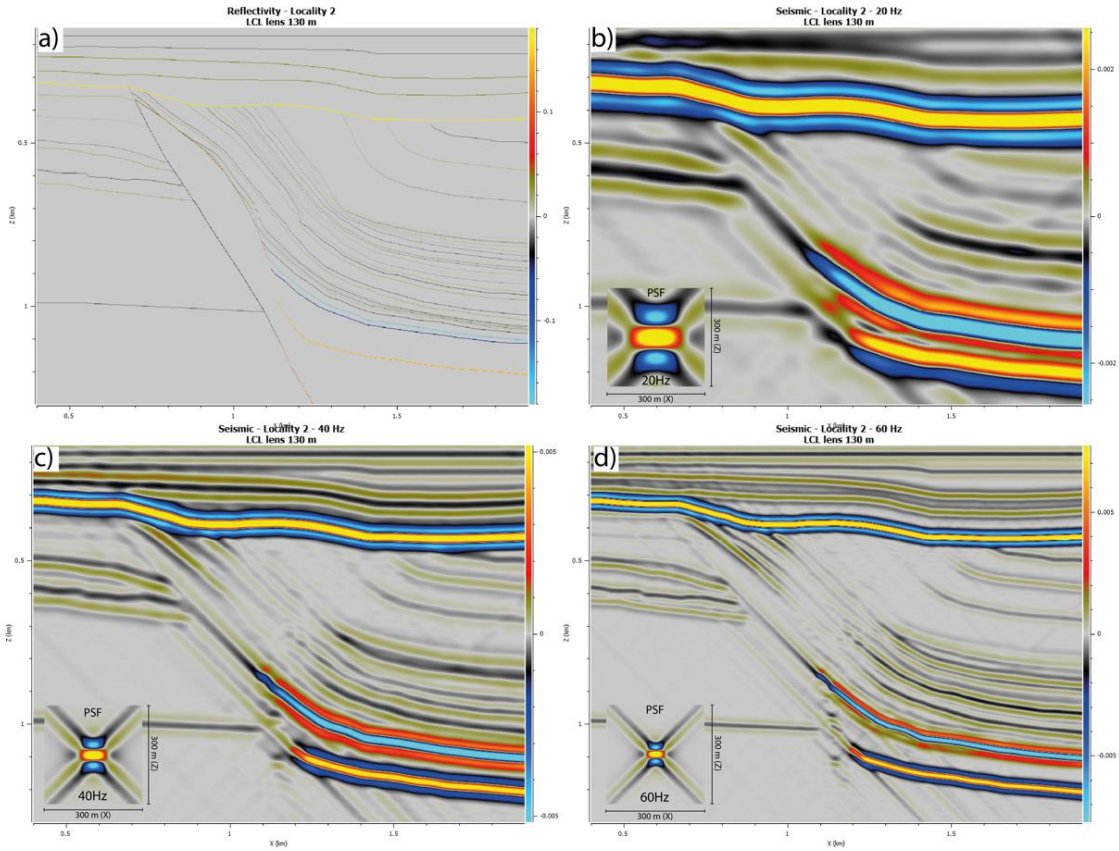

Fig. B 18: Seismic images of Locality 2 modelled with a 130 m thick LCL lens. a) Reflectivity model. b) 20 Hz seismic image. c) 40 Hz seismic image. d) 60 Hz seismic image.

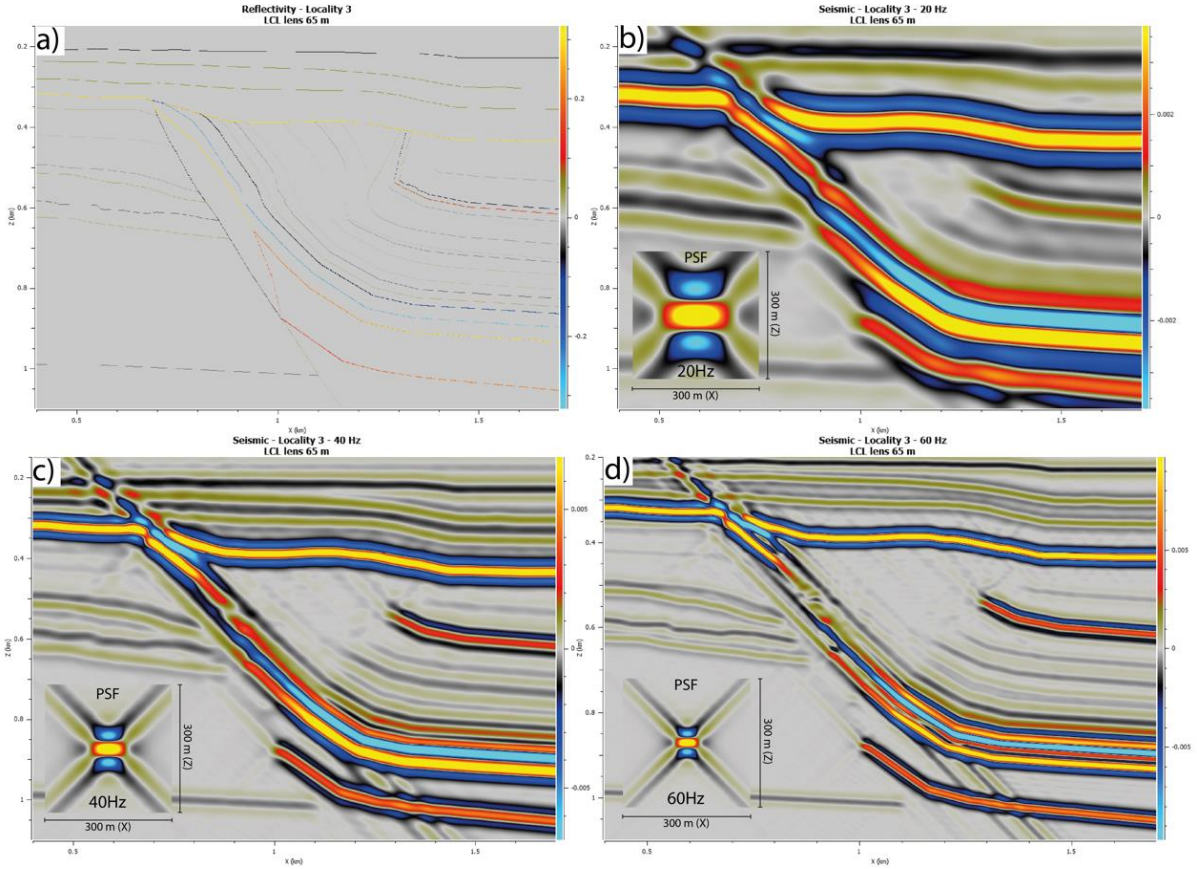

Fig. B 19: Seismic images of Locality 3 modelled with a 65 m thick LCL lens. a) Reflectivity model. b) 20 Hz seismic image. c) 40 Hz seismic image. d) 60 Hz seismic image.

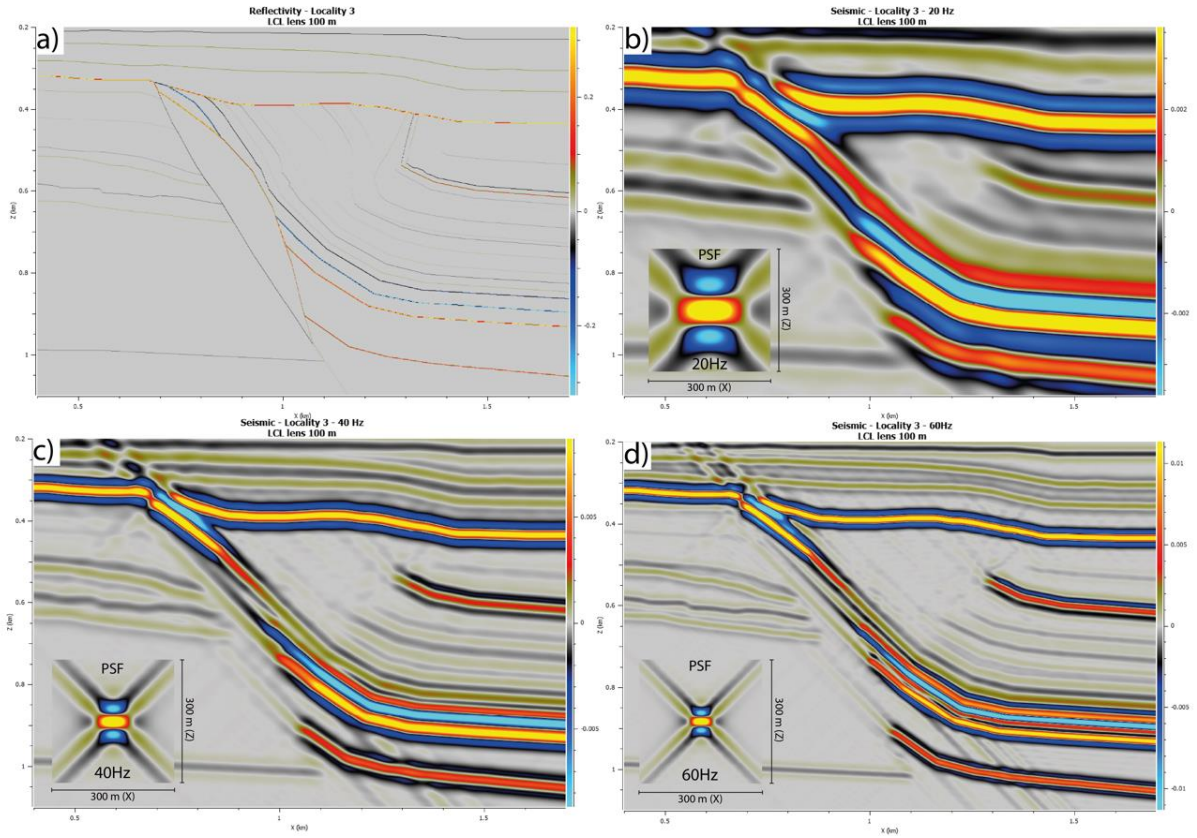

Fig. B 20: Seismic images of Locality 2 modelled with a 100 m thick LCL lens. a) Reflectivity model. b) 20 Hz seismic image. c) 40 Hz seismic image. d) 60 Hz seismic image.

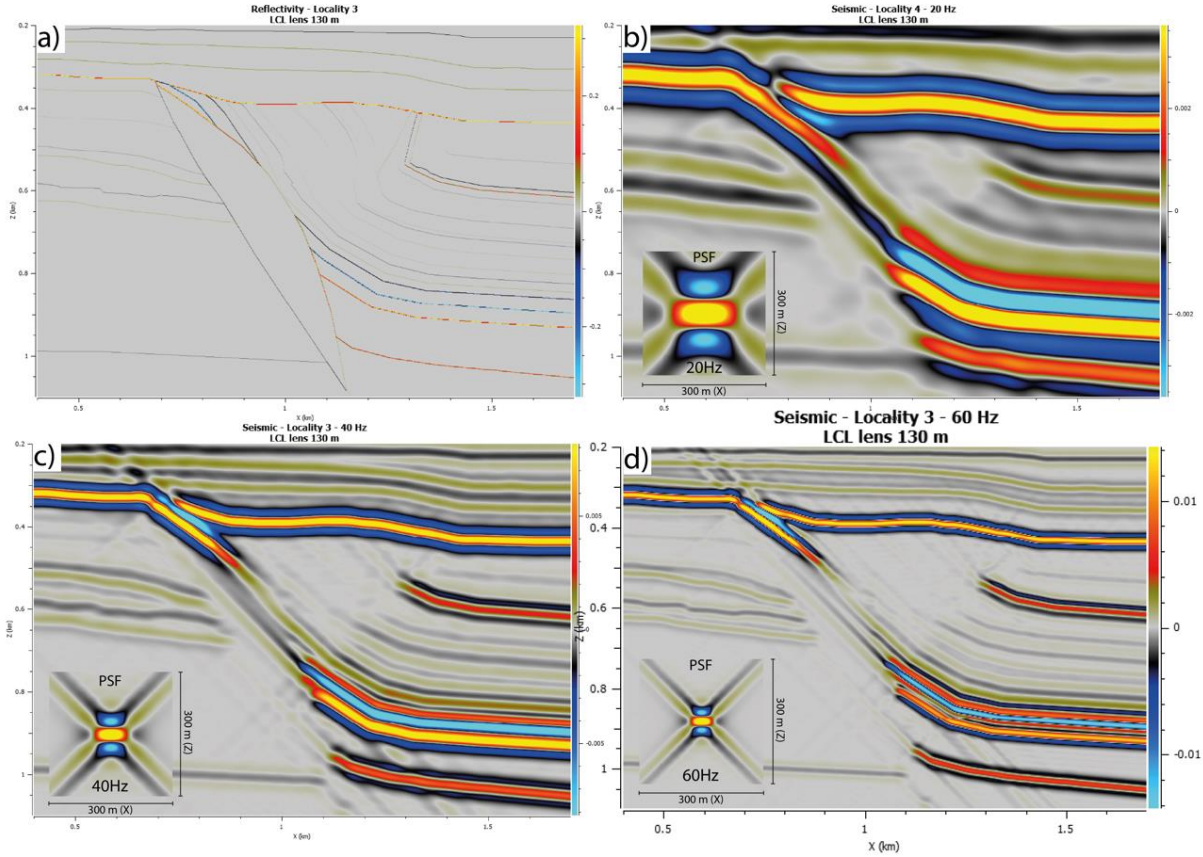

Fig. B 21: Seismic images of Locality 2 modelled with a 130 m thick LCL lens. a) Reflectivity model. b) 20 Hz seismic image. c) 40 Hz seismic image. d) 60 Hz seismic image.